Studies of the nuclear structure of ^{12}C and the astrophysical production of ^{23}Na

Nicolas James Hubbard

PhD

University of York
Physics

Aarhus University
Physics and Astronomy

March, 2018

Abstract (English)

Nuclear reactions can be used to study both the structure of the atomic nucleus, and to study the evolution of stars and the Universe. In this thesis two experiments are presented: one studying the astrophysical impact of the ^{23}Na$(\alpha,p)^{26}$Mg reaction, and one studying the nuclear structure of ^{12}C near the proton separation energy of 16 MeV.

The ^{23}Na$(\alpha,p)^{26}$Mg reaction is an important reaction affecting the abundances of ^{23}Na and the radioisotope ^{26}Al in massive stars. Before 2014 experimental and theoretical data on this reaction was of unknown uncertainty. A new direct measurement of the ^{23}Na$(\alpha,p)^{26}$Mg reaction was performed at Aarhus University and with two other independent modern measurements of the ^{23}Na$(\alpha,p)^{26}$Mg reaction a new combined experimental reaction rate has been calculated with an uncertainty of 30%, and the impact on ^{23}Na and ^{26}Al production has been modelled and the abundances constrained by this reaction.

^{12}C is a light, stable, and well-studied nucleus with current research generally on clustering phenomena. It is therefore unusual that a narrow shell-model predicted state with spin-parity 0^- has not been experimentally observed already. Excited states of ^{12}C were populated via the ^{11}B(^{3}He,d)^{12}C reaction at iThemba LABS in South Africa, and analysed through R-matrix theory. No 0^- state was observed in the region predicted by the shell-model, but a likely 0^- state has been identified above the proton separation energy, and a detailed analysis of its properties using R-matrix theory is presented.

Abstrakt (Dansk)

Kernereaktioner kan bruges til at studere både atomkernens struktur og at studere evolutionen af stjerner og universet. I denne afhandling præsenteres to eksperimenter: En undersøgelse af den astrofysiske virkning af ^{23}Na$(\alpha,p)^{26}$Mg -reaktionen og en undersøgelse af den nukleare struktur på ^{12}C nær protonseparationsenergien på 16 MeV.

^{23}Na$(\alpha,p)^{26}$Mg -reaktionen er en vigtig reaktion, der påvirker mængderne af ^{23}Na og radioisotopen ^{26}Al i massive stjerner. Før 2014 var eksperimentelle og teoretiske data om denne reaktion af ukendt usikkerhed. En ny direkte måling af ^{23}Na$(\alpha,p)^{26}$Mg reaktionen blev udført ved Aarhus Universitet og med to andre uafhængige moderne målinger af ^{23}Na$(\alpha,p)^{26}$Mg reaktionen er en ny kombineret eksperimentel reaktionshastighed beregnet med en usikkerhed på 30% og virkningen på ^{23}Na og ^{26}Al produktion er blevet modelleret, og de overflader, der er begrænset af denne reaktion.

^{12}C er en let, stabil og velundersøgt kerne med nuværende forskning generelt på clustering fænomener. Det er derfor usædvanligt, at en smal skalmodel forudsagt tilstand med spinparitet 0^- ikke er blevet eksperimentelt observeret allerede. Eksiterede tilstande i ^{12}C blev befolket via ^{11}B(^{3}He,d)^{12}C -reaktionen ved iThemba LABS i Sydafrika og analyseret med R-matrix teori. Ingen 0^- tilstand blev observeret i det område, der forudsiges af skalmodellen, men en sandsynlig 0^- tilstand er blevet identificeret over protonseparationsenergien og en detaljeret analyse af dens egenskaber ved hjælp af R-matrix teori præsenteres.

Contents

List of Tables

List of Figures

Acknowledgements

Firstly I would like to thank my supervisors, Drs Christian Diget and Hans Fynbo, for their support throughout the entire PhD. The advice and feedback that you have given has been invaluable, including the important lesson of when to leave something alone. I would like to thank you both for organising this joint programme between York and Aarhus, which has been challenging but incredibly rewarding. Credit must also be given for sorting out the administrative aspects of this joint programme, which I know was often complicated, but it all seems to have worked out.

I would like to thank those I have collaborated with throughout the PhD, particularly Dr Philip Adsley for the support and advice in analysing the data in iThemba, and handling the sometimes inane questions I ask when my mind blanks, even if the responses are dripping in sarcasm. Thanks to Dr Marco Pignatari for very helpful feedback on the astrophysics side of my work, and helping present the results in ways astronomers will find useful.

I must also thank all the people at iThemba LABS who helped during my experiments there, including: Retief and Ricky for their support in setting up and running the equipment, and for driving me to and from the lab as I couldn't drive. I would like to thank Luna, Vicente, Daniel and Lindsay for helping set up and run the experiments, including some very boring cabling and calibration, and of course everyone who took a shift during the runs. Similar thanks to those on the Aarhus experiment: Hans, Oliver, Michael, Kasper, Christian and particularly Alan Howard.

Thanks to all the staff and students at York and Aarhus for the fun times, good discussions (sometimes even about physics) and for Aarhus, helping me with moving to a new country. You've all been friendly and good fun to be around! Thanks also to the great people I have met at conferences and experiments, and for the good trips to pubs afterwards. I won't list everyone as it may grow too long, but I would like to especially thank my good friends: Abby, Osama, Ruchi and Laura, for offering support and particularly for putting up with me during the thesis write up.

Finally I must thank my family, particularly my parents and my sister, Emily, for being so supportive throughout life, offering welcome breaks from physics throughout my PhD, and for always making an effort to understand my work.

Declaration

I declare that this thesis is a presentation of original work and I am the sole author. This work has not previously been presented for an award at this, or any other, University. All sources are acknowledged as References.

The work in chapter 4 has been previously published as Howard et al. (2015) and contains work as part of a collaboration. The following aspects of the analysis have been explicitly performed by me: The target thickness analysis, initial yield calculations, extraction and comparison to other sources, initial astrophysical impact and single-resonance reaction rate, weighted cross-section energy, and final angular distributions as shown in this thesis. The following aspects of the analysis are included here for completeness but do not represent my original work: Target stoichiometry and Rutherford angle dependence was performed by M. Munch. Final yields, error analysis and published cross-sections were performed by A. Howard. Initial differential cross-sections were obtained by M. Munch (but re-evaluated and re-fitted by me). Figures obtained from Howard et al. (2015) are referenced as such.

The work in chapter 5 represents original work performed after the work in chapter 4 and after publication of Howard et al. (2015), as does the work in the subsequent chapters.

Part I

Introduction

Chapter 1

Introduction

The atomic nucleus is the small, dense, core of an atom. The nucleus is comprised of protons and neutrons, collectively nucleons, bound by the nuclear force. One way the nucleus can be studied is via nuclear reactions, in order to obtain information on the structure of nuclei and the nature of the nuclear force. Nuclear reactions are essential to astrophysics, in the field of nuclear astrophysics: nuclear reactions power all stars, and stars lead to the creation of elements throughout the Universe. This thesis presents two experiments utilising nuclear reactions, one measuring the astrophysically important $^{23}\mathrm{Na}(\alpha,p)^{26}\mathrm{Mg}$ reaction and evaluating its impact on stellar nucleosynthesis, and one determining the nature of excited states in $^{12}\mathrm{C}$, including the investigation of a theoretically predicted, but previously unobserved, excited state in the nucleus.

1.1 The $^{23}\mathrm{Na}(\alpha,p)^{26}\mathrm{Mg}$ Reaction

The field of nuclear astrophysics is the study of nuclear reactions within the context of astrophysical environments, particularly stars. Nuclear reactions provide two key aspects to stellar evolution: they provide the energy generation that fuels the life of a star, from the hydrogen fusion that powers the majority of stars like our Sun, up to the fusion of elements into iron – at which point nuclear fusion is no longer exothermic. Secondly, they enrich the Universe with heavy elements, which are nearly all produced within stellar environments. The chemical elements that make up Earth, and life itself, all originate from these stars.

A detailed description of how stars are responsible for the production of the chemical elements was first laid out in a landmark paper by Burbidge, Burbidge, Fowler, & Hoyle (1957), usually termed the $\mathrm{B}^2\mathrm{FH}$ paper. This paper explains features of the chemical abundance chart, figure 1.1, via a number of nuclear processes, such as the primary fusion of hydrogen into helium, helium into carbon, and α-particle nuclei such as oxygen-16, neon-20,

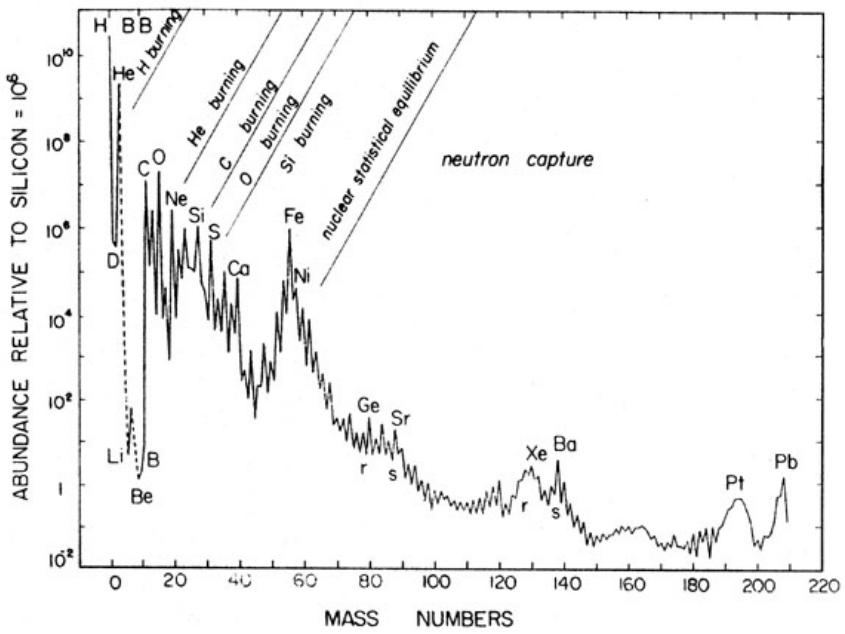

Figure 1.1: Abundance of the elements, normalised to 10^6 atoms of ^{28}Si. Figure from Pagel (1997). The features of this chart, such as the peaks of α-particle nuclei and the abundances of elements heavier than iron, were first explained by Burbidge, Burbidge, Fowler, & Hoyle (1957).

calcium-40 via the α-process. It also explains the production of heavier than iron elements, and radioactive elements by the rapid and slow neutron capture processes. This concept of stellar nucleosynthesis is now firmly established, and can be experimentally verified via the detection of short-lived radioactive isotopes such as ^{26}Al, with a half-life of 10^5 years, within the galaxy: such isotopes must be constantly produced to be observed today (Iliadis et al., 2011).

Although the concept of stellar nucleosynthesis is firmly established, the experimental and theoretical understanding is often difficult. There exist many thousands of isotopes and reactions that affect the abundances of chemical elements, and stellar reactions occur at comparatively low energies that are very difficult to achieve in the laboratory. Theoretical models can fill in the gaps in experimental knowledge, but their uncertainties on rates can lead to large potential variations in elemental abundances. Reduced uncertainty on reaction rates can constrain the chemical abundance of the elements, and combined with astronomical observations can be used to better constrain and understand astrophysical models of stellar interiors.

This thesis investigates one such reaction, the ^{23}Na$(\alpha, p)^{26}$Mg reaction,

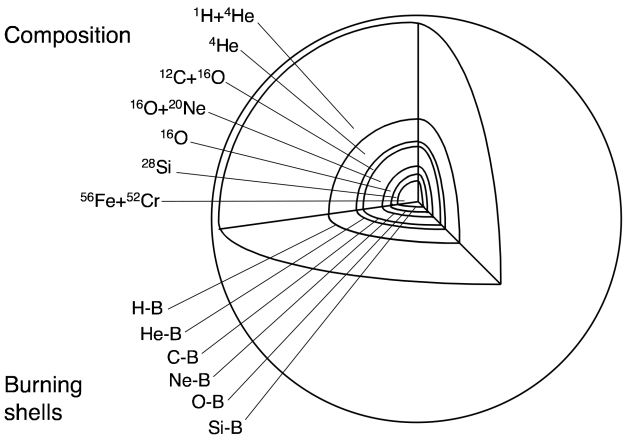

Figure 1.2: Schematic of the structure of a massive presupernova star, from Iliadis (2008). This highlights the typical onion-like structure of many shells fusing successively ligher elements as they approach the exterior. The upper labels describe the dominant isotopes and the lower labels the name of the burning shells.

which occurs inside massive stars, heavier than $11 M_{\odot}$[1]. Near the end of such a star's life a very complex interior forms, there is a central core undergoing fusion of silicon into iron and surrounding this core are many thin shells, which are fusing lighter elements that are still present. This leads to an onion-like structure of many shells fusing successively lighter elements as they approach the exterior of the star, figure 1.2. One such shell is the C/Ne shell, in which carbon is primarily being fused into Ne, Na or Mg via the reactions:

$$^{12}\mathrm{C} + {}^{12}\mathrm{C} \rightarrow {}^{20}\mathrm{Ne} + {}^{4}\mathrm{He} \quad (1.1)$$

$$^{12}\mathrm{C} + {}^{12}\mathrm{C} \rightarrow {}^{23}\mathrm{Na} + {}^{1}\mathrm{H} \quad (1.2)$$

$$^{12}\mathrm{C} + {}^{12}\mathrm{C} \rightarrow {}^{23}\mathrm{Mg} + {}^{1}n\ , \quad (1.3)$$

which occur at temperatures of approximately 1.4 GK (1.4×10^9 K). The ^{23}Na$(\alpha, p)^{26}$Mg reaction destroys the ^{23}Na produced by the above fusion, and provides additional protons (^{1}H) for reactions such as the ^{26}Al producing $^{25}\mathrm{Mg} + p \rightarrow {}^{26}\mathrm{Al} + \gamma$ reaction. The ^{23}Na$(\alpha, p)^{26}$Mg reaction's motivation and astrophysical impact is discussed in detail in chapter 3.

Until 2014 the ^{23}Na$(\alpha, p)^{26}$Mg reaction suffered from poor experimental data and a theoretical reaction rate with a large, unquantifiable, uncertainty. The reaction affects the chemical abundance of ^{23}Na and ^{26}Al and was highlighted as a reaction in need of new experimental data, to reduce the uncertainty to match other important reactions affecting ^{26}Al (Iliadis et al.,

[1] $M_{\odot}$ refers to the mass of the Sun: $1.98855(25) \times 10^{30}$ kg

2011). A new experimental measurement was performed at Aarhus University (chapter 4), and in combination with two other independent measurements performed at Argonne National Laboratory and TRIUMF by other research groups, a new combined experimental reaction rate has been calculated and the astrophysical impact has been evaluated (chapter 5).

1.2 Studies of ^{12}C Structure

Within science, there may be no element more impactful than carbon. The unique chemical properties of carbon, which has more compounds than any other element, lead to the field of organic chemistry – and to biology and other life sciences. Carbon compounds are the primary fuels that drive modern humanity, and carbon dioxide exerts a significant influence on our environment. Across physics there is extensive interest in graphene, a carbon allotrope exhibiting many beneficial properties, as well as atomic and nuclear studies of the element.

Within nuclear physics itself carbon remains significant, in nuclear astrophysics, where its status as the second element to be produced in stars after helium is important in driving the evolution of stars, and historically as the basis of arguments for stellar nucleosynthesis (Hoyle, 1954). The lack of stable isotopes with mass 5 or mass 8 requires carbon to be produced via the reaction of three α-particles, and this inherent difficulty leads to big bang nucleosynthesis producing predominantly hydrogen and helium, with stellar nucleosynthesis producing the heavier elements. The reaction occurs via the intermediate and very short-lived ^{8}Be nucleus (a half-life of 6.7×10^{-17} s):

$$^{4}\mathrm{He} + {}^{4}\mathrm{He} \rightarrow {}^{8}\mathrm{Be} \tag{1.4}$$

$$^{8}\mathrm{Be} + {}^{4}\mathrm{He} \rightarrow {}^{12}\mathrm{C}^{*} \, . \tag{1.5}$$

In order for this reaction to produce the abundance of carbon observed in the Universe, Hoyle argued there must be an excited state near the α-particle threshold in ^{12}C: the now famous Hoyle state.

In nuclear structure ^{12}C is well-known for its cluster phenomena: excited states such as the Hoyle state exhibit an unusual structure of three α-particles (Freer, 2007). Conversely, excited states that are well described as an excitation of a single particle within the ^{12}C nucleus are typically well studied and well predicted. This is due to their appearance in relatively simpler mean-field models such as the shell model, and due to their relative ease of population via transfer reactions, and their relatively clean decay modes aiding identification. A level diagram of ^{12}C is shown in figure 1.3.

The work in this thesis, however, is investigating the existence of a theoretically predicted single-particle-nature 0^{-} state near the proton separation threshold in ^{12}C. This state is reproduced in both shell model and effective field no-core shell model theory calculations, and its experimental absence is

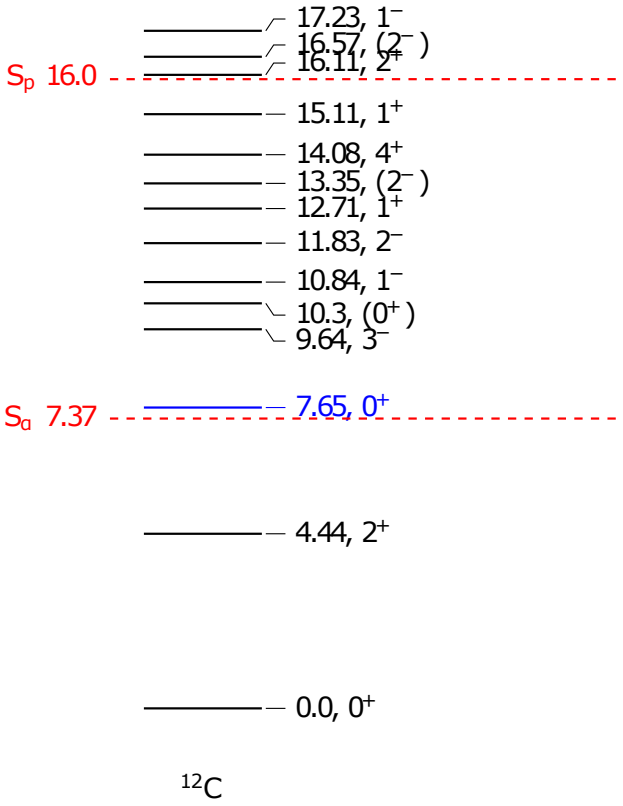

Figure 1.3: Level scheme of known states in ^{12}C, data from Kelley et al. (2017). The astrophysically important Hoyle state is noted in blue.

unexpected, particularly considering the strong population predicted by the shell model. If below the proton separation threshold the state would be limited to decaying via γ-ray decay, as α decay is prohibited due to parity conservation. Such a state would therefore be relatively long-lived, and therefore should be easily identified in experimental measurements as a narrow resonance. If above the proton separation threshold the decay mode would preferentially be via proton decay, becoming shorter lived and harder to detect as its excitation energy increases. The predictions of this state are discussed in detail in chapter 6.

To investigate this state, an experiment has been performed at iThemba LABS using the high-resolution K600 spectrometer (chapter 7) in order to probe the excited states in ^{12}C around the proton separation energy. Focus is particularly on the 15 MeV region where the shell model places the state, and the 18–20 MeV region where the no-core shell model places the state. Identification or non-identification of the state can provide useful constraints on the interactions modelled via the shell model or no-core shell model. The analysis of states below the proton separation energy and above the proton

separation energy are detailed in chapters 8 and 9, respectively. Above the proton separation energy the states are analysed using R-matrix theory in order to fit experimental data to state energy levels, spins, parities and decay widths. This analysis involves a new approach to R-matrix in order to account for the proton transfer mechanism utilised to populate the excited states.

Chapter 2

Theory

The atomic nucleus, the core of an atom, is a complex system comprised of protons and neutrons, collectively known as nucleons. They are bound together by the nuclear force, the residual of the strong force which binds the quarks inside individual nucleons. The nuclear force is unknown and complex, and as such the structure of nucleons within the nucleus is not known exactly. However, there exist many models which aim to describe the nucleus.

2.1 Nuclear Reactions

When two nuclei collide, there is a chance that they undergo a nuclear reaction, producing one or more new products. If we name the two incoming particles as A, a and two outgoing particles as B, b the reaction can be noted as $A+a \rightarrow B+b$, or more frequently $A(a,b)B$. Conventionally A is the target isotope and a the beam isotope, B is the heavier and b is the lighter produced nuclei. Nuclear reactions frequently involve a change in nuclear binding energy, which is known as the Q-value: a positive Q-value results in binding energy being liberated, increasing the kinetic energy of the product particles, conversely a negative Q-value results in a net decrease of the available kinetic energy, and requires a minimum kinetic energy for the reaction to occur. The Q-value of a reaction producing a nuclei in its excited state is equal to the Q-value of the reaction producing the nuclei in its ground state, minus the excitation energy of the excited state. Measurements of nuclear reactions are used to probe the structure of the nuclei, and to determine reaction rates determining the production and chemical evolution of elements within the galaxy. Both types of studies are used in this thesis, as well as atomic and nuclear studies of the element.

Cross sections

The probability that two colliding particles will react is represented by the cross-section σ, defined as:

$$\sigma = \frac{\text{Interactions per time}}{\text{Beam particles per time per area} \times \text{Target particles}} \tag{2.1}$$

This cross-section has units of area, although reaction cross-sections differ from simple geometrical cross-sections of a nucleus from the view of a beam upon a target by a large amount, and hence it is typically treated as a probability of interaction. The conventional unit of nuclear reaction cross-sections is the barn (b), equivalent to 1×10^{-28} m^2, along with SI prefixed variants such as the millibarn (mb), microbarn (μb) and nanobarn (nb). Assuming a perfect detector which entirely surrounds the reaction target, the cross-section can be obtained quantitatively from the reaction yield Y, the number of incident beam particles I, the target thickness t, molar mass A and Avogadro's number N_A:

$$\sigma = \frac{YA}{IN_At} \, . \tag{2.2}$$

A detector which does not fully surround the target will only measure the cross-section of a small solid angle $\Delta\Omega$: the differential cross-section $\frac{\mathrm{d}\sigma}{\mathrm{d}\Omega}$, which is the probability that reactants go into the solid angle $d\Omega$:

$$\frac{\mathrm{d}\sigma}{\mathrm{d}\Omega} = \frac{YA}{IN_At\Delta\Omega} \, . \tag{2.3}$$

The shape of this differential cross-section with respect to θ provides information about the nature of the reaction, such as the angular momentum transferred from the beam and target nuclei, and can provide indications of the nuclear structure of the produced nuclei.

Resonances

A resonance is the name given to states which are 'nearly bound', so named as they appear as strong peaks in cross-section data. A resonance is charactered by properties such as its energy (E_r), its spin-parity (J^π) its lifetime (τ) and the branching ratio for a particular channel i it decays by (B_i). The lifetime is related to the width of the resonance (Γ) by $\Gamma = \hbar/\tau$, where $\hbar$ is the reduced plank constant. Partial widths for a particular decay channel i can then be given by $\Gamma_i = B_i\Gamma$.

The partial width for a channel depends on many factors. The Coulomb and angular momentum potentials of the resonance result in classically forbidden regions through which the particle must tunnel, the probability of such tunnelling is given by the penetrability P_ℓ

$$P_\ell = \frac{1}{F_\ell(\eta, kR)^2 + G_\ell(\eta, kR)^2} \, , \tag{2.4}$$

where F_ℓ and G_ℓ refer to the regular and irregular Coulomb functions, respectively (Descouvemont & Baye, 2010). Where R is the interaction radius and k is the wavenumber in the centre of mass frame ($k = \sqrt{2\mu E/\hbar^2}$). The width also depends on the spectroscopic factor S: defined in terms of the overlap of the initial and final state wavefunctions (Iliadis, 2008). The spectroscopic factor relates to nuclear structure information and can be obtained from, or compared to, nuclear structure models such as the shell model. The width depends additionally on the single-particle reduced width θ_{sp}: the probability that the emitted particle appears at the boundary of the nucleus. Such a reduced width can be computed with an appropriate nuclear potential. The combination of these terms allows the computation of the partial width as follows:

$$\Gamma_i = \frac{2\hbar^2}{\mu R^2} P_\ell C^2 S_i \theta_{sp}^2 \,, \tag{2.5}$$

where R is the interaction radius used for calculating P_ℓ and θ_{sp}, μ is the reduced mass and C is the isospin Clebsch-Gordon coefficient.

The cross-section for a reaction proceeding through a single resonance in the compound nucleus via incoming channel i and outgoing channel f is given by the Breit-Wigner equation:

$$\sigma(E) = \frac{\lambda^2}{4\pi} \frac{2J+1}{(2j_a+1)(2j_b+1)} (1+\delta_{ab}) \frac{\Gamma_i \Gamma_f}{(E-E_r)^2 + \Gamma^2/4} \,, \tag{2.6}$$

where λ is the de Broglie wavelength, the $(2j+1)$ factors account for averaging spin projections over the incoming channel, and summing projections over the outgoing channel. The $(1+\delta_{ab})$ term takes into account cases where the reaction is between identical particles (a, b being the reactant particles, and δ_{ab} being 1 only if $a = b$).

A resonance can also be described by its resonance strength, proportional to the maximum cross-section and total width of the resonance. Resonance strengths are useful for obtaining astrophysical reaction rates for reactions proceeding via isolated resonances, and is defined as:

$$\omega\gamma = \frac{2J+1}{(2j_a+1)(2j_b+1)} \frac{\Gamma_i \Gamma_j}{\Gamma} \,. \tag{2.7}$$

DWBA

At high energies compared to the energy of the populated resonances in B and b, the reactions occurring are likely to be direct reactions involving few nucleon-nucleon interactions due to the shorter de Broglie wavelengths. Such reactions cause the ejectile to retain information from before the interaction, and the angular distribution is strongly peaked at small scattering angles. A common type of direct reaction is the transfer reaction, involving one or more nucleons which are transferred from the projectile to the target nucleus.

Transfer reaction angular distributions are very sensitive to the ℓ-value transferred, allowing the J^π of states to be determined. In order to do so however, the distributions must be compared to some calculated distribution. In this case, the Distorted-Wave Born Approximation (DWBA) is used.

The Born Approximation is used when the interaction strength is small compared to the interaction energy of the bound system, it can be treated as a perturbation. In this instance, it is possible to consider an interaction limited to a finite number of steps, rather than a complete interaction theory. The Born Approximation usually refers to the first-order Born Approximation, where the number of steps is limited to one.

When dealing with transfer reactions of charged particles, the incoming and outgoing waves are expressed in terms of the Coulomb functions: the distorted waves of DWBA. The Born approximation involves splitting the potential into two parts, the larger of which is the exactly known Coulomb potential, the wave-functions can then be calculated by expanding the smaller unknown nuclear potential (Taylor, 1983). Comparing the differential cross-sections of experimental measurements and DWBA allow the ℓ-value to be assigned, and the J^π to be determined, or constrained, depending on the involved spins of the reaction. In this thesis, proton transfer reactions are considered, which have a spin $\frac{1}{2}$. Assuming the initial spin state of the target is J_i the possible J states populated are given by:

$$\left| J_i - \frac{1}{2} - \ell \right| \leq J \leq J_i + \frac{1}{2} + \ell \,, \tag{2.8}$$

and the parity is given by $\pi = \pi_i \times (-1)^\ell$: even values of ℓ do not change the parity, and odd values invert it. Although the DWBA cross-section can be calculated for all angles, the assumptions of the Born approximation limit the reliability to the first minimum (Naqib & Green, 1968), and are typically best satisfied around the first maximum (Schiffer et al., 2013) corresponding to where the projectile grazes the surface of the nucleus. The DWBA cross-section, which solely deals with the kinematic nature of the reaction, and the experimental cross-sections can be related by the spectroscopic factor S as (Krane, 1987):

$$\left(\frac{\mathrm{d}\sigma}{\mathrm{d}\Omega}\right)_{exp} = C^2 S \left(\frac{\mathrm{d}\sigma}{\mathrm{d}\Omega}\right)_{DWBA} . \tag{2.9}$$

R-matrix

At low energies, the reaction cross-sections are dominated by resonances in the compound nucleus formed by the two reactants. In these cases the cross-sections can calculated from resonance properties using R-matrix theory (Lane & Thomas, 1958; Descouvemont & Baye, 2010), or equivalently resonance properties can be calculated from experimentally measured cross-sections. Central to the R-matrix framework is the division of the reaction into an

"internal" region corresponding to the compound nucleus, and an "external" region corresponding to the reaction channels which enter or exit the compound nucleus. The external region has no interaction from the nuclear force, and can be calculated exactly. The internal region provides the resonance parameters. The two regions are defined by the R-matrix radius a, an essential but unphysical parameter in R-matrix theory.

Accounting for each partial wave separately, we can define the collision function U, a property proportional to the total cross-section:

$$\sigma = \frac{\pi}{k^2} \sum_{\ell} (2\ell + 1) \left| 1 - U_\ell \right|^2 \ , \tag{2.10}$$

whereas internally we can discuss the resonant states $X_{\lambda\ell}(r)$ for each partial wave, resulting from the Schrödinger equation:

$$-\frac{\hbar^2}{2m} \frac{\mathrm{d}^2 X_{\lambda\ell}}{\mathrm{d}r^2} + V(r) X_{\lambda\ell} = E_{\lambda\ell} X_{\lambda\ell} \tag{2.11}$$

and imposed boundary condition:

$$a_\ell \left(\frac{\mathrm{d}X_{\lambda\ell}}{\mathrm{d}r} \right)_{r=a} = b_\ell \ , X_{\lambda\ell}(a\ell) \tag{2.12}$$

where b_ℓ is the boundary condition number and a_ℓ is the R-matrix radius. The total internal wave function $\phi_\ell(r) = \sum_\lambda c_\lambda X_{\lambda\ell}$ must satisfy the same Schrödinger equation and can be matched at the radius using Green's theory (Vogt, 2005):

$$\left(\frac{\phi'_\ell}{\phi_\ell} \right)_{r=a_\ell} = \frac{1 + b_\ell R_\ell}{R_\ell} \ , \tag{2.13}$$

where the prime symbol indicates the dimensionless derivative $rd\phi/dr$ and the R-function is defined as:

$$R_\ell = \sum_{\ell\lambda} \frac{\gamma^2_{\ell\lambda}}{E_{\ell\lambda} - E} \ , \tag{2.14}$$

with γ being the reduced width amplitude, proportional to the wavefunction of the resonant state X at the R-matrix radius:

$$\gamma^2_{\lambda\ell} = \frac{\hbar^2}{2ma_\ell} X^2_{\lambda\ell}(a_\ell) \ . \tag{2.15}$$

By matching the internal and external logarithmic derivatives at the R-matrix radius, we can obtain the collision function:

$$U_\ell = O_\ell^{-1} (1 - R_\ell L_\ell)^{-1} (1 - R_\ell L^*_\ell) I_\ell \ , \tag{2.16}$$

where I_ℓ refers to the incoming wave function, O_ℓ the outgoing wave function, and $L_\ell \equiv O'_\ell / O_\ell - b_\ell$. By solving the external radial Schrödinger equation in

the presence of a Coulomb and angular momentum barrier we obtain definitions for the wave functions in term of Coulomb waves F_ℓ and G_ℓ

$$I_\ell = (G_\ell - iF_\ell)\exp(i\omega_\ell) \tag{2.17}$$

and

$$O_\ell = (G_\ell + iF_\ell)\exp(-i\omega_\ell)\ , \tag{2.18}$$

where $\omega_\ell = \sum_n^\ell \tan(Z_1 Z_2 e^2/h\upsilon n)$. By redefining L_ℓ in terms of the standard penetration factor P_ℓ and shift function S_ℓ:

$$L_\ell = S_\ell - b_\ell + iP_\ell\ , \tag{2.19}$$

we can obtain standard definitions:

$$P_\ell = \frac{kr}{F_\ell^2+G_\ell^2} \tag{2.20}$$

$$S_\ell = \frac{F'_\ell F_\ell + G'_\ell G_\ell}{F_\ell^2+G_\ell^2} \tag{2.21}$$

$$O_\ell^{-1} I_\ell = \exp(2i\Omega_\ell) \tag{2.22}$$

$$\Omega_\ell = \omega_\ell - \tan(F_\ell/G_\ell)\ . \tag{2.23}$$

With these definitions the cross-section of a single resonance can be obtained by defining the R-function (Vogt, 2005) as containing a single resonance λ, and inserting this one-term R-function and the external functions into the collision function, and in turn, the collision function into the cross-section formula:

$$\sigma = \frac{\pi}{k^2}(2\ell+1)\left|-\exp(2i\Omega_\ell)\frac{1+i\Gamma_{\lambda\ell}}{[(E_{\lambda\ell}-E+\Delta_{\lambda\ell})-(i/2)\Gamma_{\lambda\ell}]}\right|^2\ , \tag{2.24}$$

where:

$$\Gamma_{\lambda\ell} = 2P_\ell\gamma_{\ell\lambda}^2 \tag{2.25}$$

and

$$\Delta_{\lambda\ell} = (S_\ell - b_\ell)\gamma_{\ell\lambda}^2\ . \tag{2.26}$$

This cross-section can be compared to the Breit-Wigner formula (equation 2.6), but incorporates additional effects between potential and resonance scattering (Vogt, 2005), although it excludes complications of multiple resonances, channels and the coupling of spins. The energy shift Δ is dependent on the boundary condition chosen, the customary condition being the "natural" condition: $b_\ell = S_\ell$.

Practical applications of the above formulae are complicated by the energy dependence of the P_ℓ and S_ℓ functions. The P_ℓ function is very strongly energy dependent, whereas the S_ℓ function is weakly energy dependent. The usual approximation is one by Thomas (1951), which is to expand the shift linearly

with energy. We can then define the energy at which the cross-section is maximum, the resonance energy E_R as:

$$E_R - E_\lambda - \Delta_\lambda(E_R) = 0 \,, \tag{2.27}$$

and by utilising the Thomas approximation

$$E_\lambda + \Delta_\lambda = (E_R - E)\left[1 - \left(\frac{\mathrm{d}\Delta_\lambda}{\mathrm{d}E}\right)_{E_R}\right] \,, \tag{2.28}$$

applying this into the cross-section formula (equation 2.24) we can replace the above 'formal' parameters $E_\lambda, \Gamma_\lambda$ with 'observed' parameters E_R, Γ_R (with $\Delta = 0$), where

$$\Gamma_R = \frac{\Gamma_\lambda}{1 - (\mathrm{d}\Delta_\lambda/\mathrm{d}E)_{E_R}} \,. \tag{2.29}$$

An alternative formalism, by Brune (2002) can be used in which the R-matrix explicitly takes these observed parameters as inputs.

The extension to multiple channels largely involves replacing the R-function described in equation 2.14 with the R-matrix. For ingoing channel c and outgoing channel c' the R-matrix is defined as

$$R_{cc'}(E) = \sum_\lambda \frac{\gamma_{\lambda c}\gamma_{\lambda c'}}{E_\lambda - E} \,. \tag{2.30}$$

The problem can also be rewritten to represent a matrix in terms of levels rather than channels, permitting a problem more computationally feasible for a large number of channels providing the level number remains small. This form is named the A-matrix and is defined as (Lane & Thomas, 1958):

$$(A^{-1})_{\lambda\lambda'} = (E_\lambda - E)\delta_{\lambda\lambda'} + \Delta_{\lambda\lambda'} - (i/2)\Gamma_{\lambda\lambda'} \,, \tag{2.31}$$

where

$$\Delta_{\lambda\lambda'} = \sum_c \gamma_{\lambda c}\gamma_{\lambda' c}(S_c - b_c) \tag{2.32}$$

and

$$\Gamma_{\lambda\lambda'} = \sum_c \gamma_{\lambda c}\gamma_{\lambda' c} 2P_c \,, \tag{2.33}$$

the collision matrix U is redefined as (Vogt, 2005):

$$U_{cc'} = \exp\left(i(\Omega_c + \Omega_{c'})\right)\left[\delta_{cc'} + i\sum_{\lambda\lambda'} \Gamma^{1/2}_{\lambda c}\Gamma^{1/2}_{\lambda' c'} A_{\lambda\lambda'}\right] \,. \tag{2.34}$$

Hauser-Feshbach

Hauser-Feshbach theory discusses the extreme situation where at higher excitation energies, the resonances become broader and more closely packed. There is a transition from isolated resonances to the continuum, where the resonances overlap to the point no structure remains on the cross-section – it varies smoothly with energy. The reaction cross section can then be derived by averaging over any structure. The total cross-section is the sum of partial cross-section contributions from separate J, π:

$$\langle \sigma(\alpha, \alpha') \rangle = \sum_{J\pi} \langle \sigma(\alpha, \alpha') \rangle^{J\pi} \ . \tag{2.35}$$

For a specific $J\pi$ and for a pair of particles (α, α'), we can factor the cross-section into formation of a compound nucleus C via channel α, and branching ratio for decay into channel α':

$$\langle \sigma(\alpha, \alpha') \rangle^{J\pi} = \sigma_{\alpha C}^{J\pi} \Gamma_{\alpha'}^{J\pi} \ , \tag{2.36}$$

where the width can be obtained via the reciprocity theorem (Iliadis, 2008) and summing over all channels α'':

$$\Gamma_{\alpha'}^{J\pi} = \frac{(2J_1' + 1)(2J_2' + 1) k_{\alpha'}^2 \sigma_{\alpha' C}^{J\pi}}{\sum_{\alpha''} (2J_1'' + 1)(2J_2'' + 1) k_{\alpha''}^2 \sigma_{\alpha'' C}^{J\pi}} \ . \tag{2.37}$$

The formation of the compound nucleus cross-section is given by:

$$\sigma_{\alpha C} = \sum_{J\pi} \sigma_{\alpha C}^{J\pi} = \frac{\pi}{k^2} \sum_{\ell} (2\ell + 1) T_\ell(\alpha) \ . \tag{2.38}$$

As the cross section is averaged over many resonances, we can assume T does not depend on J and can thus rewrite equation 2.38 with explicit spin factors:

$$\sigma_{\alpha C} = \frac{\pi}{k^2} \sum_{J\pi} \frac{2J + 1}{(2J_1 + 1)(2J_2 + 1)} \sum_{s=|J_1 - J_2|}^{J_1 + J_2} \sum_{\ell=|J-s|}^{J+s} T_\ell(\alpha) \ . \tag{2.39}$$

Comparing the two equations 2.38 and 2.39 gives a formula for the partial cross-section:

$$\sigma_{\alpha C}^{J\pi} = \frac{\pi}{k^2} \frac{2J + 1}{(2J_1 + 1)(2J_2 + 1)} \sum_{s\ell} T_\ell(\alpha) \ . \tag{2.40}$$

Finally, combining the equations 2.35, 2.36, 2.37, and 2.40 we can derive a total Hauser-Feshbach energy averaged cross-section:

$$\langle \sigma(\alpha, \alpha') \rangle = \frac{\pi}{k_\alpha^2} \sum_{J,\pi} \frac{2J + 1}{(2J_1 + 1)(2J_2 + 1)} \frac{\left[\sum_{sl} T_l(\alpha)\right] \left[\sum_{s'l'} T_{l'}(\alpha')\right]}{\sum_{\alpha''} \sum_{s''l''} T_{l''}(\alpha'')} \ . \tag{2.41}$$

The transmission coefficient T is given by:

$$T_\ell(\alpha) = 1 - \left| e^{2i\delta_{\alpha\ell}} \right|^2 , \tag{2.42}$$

where $\delta_{\alpha\ell}$ is the elastic scattering phase shift, and can be obtained from an elastic scattering (real) potential V_0 by solving the Schrödinger equation, where at large distances $V(r) = 0$, the radial equation

$$u_\ell = sin(kr - \ell\pi/2 + \delta_\ell), \quad r \to \infty \tag{2.43}$$

differs at most from the free-particle expression by the phase shift (Iliadis, 2008). Phase shifts can also be related to the elastic scattering differential cross-section by

$$\left(\frac{\mathrm{d}\sigma}{\mathrm{d}\Omega}\right)_{el} = \frac{1}{k^2} \left| \sum_{\ell=0}^{\infty} (2\ell + 1) \sin\delta_\ell P_\ell(\cos\theta) \right|^2 , \tag{2.44}$$

allowing experimental determination of phase shifts.

2.2 Nuclear Astrophysics

Reaction Rates

In a stellar environment the centre-of-mass energy of the reactants is not fixed as it is in an experiment, but instead is in a thermal equilibrium and thus has an energy distributed according to the Maxwell-Boltzmann distribution. In these environments it is better to refer to the *reaction rate* as a function of temperature, rather than the cross-section as a function of energy. The reaction rate R is described in terms of number of reactions per volume per time, and can be related to the cross-section by:

$$R = \frac{N_r}{Vt} = \sigma(v) v \frac{N_a}{V} \frac{N_b}{V} = \sigma(v) v n_a n_b , \tag{2.45}$$

where $\sigma(v)$ is the velocity dependent cross-section, v is the relative velocity between the two species a and b, N is the number of ions within an arbitrary volume V, equivalently given by the number density n. This equation assumes that the velocity between the two particles is constant, whereas for a constant temperature the velocity will cover a range of values according to the Maxwell-Boltzmann distribution $P(v)$, in this case we rewrite R as

$$R = n_a n_b \langle \sigma v \rangle = n_a n_b \int P(v) v \sigma(v) \, \mathrm{d}v , \tag{2.46}$$

where the Maxwell-Boltzmann distribution is:

$$P(v)\mathrm{d}v = 4\pi v^2 \left(\frac{\mu}{2\pi kT}\right)^{\frac{3}{2}} \exp\left(-\frac{\mu v^2}{2kT}\right) \mathrm{d}v \tag{2.47}$$

or, in units of energy via the relation $E = \frac{1}{2}\mu v^2$

$$P(E)\mathrm{d}E = \frac{2}{\sqrt{\pi}}\frac{1}{(kT)^{\frac{3}{2}}}\sqrt{E}\exp\left(-\frac{E}{kT}\right)\mathrm{d}E\ . \tag{2.48}$$

In astrophysics, reaction rates are usually tabulated normalised to a mole of reacting particles: $n_a n_b = N_A \approx 6.02 \times 10^{23}$, and combining equations 2.46 and 2.48 we obtain a definition of reaction rate in terms of energy-dependent cross-section:

$$N_A\langle\sigma v\rangle = N_A\left(\frac{8}{\pi\mu}\right)^{\frac{1}{2}}\left(\frac{1}{kT}\right)^{\frac{3}{2}}\int_0^\infty \sigma(E)E\exp\left(\frac{-E}{kT}\right)\mathrm{d}E\ . \tag{2.49}$$

Because the cross-section data has a strong energy dependence due to the Coulomb repulsion term, it is often simpler to factor out this term, particularly before performing interpolation or extrapolation of experimental data for astrophysical evaluations. We can define the cross-section as the Coulomb repulsion term multiplied by the astrophysical S-factor:

$$S(E) \equiv \frac{E}{\exp\left(-2\pi\eta\right)}\sigma(E)\ , \tag{2.50}$$

where η is the Sommerfeld parameter:

$$\eta = \frac{Z_1 Z_2 e^2}{4\pi\epsilon_0\hbar\nu}\ . \tag{2.51}$$

We can also rewrite the formula for the astrophysical reaction rate from equation 2.49 in terms of the S-factor rather than cross-section:

$$\langle\sigma v\rangle = \left(\frac{8}{\pi\mu}\right)^{\frac{1}{2}}\left(\frac{1}{kT}\right)^{\frac{3}{2}}\int_0^\infty S(E)\exp\left(-\frac{E}{k_B T} - \sqrt{\frac{E_G}{E}}\right)\mathrm{d}E\ , \tag{2.52}$$

where:

$$E_G \equiv 4\pi^2\eta^2 E\ . \tag{2.53}$$

Because the cross-section increases with E and the Maxwell-Boltzmann distribution decreases with E, there is a region of energy where E is large enough for the cross-section to be large, and small enough for the probability of the reactants having the required E to be large, as shown in figure 2.1. This region is known as the Gamow window, and is the energy region where, for a given temperature, reactions are most likely to occur. This window, although asymmetric, is frequently approximated as a Gaussian, the location (E_0) and width (ΔE) for the Gamow window for charged particle reactions, in MeV, are given as (Rolfs & Rodney, 2005):

$$E_0 = 0.122(Z_1^2 Z_2^2\mu)^{1/3}\ T_9^{2/3}\ \mathrm{MeV} \tag{2.54}$$

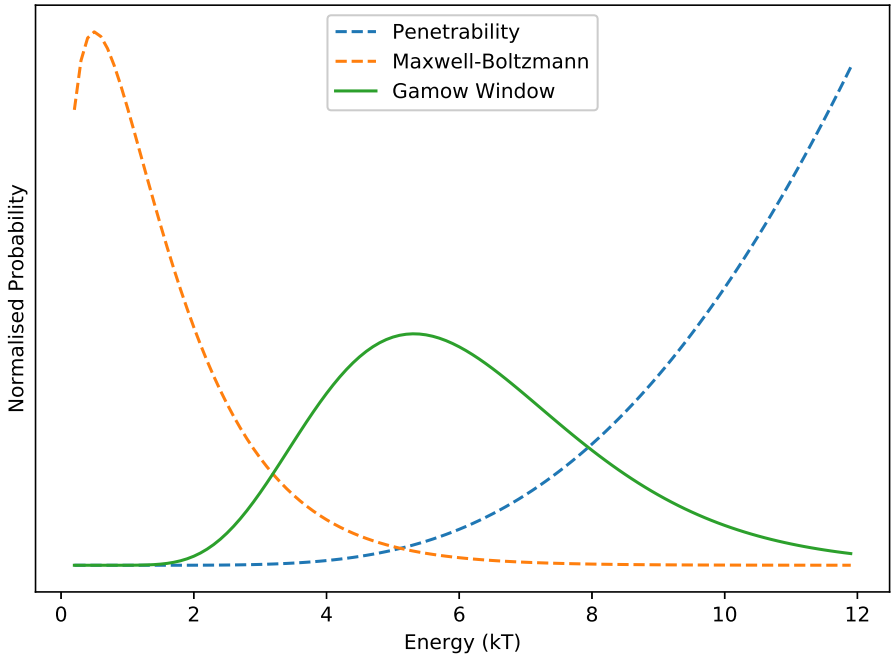

Figure 2.1: Illustration of the Gamow window. The Maxwell-Boltzmann distribution probability decreases rapidly with increasing energy, whereas the cross-section increases rapidly. The convolution of the two forms a region of maximum probability known as the Gamow window.

$$\Delta E = 0.2368(Z_1^2 Z_2^2 \mu)^{1/6} T_9^{5/6} \text{ MeV} , \tag{2.55}$$

where $Z_{1,2}$ are the charges of the reactants, $\mu = \frac{A_1 A_2}{A_1 + A_2}$ and T_9 is the temperature in GK. Because the reaction probability is greatest in this window, experimental and theoretical studies aim to obtain cross-sections within this region. This can be challenging for reactions occurring in cooler regions of stars, where the Gamow window can be lower in energy than can be reasonably measured in laboratories.

The physics affecting nuclear reactions is time reversible and as such measurements of cross-sections and reaction rates for the reaction $i(j,o)m$ can also be used to obtain measurements for the reverse reaction $m(o,j)i$ (Iliadis, 2008). The cross-sections are related by phase space:

$$\frac{\sigma_{rev}}{\sigma} = \frac{(2J_i + 1)(2J_j + 1)}{(2J_o + 1)(2J_m + 1)} \frac{A_{ij} E_{ij}}{A_{om} E_{om}} . \tag{2.56}$$

In astrophysical systems we also need to account for the excitation into non-ground states, assuming a thermal equilibrium of the states (as in a stellar

plasma), and we need to take into account transitions between these excited states. To account for these, we incorporate *partition functions* G_i:

$$G_i = \frac{\sum_\mu g_{i\mu} \exp\left(-E_{i\mu}/kT\right)}{g_{i0}} \,, \tag{2.57}$$

where $g_{i\mu}$ and $E_{i\mu}$ are the statistical weight and excitation energy of the excited state μ and g_{i0} is the statistical weight of the ground state. Numerical values of these partition functions are tabulated in Rauscher & Thielemann (2000). By assuming the partition functions for the light nuclei j, o are 1 (no excited states), averaging over the initial states and summing over final states, we find for the reverse reaction (Rauscher & Thielemann, 2000):

$$N_A\langle\sigma_m v\rangle = \left(\frac{A_i A_j}{A_o A_m}\right)^{3/2} \frac{(2J_i+1)(2J_j+1)}{(2J_o+1)(2J_m+1)} \frac{G_i(T)}{G_m(T)} e^{-Q/kT} N_A\langle\sigma_i v\rangle \,. \tag{2.58}$$

Post Processing

In massive stars the number of reactions occurring simultaneously is in the thousands, and as such it is computationally infeasible to model every reaction when modelling stellar evolution, instead only the primary energy producing reactions are included. For studying the isotopic evolution of a star, and the final abundances that may be emitted into the wider galaxy, a post-processing calculation is performed. In these calculations the stellar evolution is taken as input from a previously ran model, which fully describes how the stellar environment changes with time. The post-processing calculations then perform large reaction rate networks over time, based on these stellar environments. Because only the abundances need to be tracked, rather than any hydrodynamical processes, this post-processing can be performed much quicker than a full hydrodynamical simulation. In addition, because separate regions of the star do not influence each other during the calculations, they can be run independently resulting in a large speed-up with parallel processing technologies. Pre-determined mixing coefficients can be incorporated after the abundance calculations, to account for convective stellar regions.

Part II

The ^{23}Na$(\alpha, p)^{26}$Mg Reaction

Chapter 3

Measurement of the ^{23}Na$(\alpha, p)^{26}$Mg Reaction Rate

3.1 Astrophysical Motivation

The ^{23}Na$(\alpha, p)^{26}$Mg reaction has been identified as having a significant impact on the nucleosynthesis of ^{23}Na in massive stars, which is the major source of ^{23}Na abundance within the Universe (Timmes et al., 1995). This is verified by observations of the sodium-to-iron ratio, shown in figure 3.1, observations which largely agree with models assuming massive stars are the sole source of ^{23}Na, although small amounts of additional sodium may be necessary to explain the ratio in high metallicity stars (Timmes et al., 1995). As such, understanding of the production and destruction of ^{23}Na in massive stars is important for galactic chemical evolution studies. ^{23}Na is primarily produced in the carbon burning stages of massive stars, via the carbon burning reaction ^{12}C$(^{12}$C$, p)^{23}$Na, with about 10% of ^{23}Na being produced in the hydrogen envelope as part of the Ne-Na cycle (Woosley & Weaver, 1995). The ^{23}Na$(\alpha, p)^{26}$Mg reaction occurs in the carbon burning stage of a massive star, and would destroy the produced ^{23}Na. A study of type-1a supernovae by Bravo & Martínez-Pinedo (2012) found the ^{23}Na$(\alpha, p)^{26}$Mg reaction to affect the production of ^{21}Ne, ^{23}Na, ^{26}Mg, ^{29}Si, ^{43}Ca and ^{47}Ti, with their abundances changing by a factor of $0.12 - 2$ when the ^{23}Na$(\alpha, p)^{26}$Mg reaction is increased or decreased by a factor of 10, and with ^{26}Mg and ^{43}Ca changing by over a factor of 2.

The ^{23}Na$(\alpha, p)^{26}$Mg reaction has also been identified as affecting the production of the radioisotope ^{26}Al, an important observational γ-ray emitter which can help understand the processes occurring in the cores of massive stars. ^{26}Al has been measured by the γ-ray telescopes COMPTEL (Chen et al., 1995) and INTEGRAL (Diehl et al., 2013). The distribution of ^{26}Al within the galaxy is irregular, see figure 3.2, implying massive stars are the primary source of ^{26}Al, although the exact site is not known (Iliadis et al.,

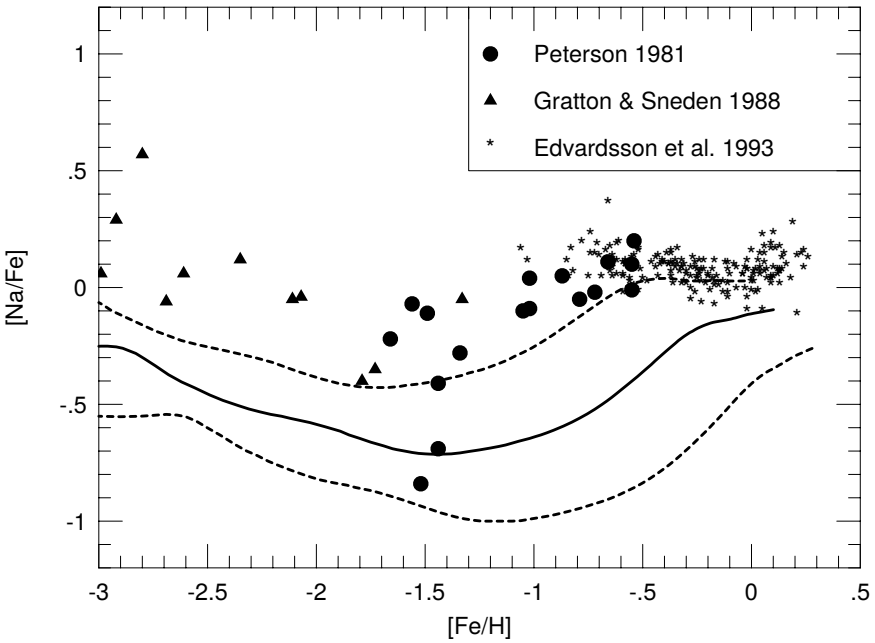

Figure 3.1: Evolution of the sodium-to-iron ratio [Na/Fe] as a variation of the metallicity [Fe/H] by Timmes et al. (1995). The solid and dashed lines represent evolution predicted from massive stars as the source of sodium.

2011). ^{26}Al (5^+) decays by β decay to the first excited state in ^{26}Mg (2^+) which subsequently decays to the ^{26}Mg ground state by emission of a 1.8 MeV γ-ray, shown in figure 3.3 – it is this γ-ray which is detected by telescopes. This decay occurs with a half-life of 7×10^5 years, short in stellar terms, and as such provides a snapshot of current conditions within the star (Iliadis et al., 2011). These understandings are limited by how well the nuclear processes affecting production and destruction of ^{26}Al are understood.

Motivated by the importance of ^{26}Al, a study on the sensitivity of ^{26}Al abundance to various reaction rates was performed by Iliadis et al. (2011), a table of the 5 most significant reactions is shown in table 3.1. The $^{23}\mathrm{Na}(\alpha, p)^{26}\mathrm{Mg}$ reaction was identified as having a significant impact on the production of ^{26}Al: producing protons for the $^{25}\mathrm{Mg}(p, \gamma)^{26}\mathrm{Al}$ reaction within hydrogen-deficient massive stars. An increase in the $^{23}\mathrm{Na}(\alpha, p)^{26}\mathrm{Mg}$ reaction rate by a factor of 10 was determined to increase the ^{26}Al production by a factor of 3 (Iliadis et al., 2011). Weaknesses in the early experimental measurements had been identified, leading to the use of the statistical Hauser-Feshbach model in astrophysical models such as REACLIB (Cybert et al., 2010). These models themselves are predicted to have an uncertainty greater than a factor of 2 for this reaction however, and new experimental data was recommended by Iliadis et al. (2011).

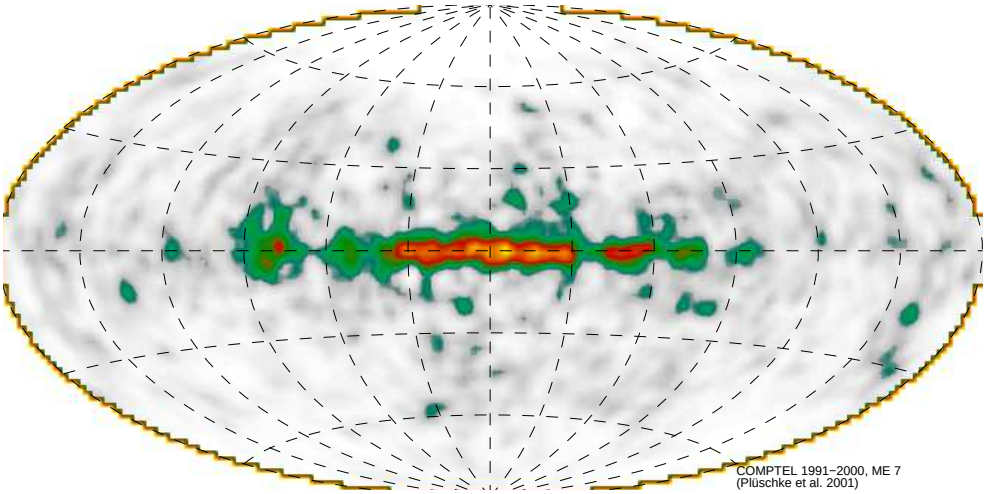

Figure 3.2: ^{26}Al distribution observed in the COMPTEL 1.809 MeV survey (Plüschke et al., 2001).

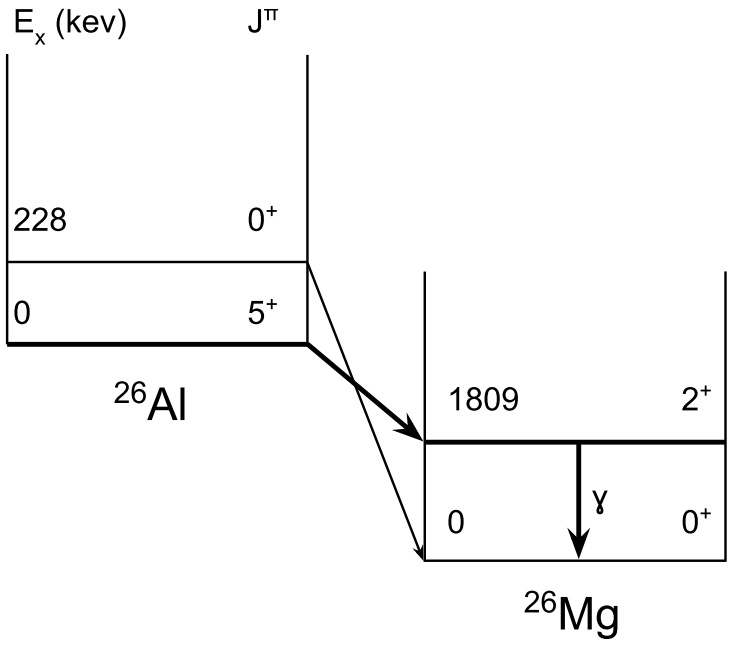

Figure 3.3: Decay scheme of ^{26}Al to ^{26}Mg.

Table 3.1: Changes in abundances of ^{26}Al (Iliadis et al., 2011).

Reaction	Rate Multiplied By				Experimental	Uncertainty
	10	2	0.5	0.1		
^{23}Na$(p,\alpha)^{20}$Ne	0.15	0.61	1.6	4.2	Yes[1]	6%
^{26}Al$(n,p)^{26}$Mg	0.16	0.65	1.4	1.9	Hybrid[2]	—[5]
^{25}Mg$(p,\gamma)^{26}$Al	6.2	2.0	0.46	0.10	Yes[1]	5%
^{23}**Na**$(\alpha,p)^{26}$**Mg**	3.0	1.3	...	0.71	No[3]	—[5]
^{26}Mg$(\alpha,n)^{29}$Si	0.40	0.83	...	1.3	Yes[4]	29%

[1] Iliadis et al. (2010)
[2] Experimental below $T \approx 0.2$ GK, Iliadis et al. (2011)
[3] Rauscher & Thielemann (2000)
[4] Angulo et al. (1999)
[5] Uncertainty is difficult to quantify

3.2 Early Experiments

The earliest measurement of the ^{23}Na$(\alpha,p)^{26}$Mg reaction was performed by Kuperus (1964), who measured the resonance strengths of reactions producing ^{26}Mg in its ground state (p_0 protons). These measurements covered a range of $E_\alpha = 1 - 3.3$ MeV. The reaction has a positive Q-value of 1.820 MeV. For resonances sufficiently isolated, angular distributions were measured via six silicon surface-barrier detectors positioned at angles of 172, 150, 135, 120, 87 and 40 degrees with respect to the beam. Forward-backward symmetry of the angular distributions was also investigated by comparing the yield of the 40° detector with the other detectors. A yield curve is shown in figure 3.4, where at least 38 resonances were identified, with 21 sufficiently resolved for angular distribution analysis. Two resonances, at $E_\alpha = 2.695$ and 3.194 MeV showed deviation from forward-backward symmetry.

This experiment was followed up by Whitmire & Davids (1974), who measured resonance strengths of reactions producing ^{26}Mg in its first excited state (p_1 protons). In addition, they calculated a stellar reaction rate based on their data. Measurements were performed over a range $E_\alpha = 2.3 - 3.7$ MeV, with six silicon detectors located at 45, 65, 85, 105, 125 and 145 degrees. A charged particle spectrum is shown in figure 3.5, and a p_0 yield curve in figure 3.6. Because Whitmire did not reproduce the p_0 data that was published by Kuperus, and because of a common experimental technique, they will be analysed as one combined data set of both p_0 and p_1 data.

Yields (Y) measured by both Whitmire & Kuperus were converted into resonance strengths ($\omega\gamma$) using the relationship

$$\frac{Y_1}{Y_2} = \frac{E_2}{E_1}\frac{(\omega\gamma)_1}{(\omega\gamma)_2}\,, \tag{3.1}$$

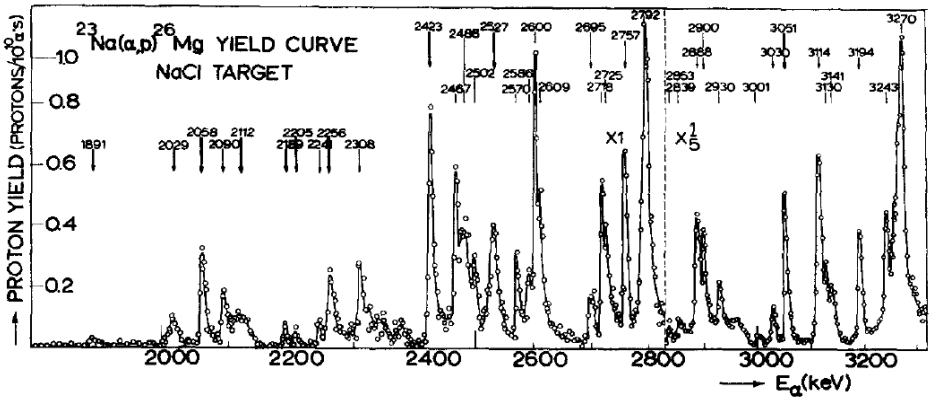

Figure 3.4: Resonance yields of the $^{23}\mathrm{Na}(\alpha, p)^{26}\mathrm{Mg}$ reaction over the range $E_\alpha = 1 - 3.3$ MeV, measured by Kuperus (1964).

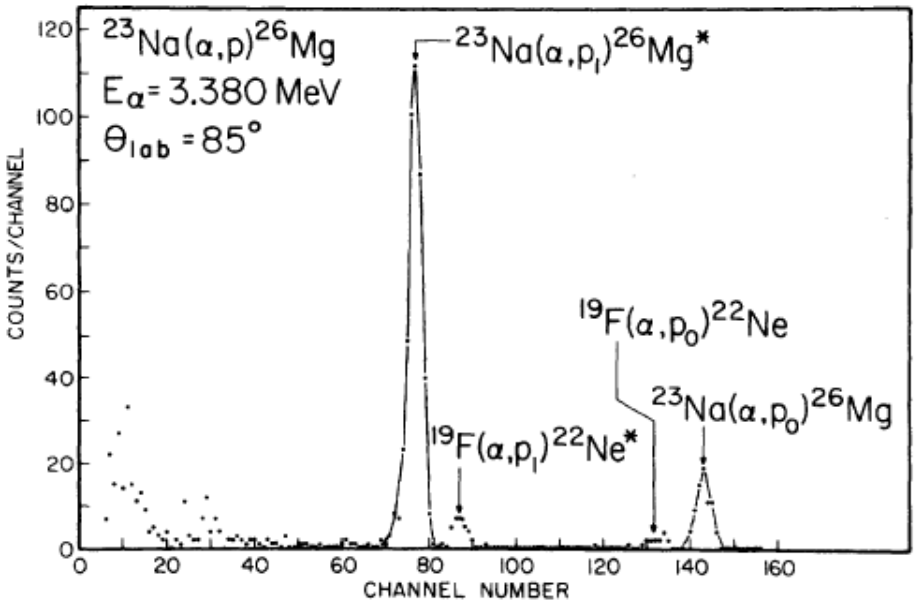

Figure 3.5: Charged particle spectrum measured by Whitmire & Davids (1974). The protons producing $^{26}\mathrm{Mg}$ in both its ground state and its first excited state can be observed.

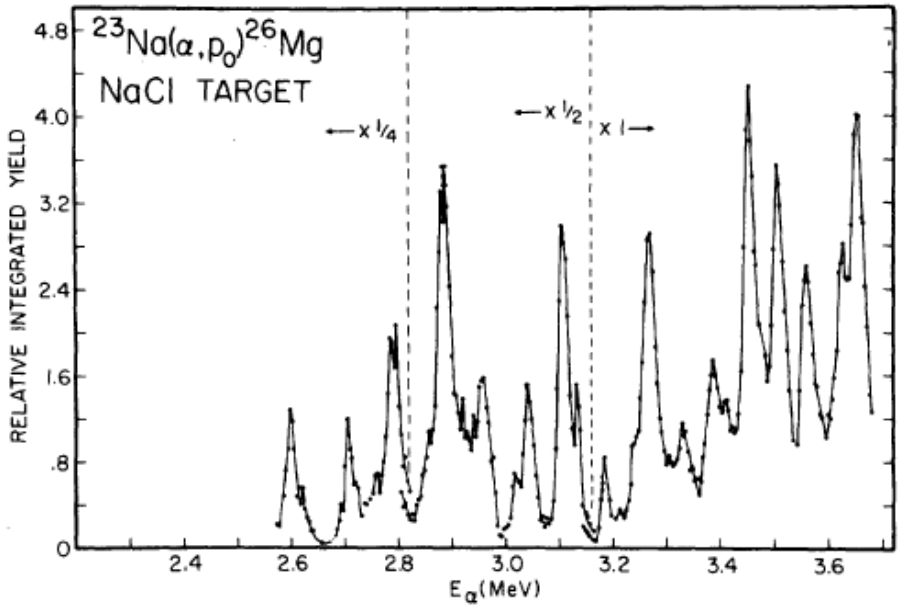

Figure 3.6: Resonance yields of the ^{23}Na$(\alpha, p)^{26}$Mg reaction over the range $E_\alpha = 2.3 - 3.7$ MeV, measured by Whitmire & Davids (1974).

where E is the laboratory bombarding energy of the resonance. An absolute measurement of $\omega\gamma$ was obtained by the thick-target yield for the strong 3.051 MeV resonance:

$$\omega\gamma = (2J_{23}+1)(2J_\alpha+1)\frac{M_\alpha}{\pi^2\hbar^2}\epsilon(E_\alpha)\frac{e}{Q}E_\alpha Y(\infty)\ , \tag{3.2}$$

where $Y(\infty)$ is the step in the yield over the resonance, J_{23} is the spin of ^{23}Na, J_α is the spin of 4He, M_α is the mass, ϵ is the stopping power of NaCl in units of energy$\times$length^2/atom, e is the electronic charge, and Q is the total charge collected. The published resonance strengths can be converted back into yields, in order to calculate cross-sections via equation 2.2.

The experiments were performed in standard kinematics, with a ^{4}He beam on a NaCl target. Due to the experiments measuring the strengths of individual resonances, the targets involved were necessarily thin and measurements were taken with small increases in beam energy. In order to obtain statistics in reasonable time it was therefore necessary for the beam current to be very high, which unfortunately led to heating of the target and subsequent target degradation. Although this effect was noted by Whitmire, it was not quantified and thus led to a large systematic uncertainty. This led to reaction rate compilations preferring a reaction rate predicted from Hauser-Feshbach models.

3.3 Hauser-Feshbach and NON-SMOKER

The basics of Hauser-Fechbach theory are discussed in Chapter 2. Although the mathematics of Hauser-Feshbach theory is standard, the calculations depend on the transmission coefficients T and the level density ρ, which must be evaluated with accuracy for a range of nuclei. These properties differ between the various statistical model calculations available. The code NON-SMOKER was used by Rauscher & Thielemann (2000) to determine the reaction rates of a range of nuclei, including unstable nuclei with no experimental information. Global descriptions were therefore employed to minimise the overall error, even far from stability (Rauscher & Thielemann, 2000).

The transmission from an excited state (E, J, π) to the state $(E_i^\mu, J_i^\mu, \pi_i^\mu)$ in nucleus i via emission of particle j is given by the summation over all allowed partial waves

$$T_j^\mu(E, J, \pi, E_i^\mu, J_i^\mu, \pi_i^\mu) = \sum_{l=|J-s|}^{J+s} \sum_{s=|J_i^\mu - J_j|}^{J_i^\mu + J_j} T_{jls}(E_{ij}^\mu) \,, \tag{3.3}$$

where the angular momentum l and channel spin $s = J_j + J_i^\mu$ couple to $J = l + s$. The transition energy $E_{ij}^\mu = E - S_j - E_i^\mu$, where S_j is the channel separation energy. These transmission coefficients can then be summed into a total transmission coefficient T_o into channel o, where up to 19 experimentally known states are utilised up to state v_m, followed by an integration over the level density ρ for higher energies:

$$\begin{aligned} T_o(E, J, \pi) = &\sum_{\nu=0}^{v_m} T_o^\nu(E, J, \pi, E_m^\nu, E_m^\nu, \pi_m^\nu) \\ &+ \int_{E_m^{v_m}}^{E-S_{m,o}} \sum_{J_m, \pi_m} T_o(E, J, \pi, E_m, J_m, \pi_m) \times \rho(E_m, J_m, \pi_m) \, \mathrm{d}E_m \,. \end{aligned} \tag{3.4}$$

Experimental data are taken from Firestone (1996), up to the first level with unassigned spin. If ground state spins and parities are unavailable, they are taken from Möller et al. (1997). The individual particle transmission coefficients T_{jls} are calculated from optical potentials for the particle-nucleus interaction. For protons and neutrons the potential is given by Jeukenne et al. (1977), and for α-particles, such as for the $^{23}\mathrm{Na}(\alpha, p)^{26}\mathrm{Mg}$ reaction, the potential is from McFadden & Satchler (1966), however a more sophisticated potential may be necessary for heavily charged nuclei at astrophysical energies (Rauscher & Thielemann, 2000).

Level densities in the NON-SMOKER code are obtained from Rauscher et al. (1997), based on the Fermi-gas formalism, a phenomenological approach fitted to known level densities over a wide range of masses. Sophisticated

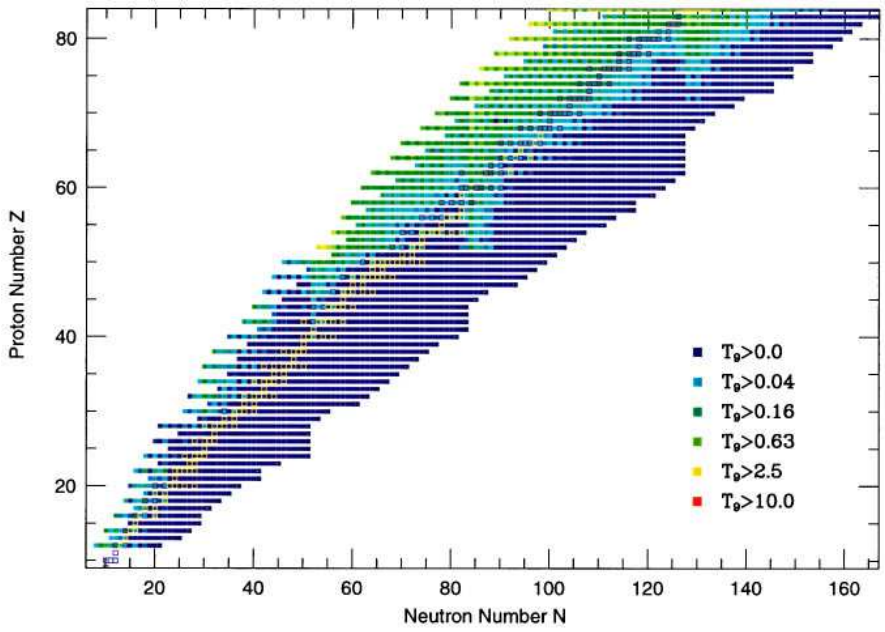

Figure 3.7: Minimum temperatures for applicability of statistical models for α-induced reactions. Figure by Rauscher et al. (1997).

Monte Carlo shell model calculations have shown excellent agreement with this approach for level densities. Compared to some Hauser-Feshbach codes, no experimental level density parameters were used for specific cases. The level density formalism depends on microscopic and pairing corrections, obtained from nuclear mass models. Where possible experimental masses were used, with the finite range droplet model (Möller et al., 1995) being used for other nuclei.

Hauser-Feshbach statistical models rely on the assumption that the average transmission coefficient 3.3 can be used. This is the case for high-level densities where resonances completely overlap. Level densities can be too low in the case of light nuclei, shell closures or reduced particle separation energies. In these cases single resonances and the direct reaction mechanism have to be taken into account. A quantitative criterion was derived in Rauscher et al. (1997), and shown for α-particle induced reactions in figure 3.7. The ^{23}Na$(\alpha, p)^{26}$Mg reaction's compound nucleus is ^{27}Al ($Z = 13, N = 14$) where the statistical model is observed to be usable above $T_9 > 0.63$, with the uncertainty caveats of α-induced reactions. Strong individual resonances observed in Whitmire & Davids (1974) may also affect the reliability of the statistical model, particularly considering the sensitivity of ^{23}Na and ^{26}Al production to the rate.

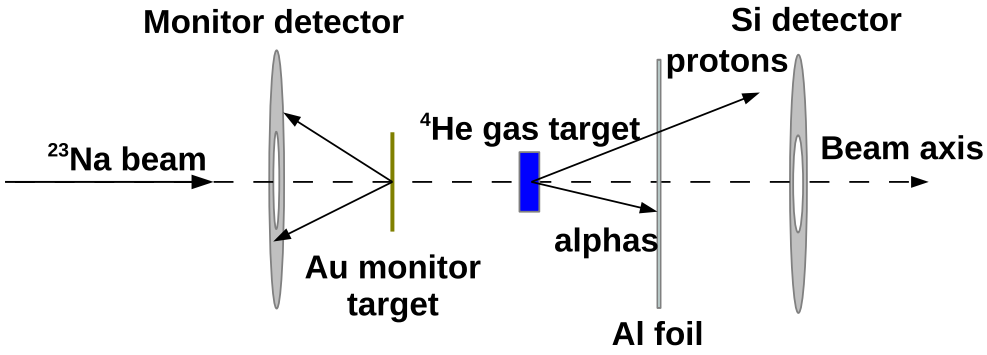

Figure 3.8: Schematic of the experimental setup, by Almaraz-Calderon et al. (2014).

3.4 Almaraz-Calderon et al., 2014

Based on the recommendations by Iliadis et al. (2011) and the weaknesses of the data by Kuperus (1964); Whitmire & Davids (1974) a new experimental measurement of the ^{23}Na$(\alpha,p)^{26}$Mg reaction was performed by Almaraz-Calderon et al. (2014) at Argonne National Laboratory (ANL) near Chicago, USA. This experiment was performed in inverse kinematics, utilising a ^{23}Na beam on a ^{4}He cryogenic gas target. This setup avoids the target deterioration issues experienced by Kuperus and Whitmire, eliminating that large source of uncertainty on their measurements. Measurements were made over the range of $E_{cm} = 1.3$ to 2.5 MeV, with beam energies of 23, 26, 28 and 30 MeV. The target had an effective thickness of 59 μg/cm^2. An annular 500 μm silicon strip detector measured the protons, covering an angular range of $\theta_{lab} = 6.8°$ to 13.5°. A second 300 μm thick silicon detector was placed upstream, along with a Au foil, in order to monitor beam intensity via Rutherford backscattering. A schematic of the setup is shown in figure 3.8.

Proton yields to both the ground state (p_0) and first excited state (p_1) of ^{26}Mg were extracted for the two higher beam energies. For the 26 MeV beam energy, p_1 protons were obscured from background protons from the gas target window. For the lowest energy no significant signal was observed and only an upper limit was quoted. The rings of the segmented silicon detector were grouped into 4 sets of 4 rings, and the combined yield for each group was used to determine four differential cross-sections. As the experimental setup can only observe protons emitted at angles of $\theta_{cm} \geq 160°$, it was necessary to assume an angular distribution in order to obtain total cross-sections. The distribution was assumed to be the same as the ^{27}Al$(\alpha,p)^{30}$Si reaction, the distribution and the measured differential cross-sections are shown in figure 3.9.

The parameters obtained from this previously measured angular distribution (Spasskii et al., 1968) were normalised to the measured differential

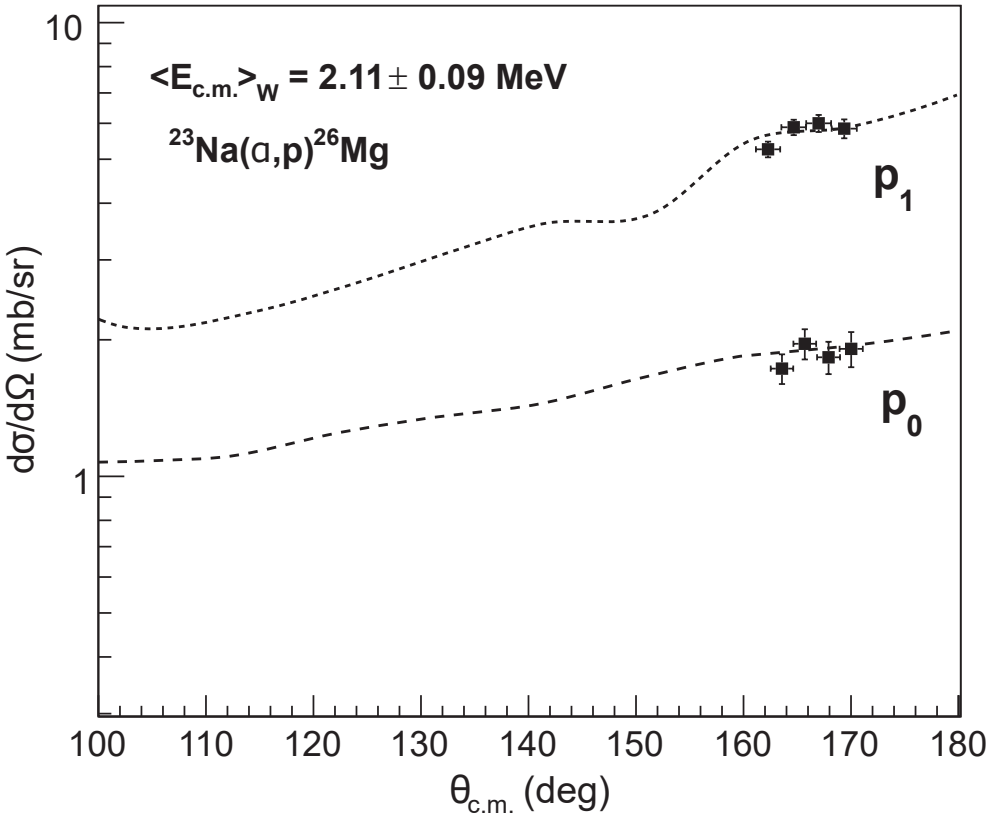

Figure 3.9: Measured differential cross-section, and assumed angular distribution, by Almaraz-Calderon et al. (2014).

cross-section data, and integrated in order to obtain the total cross-sections. An uncertainty of 50% was assigned to these values. These total cross-sections are shown in figure 3.10, where they were observed to be a factor of 40 higher than those predicted by HF models, and over 100 higher than those measured by Whitmire. This discrepancy is very large to be attributed to target degradation issues in Whitmire, and is a much larger discrepancy than expected from the statistical model calculations. An experimental reaction rate was also obtained, which was significantly larger than the factor of 10 increase necessary to change the abundance of ^{26}Al by a factor of 3 (Almaraz-Calderon et al., 2014).

3.5 New Measurement at Aarhus University

A summary of the cross-sections in 2014 is shown in figure 3.11, with very large discrepancies between the three sets. The significantly increased cross-sections in Almaraz-Calderon et al. (2014) were unexpected, and much larger than the assumed uncertainties in Hauser-Feshbach models and the assumed

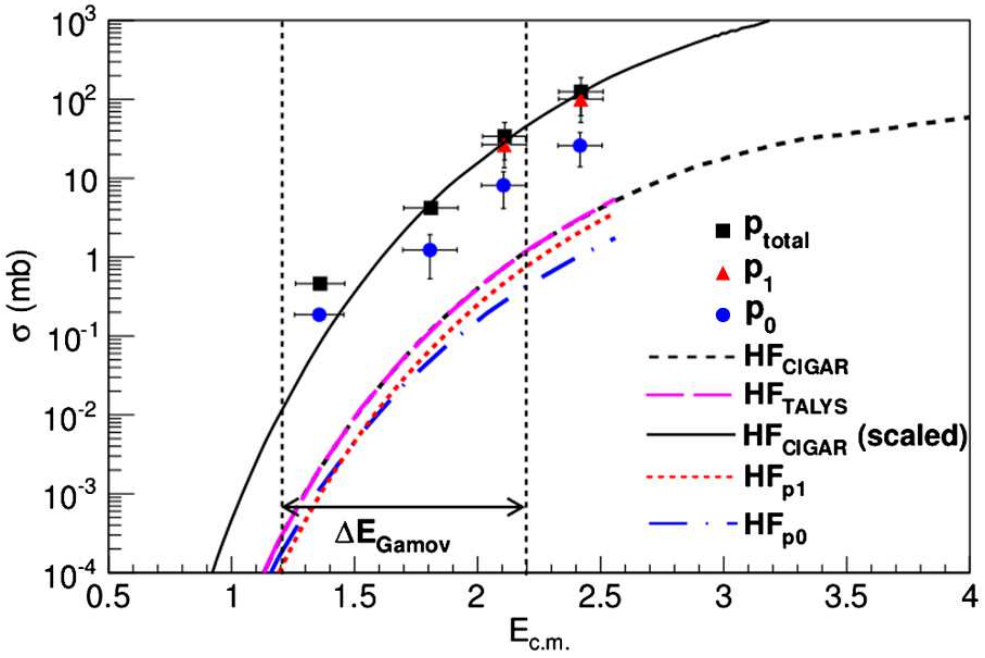

Figure 3.10: Cross-sections for the ^{23}Na$(\alpha, p)^{26}$Mg reaction, measured by Almaraz-Calderon et al. (2014).

degradation in Kuperus (1964); Whitmire & Davids (1974). An analysis of α-induced reactions by Mohr (2015) also observed that the Almaraz-Calderon et al. (2014) measurements were inconsistent with the trend of most reactions, with the only other inconsistent reactions being from old and unreliable experimental data.

Due to these issues, a new measurement of the ^{23}Na$(\alpha, p)^{26}$Mg was performed at Aarhus University, in Denmark. The experiment was performed in forward kinematics as with Whitmire & Kuperus, but with reduced beam intensities and direct monitoring of the target during the experiment, in order to correct for any target deterioration that may occur. Unlike Whitmire & Kuperus our focus was on total cross-sections and comparison with Almaraz-Calderon et al. (2014), rather than individual resonance strength measurements. In addition, the larger, segmented charged particle detectors available allowed the direct measurement of angular distributions, removing the uncertainty on assumed angular distributions in the work by Almaraz-Calderon et al. (2014).

3.6 Measurement at TRIUMF

At the same time as the measurement at Aarhus University, an independent measurement of the ^{23}Na$(\alpha, p)^{26}$Mg reaction was also being performed at TRI-

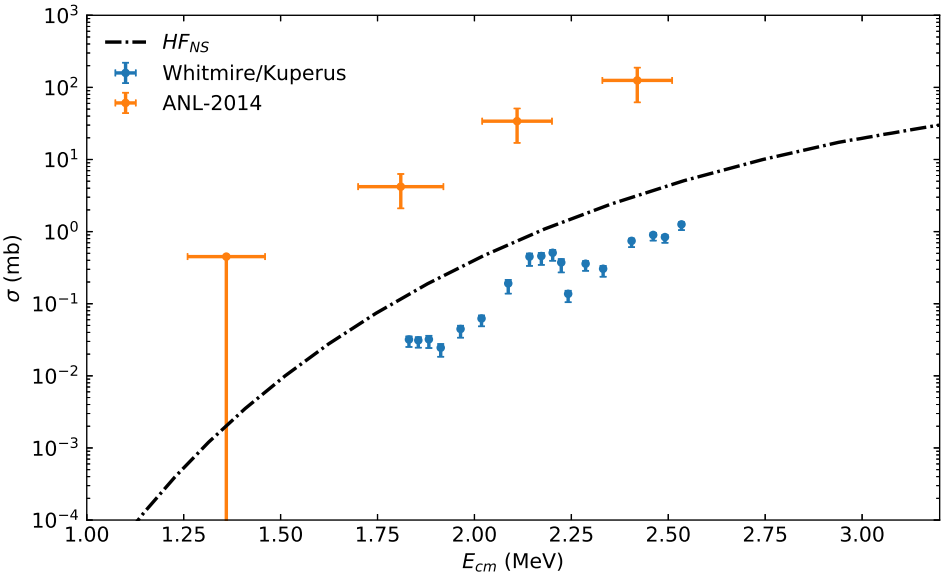

Figure 3.11: Summary of cross-section data for the ^{23}Na$(\alpha, p)^{26}$Mg reaction in 2014.

UMF, Canada and published in parallel to the present work, as presented in chapter 4. The TRIUMF experiment is described in detail by Tomlinson (2015). The TRIUMF experiment was performed in inverse kinematics using the TRIUMF-UK Detector Array (TUDA), a 1.5 m long scattering chamber which houses an array of charged particle detectors. The target was a gas target with 147 mbar of ^{4}He, a 4 μm titanium entrance window was used in order to replicate the setup utilised by Almaraz-Calderon et al. (2014) (Tomlinson, 2015). The charged particles produced by the reactions were detected by silicon detectors, using a $\Delta E - E$ configuration to perform particle identification. Beam intensity was monitored by the Louvain-Edinburgh Detector array (LEDA) placed upstream of the target to monitor backscattering (Tomlinson, 2015). The setup is shown in figure 3.12. Beam energies between 1.2 and 1.7 MeV/u were utilised, and protons to the ground state and first two excited states of ^{26}Mg were measured. The results were published by Tomlinson et al. (2015) and are discussed and compared with other measurements in chapter 5.

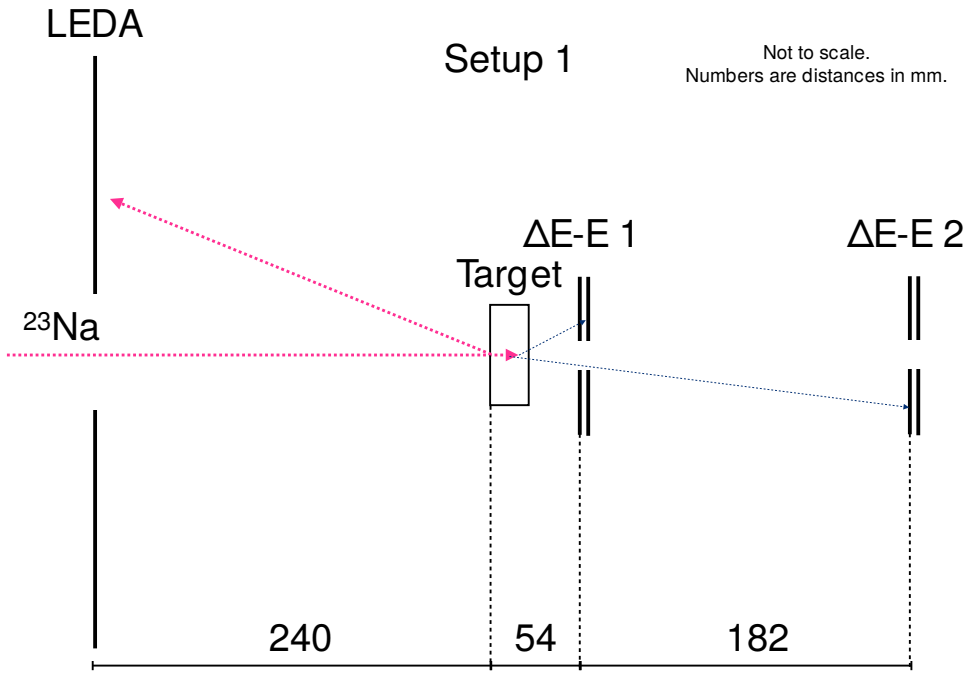

Figure 3.12: Experimental setup of the $^{23}\mathrm{Na}(\alpha, p)^{26}\mathrm{Mg}$ measurement at TRIUMF, figure from Tomlinson (2015).

Chapter 4

Experimental Analysis

4.1 Experimental Setup at Aarhus University

The new $^{23}\mathrm{Na}(\alpha, p)^{26}\mathrm{Mg}$ reaction measurement was performed at Aarhus University utilising their 5 MV Van de Graaf accelerator located at the Department of Physics and Astronomy, shown in figure 4.1. This particle accelerator is a small electrostatic accelerator that works by accelerating ions through a static electric potential generated by a Van de Graaf belt. As the name implies, the maximum voltage produced is 5 MV, although in practice the usable voltages are lower, typically on the order of 1 to 3 MV. The ions themselves come from a bottle of helium gas which is ionised to the 1^+ state by an ECR ion source, and are thus accelerated between 1 and 3 MeV. For this experiment the alpha energy ranged from 1.99 to 2.94 MeV.

These α-particles then impinged on a locally produced NaCl target with a nominal thickness of 70 μg/cm^2. Because cross-sections depend on a good measurement of the target thickness, measurements of the target thickness were made during the experiment, and are discussed in section 4.2. This target was rotated at 45° with respect to the beam axis, which increases the effective thickness by a factor of $\sqrt{2}$. Surrounding the target were two sets of silicon detectors: one 322 μm annular Micron Semiconductor S3 double-sided silicon strip detector (DSSD) located at 180° covering angles between 140° and 163°, and one 'telescope' detector comprised of a thin 40 μm square Micron W1 DSSD backed by a thick 1500 μm square pad detector located at 90° covering angles between 60° and 120°. The experimental setup is shown in figure 4.2.

The telescope detector allows particle identification via the two separate detectors: α-particles have a much greater stopping power and will by fully stopped in the thin W1 detector at the front, whereas protons will deposit only part of their energy in the thin W1 detector, and deposit the rest in the backing pad detector; their position can still be identified from the W1 detector. This particle identification helps discriminate between the elastically

Figure 4.1: Picture of the 5 MV Van de Graaf Accelerator at Aarhus University.

scattered α-particles and the protons produced by the reaction.

The S3 detector does not have such particle identification capabilities, separation of the protons from the α-particles was achieved by mounting the detector "backwards", with the junction side facing the target (Howard et al., 2015). This side has a very large 4 μm dead-layer (region where energy deposited cannot be measured), and thus acts as a degrader foil. As the α-particles have a greater stopping power they will be more degraded in this dead-layer, increasing the separation between backscattered α-particles and protons.

After the detector set-up, the beam passes to a Faraday cup which measures the current precisely. This cup is connected to a current integrator to measure the total beam charge over the run. Typical beam currents were in the range of $200 - 500$ ppA.

When a charged particle interacts with the silicon detector, it generates a charge in the detector proportional to the deposited energy. This charge is collected by Mesytec MPR-16 charge-sensitive preamplifiers, which produce and amplify a voltage proportional to the charge in the detector. These signals are further amplified by Mesytec MSCF-16 shaping amplifiers, which also reshape the signal to a Gaussian pulse whose maximum voltage is proportional to the particle energy. These shaped signals then enter a set of CAEN V785 ADCs which digitise the peak height into a 12-bit value, corresponding to 4096 voltage divisions between 0 and 4 V. These ADCs are connected via a

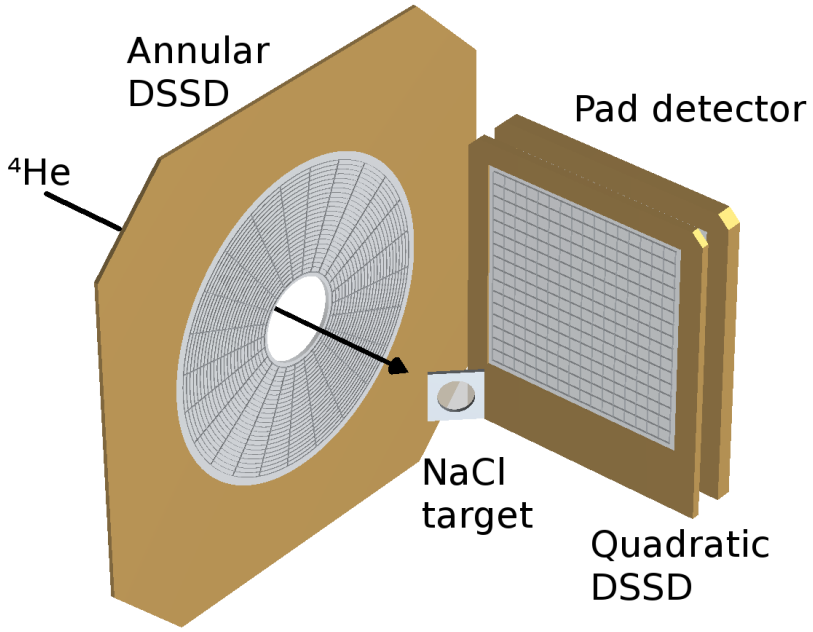

Figure 4.2: Schematic of the experimental setup at Aarhus University. The incoming ^{4}He is incident on a thin NaCl target and the emitted protons and scattered α-particles are detected by the two DSSDs. Figure by Howard et al. (2015).

VME bus to a computer running the data acquisition program MIDAS, which records the ADC values into a data file for subsequent analysis.

4.2 Target Thickness and Composition

In order to obtain differential cross-sections it is necessary to know the thickness of the target. Although the thickness was estimated at 70 μg/cm^2 during production, this measurement was very crude and in order to obtain a good uncertainty it is necessary to remeasure the target thickness more precisely.

The method used involved measuring the energy loss via α-particles backscattered from the 10 μg/cm^2 carbon backing of the foil. The target is rotated through 180° and the energy peak then shifts due to the losses in the NaCl layer. This technique has been discussed before by Chiari et al. (2001), and is shown in figure 4.3. A figure comparing the elastic scattering peak at 0 and 180 degrees is shown in figure 4.4. The target thickness t depends on the incident angle (θ_i) of the beam alpha particles, the detected angle (θ_d) of the scattered α-particles, the energy shift (ΔE) and the stopping power of

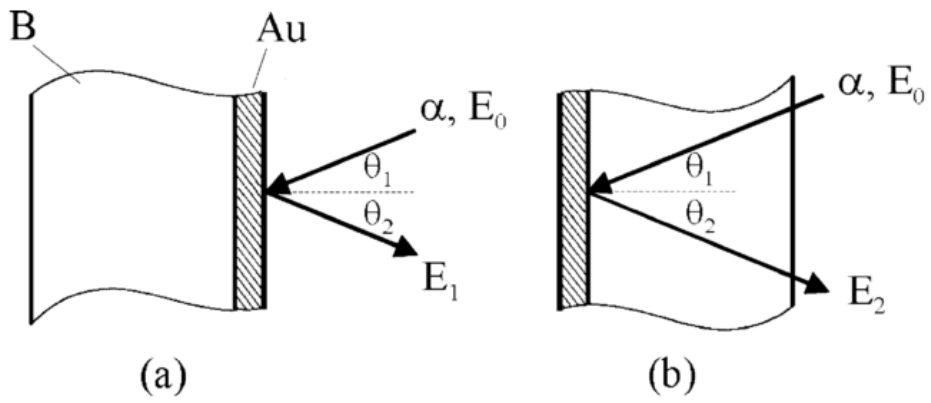

Figure 4.3: Illustration of the energy loss method for determining target thickness, by Chiari et al. (2001). Scattered α-particles from the backing (Au in Chiari's experiment) lose energy if the target is oriented with the target material (B) facing the beam, depending on the thickness. In the present work the backing is C and the target material is NaCl.

α-particles in sodium ($S(E)$):

$$t = \frac{\Delta E(\theta)}{S(E)} \frac{1}{\left[\frac{1}{\cos\theta_i} + \frac{1}{\cos\theta_d}\right]} \,. \tag{4.1}$$

At 3 MeV the energy loss was measured to be 65 keV, corresponding to a thickness of 76 μg/cm^2. Because the target was rotated during the experiment, this results in an effective thickness corresponding to an energy loss of between 92 and 115 keV depending on the beam energy.

Monitoring of the target composition and thickness during the experiment was a focus of the experimental planning, motivated by the large target degradation observed in the earlier experiments by Kuperus (1964); Whitmire & Davids (1974) which contributed to their unsuitability. Due to the ability of the detector set-up to discriminate between α-particles and protons, Rutherford scattering was used to monitor the target during the experiment. First of all the intensity of the observed scattered α-particles was compared to the Rutherford scattering formula to confirm the suitability:

$$\frac{\mathrm{d}\sigma}{\mathrm{d}\Omega} = \left(\frac{Z_1 Z_2 \alpha \hbar c}{4E_\alpha \sin^2(\theta/2)}\right)^2 \,. \tag{4.2}$$

Afterwards the separate yields from scattering on both the Na and Cl can be used to determine the stoichiometric composition of the target. Observation of this ratio over beam current showed that the composition was not changing with beam, and thus degradation was not an issue in the experiment. This

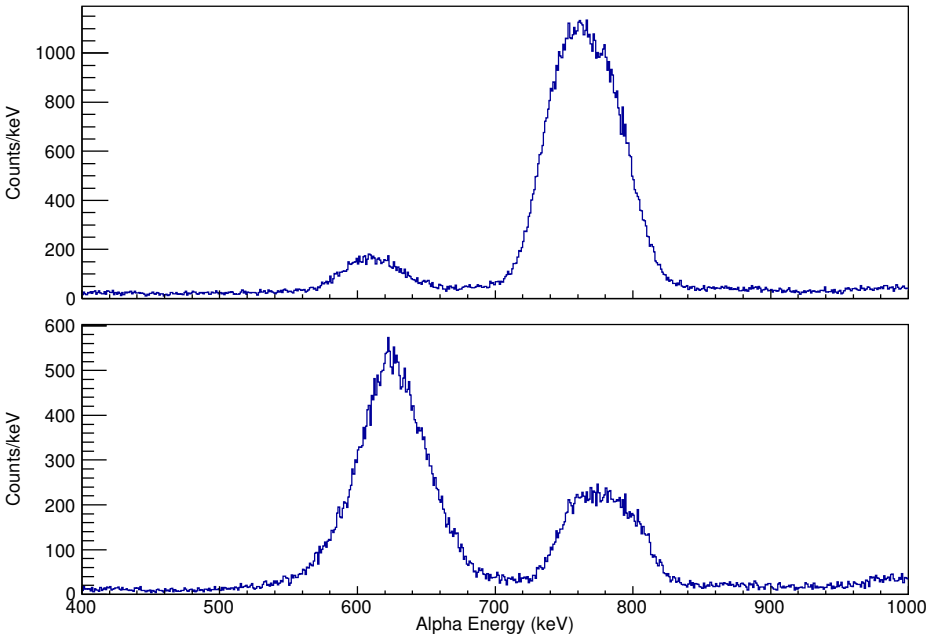

Figure 4.4: Spectra of the peak corresponding to elastically scattered alpha particles from ^{12}C at 180° (top; where the C layer faces the beam) and at 0° (bottom; where the NaCl layer faces the beam). When passing through the NaCl layer the peak is shifted down in energy depending on the thickness of the layer, allowing the thickness to be calculated.

was not unexpected due to the much lower beam currents employed compared to the earlier experiments. The Rutherford scattering data was furthermore employed to normalise yields to cross-sections, as this eliminated systematic uncertainties in the target thickness and the integrated beam current. The target composition analysis is shown in figure 4.5.

4.3 Yield Analysis

An example spectrum of the protons is shown in figure 4.6. The energy response of the silicon detectors was pre-calibrated by using a triple-α (Am, Pt, Cu) radioactive source before the experiment began. The energies detected in the S3 detector were corrected for a measured 3550 nm dead layer, while the W1/PAD detectors were assumed to have negligible dead layer loss for protons. The W1/PAD telescope required a coincidence in both the W1 and the PAD for proton events, and no PAD event for α-particle events. For the S3 detector all events were analysed under the assumption that they arose from protons, with α-particles subsequently discriminated against based on the deposited energy, as illustrated in figure 4.6.

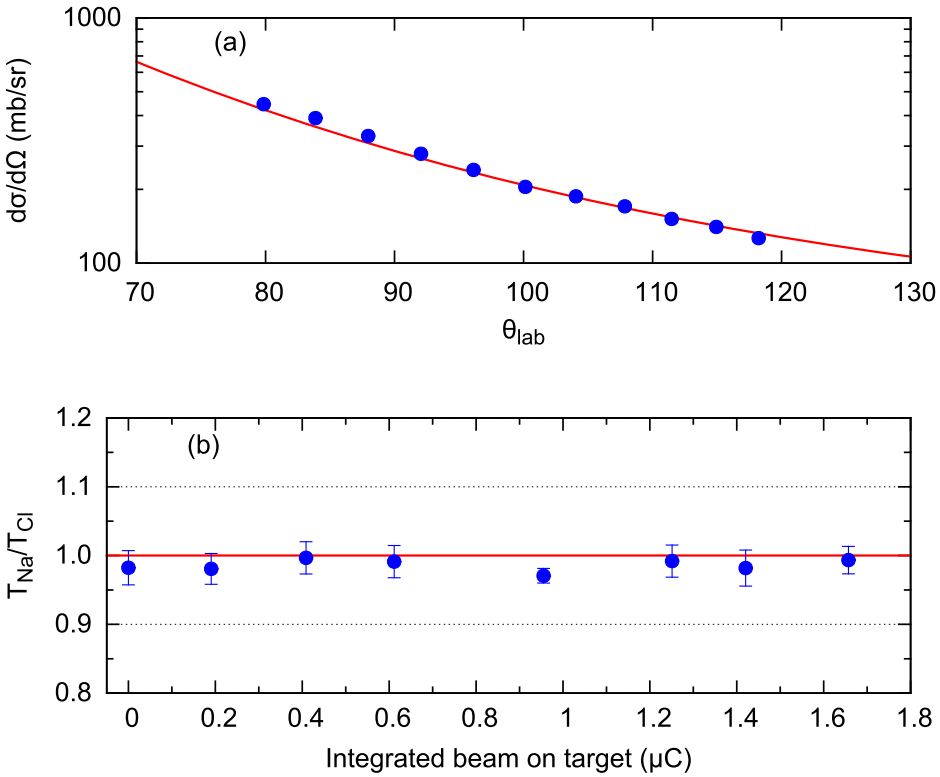

Figure 4.5: Figure from Howard et al. (2015) showing the results from target composition analysis. (a) Shows the measured differential cross-section from elastic scattering reproducing the predicted Rutherford distribution (red line). (b) Shows the ratio of the thicknesses of Na and Cl from the Rutherford cross-section with integrated beam on target. The ratio is consistent throughout the experiment, indicating no target deterioration is present.

The angle of the detected proton was determined from the hit pixel of the detector and the geometry of the set-up, with the solid angle evaluated by sampling random positions within each detector pixel. The energies, angles and solid angles were converted into centre-of-mass coordinates for evaluation of the differential cross-section. These corrections ensure that data from different pixels with the same angle can be combined properly.

Energy spectra for a number of centre-of-mass energies are shown in figure 4.6. The energy of the peaks was compared to the predicted proton energy of the $^{23}\mathrm{Na}(\alpha,p)^{26}\mathrm{Mg}$ reaction from kinematic calculations, confirming the p_0 and p_1 peaks as highlighted.

The small peak at * is at the energy expected from the $^{19}\mathrm{F}(\alpha,p_0)^{22}\mathrm{Ne}$ reaction, and is indicative of small F contamination within the NaCl target. The $^{19}\mathrm{F}(\alpha,p_1)^{22}\mathrm{Ne}$ component is expected to overlap with the $^{23}\mathrm{Na}(\alpha,p_1)^{26}\mathrm{Mg}$ peak, potentially increasing observed yields slightly. The intensity of the F

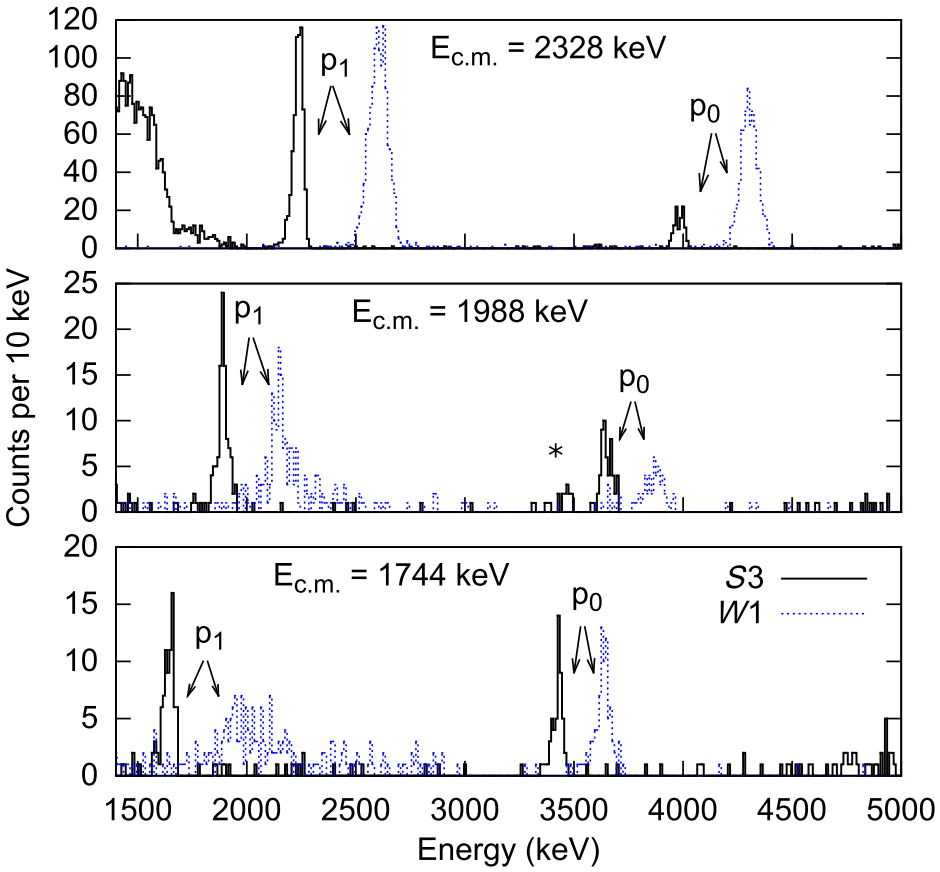

Figure 4.6: Figure from Howard et al. (2015) showing the proton energy spectra. α-scattering background is visible in the S3 detector at low particle energies, well separated from proton events.

contamination peak is approximately 10% as intense as the Na peak, and hence a conservative uncertainty of 10% was added to the lower limits of the p_1 cross-sections. The F peak is not seen in the upper and lower plots of figure 4.6 due to the smaller size of the Na peak, and corresponding much smaller size of the F peak.

The yields of protons to higher excited states (p_2, etc) were not observed in this experiment due to their energy being too low, and thus they appear under the background produced by scattered α-particles, which became significant at low count rates.

For each beam energy used, the data is associated with an energy corresponding to the average energy throughout the target. However because the cross-section is also energy dependent, this average is ideally weighted for the cross-sections, obtaining the typical energy for the cross-section measurement. In order to calculate this weighted energy 5 equally spaced energy steps cov-

ering the energy range within the target were taken, and the cross-section from NON-SMOKER was obtained at these energies, via linear interpolation if necessary. The weighted average was then taken for these 5 energy steps in order to obtain the cross-section weighted average energy.

4.4 Angular Distributions and Total Cross-Sections

The yields (Y) for each set of angles can be directly converted into differential cross-sections by taking into account the solid angle of the detectors at each angle ($\Delta\Omega$), the target thickness in ions/cm^2 (N) and the integrated beam current in ions (I), assuming an intrinsic detector efficiency of 100%:

$$\frac{\mathrm{d}\sigma}{\mathrm{d}\Omega} = \frac{Y}{IN\Delta\Omega} \ . \tag{4.3}$$

At energies below $E_{cm} = 1.9$ MeV the p_1 protons did not exit the W1 detector with sufficient energy to register within the subsequent PAD detector, resulting in a drop in the detector efficiency that is not easily quantified. For this reason only protons detected in the S3 detector in the region of $140° - 160°$ were measured at these energies, limiting the possible angular distribution analysis.

At the higher energies, a full angular distribution was obtained by fitting the differential cross-sections to a sum of the first four even Legendre polynomials:

$$\frac{\mathrm{d}\sigma}{\mathrm{d}\Omega} = a + bP_2(\cos(\theta)) + cP_4(\cos(\theta)) + dP_6(\cos(\theta)) \ , \tag{4.4}$$

which can then be integrated to obtain the total cross-section.

$$\sigma = \int_0^{2\pi} \int_0^{\pi} \frac{\mathrm{d}\sigma}{\mathrm{d}\Omega} \sin(\theta) \ \mathrm{d}\theta \mathrm{d}\phi \ , \tag{4.5}$$

which for the Legendre polynomials above, simplifies to:

$$\sigma = 4\pi a \ . \tag{4.6}$$

The even Legendre polynomials are symmetric around 90°, which is expected for a reaction such as this which produces an intermediate compound nucleus. The experimental data from Kuperus (1964) investigated any asymmetry around 90° and only identified a small asymmetry with one state, nonetheless to account for this a systematic uncertainty of 20% was included in the error analysis.

For the low energies where the p_1 protons could only be measured at large angles, an isotropic distribution was assumed. By comparing this assumption

Table 4.1: Angle-integrated cross-sections and their total errors.

E_{cm} (keV)	σ_{p0} (mb)	σ_{p1} (mb)	σ_{tot} (mb)
1744	$0.05(1)^{\text{stat}}(1)^{\text{sys}}$	$0.06(1)^{\text{stat}}(^{+2}_{-2})^{\text{sys}}$	$0.11(1)^{\text{stat}}(^{+2}_{-2})^{\text{sys}}$
1831	$0.11(1)^{\text{stat}}(2)^{\text{sys}}$	$0.20(1)^{\text{stat}}(^{+6}_{-6})^{\text{sys}}$	$0.31(1)^{\text{stat}}(^{+6}_{-6})^{\text{sys}}$
1998	$0.09(1)^{\text{stat}}(2)^{\text{sys}}$	$0.26(5)^{\text{stat}}(^{+5}_{-6})^{\text{sys}}$	$0.35(5)^{\text{stat}}(^{+5}_{-6})^{\text{sys}}$
2071	$0.22(2)^{\text{stat}}(4)^{\text{sys}}$	$0.56(4)^{\text{stat}}(^{+11}_{-12})^{\text{sys}}$	$0.78(4)^{\text{stat}}(^{+12}_{-13})^{\text{sys}}$
2139	$0.34(4)^{\text{stat}}(7)^{\text{sys}}$	$2.80(20)^{\text{stat}}(^{+56}_{-62})^{\text{sys}}$	$3.14(20)^{\text{stat}}(^{+56}_{-62})^{\text{sys}}$
2328	$0.28(3)^{\text{stat}}(6)^{\text{sys}}$	$1.58(7)^{\text{stat}}(^{+32}_{-35})^{\text{sys}}$	$1.86(8)^{\text{stat}}(^{+33}_{-36})^{\text{sys}}$
2400	$0.62(4)^{\text{stat}}(12)^{\text{sys}}$	$1.52(9)^{\text{stat}}(^{+30}_{-33})^{\text{sys}}$	$2.14(10)^{\text{stat}}(^{+32}_{-35})^{\text{sys}}$
2469	$1.76(8)^{\text{stat}}(35)^{\text{sys}}$	$3.05(9)^{\text{stat}}(^{+61}_{-67})^{\text{sys}}$	$4.81(12)^{\text{stat}}(^{+70}_{-76})^{\text{sys}}$

with the fitted distributions at higher energies, the isotropic distributions result in a 30% lower cross-section. The cross-sections at $E_{cm} < 1.9$ MeV were corrected for this 30% decrease and have a systematic uncertainty of 30% included.

The angular distributions and the Legendre fits at all the measured beam energies are shown in figure 4.7. The total cross-sections obtained from the integration, and their uncertainties are shown in table 4.1.

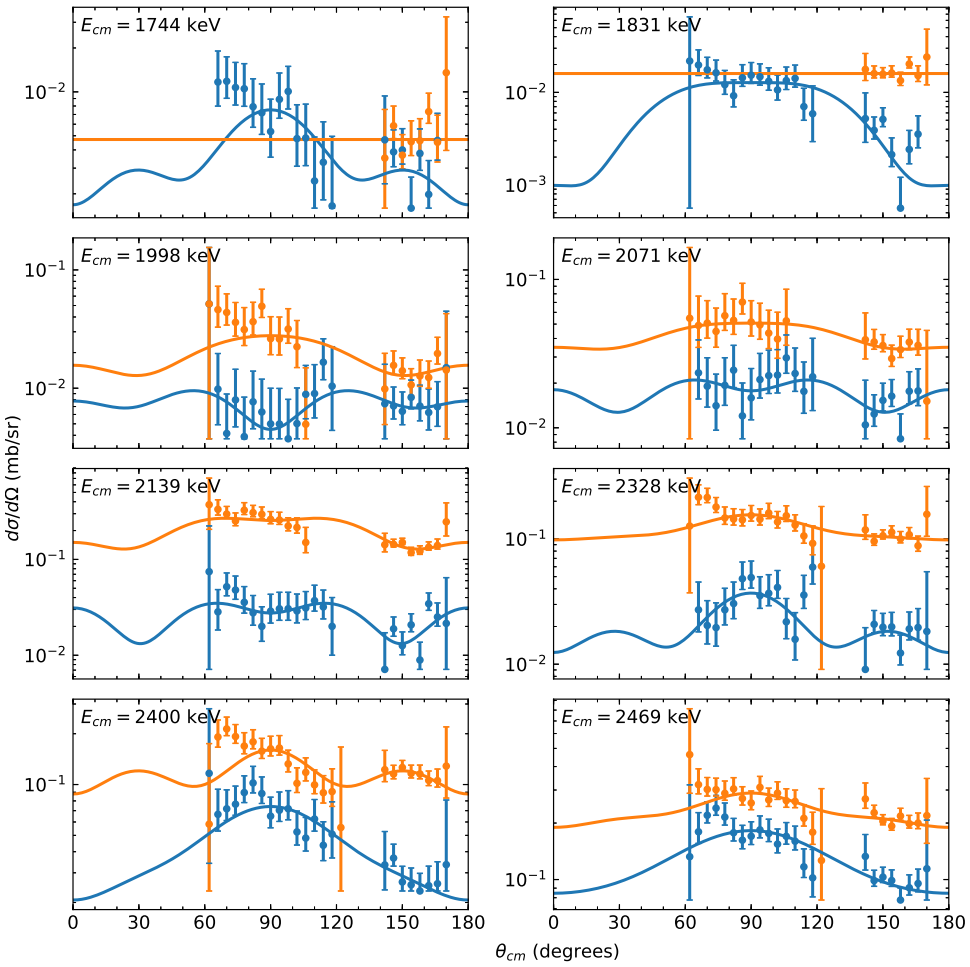

Figure 4.7: Angular distributions for the $^{23}\mathrm{Na}(\alpha, p)^{26}\mathrm{Mg}$ reaction measured at Aarhus University for centre-of-mass energies of 1744–2469 keV. The red data points are p_1 protons and the blue data points are p_0 protons. The lines correspond to Legendre polynomial fits to data points of the same colour.

Chapter 5

Astrophysical Impact

5.1 Corrected Cross-Sections

Alongside our work described in chapter 4 and Howard et al. (2015), an additional experiment was performed and analysed at the same time by Tomlinson et al. (2015). This experiment was performed in inverse kinematics and used a very similar experimental set-up to that of Almaraz-Calderon et al. (2014). The cross-sections were measured assuming an isotropic angular distribution, and total cross-sections consistent with our work and the Hauser-Feshbach (HF) models were obtained.

Following the publication of our results (Howard et al., 2015) and the TRIUMF results (Tomlinson et al., 2015), the data from Almaraz-Calderon et al. (2014) was reanalysed (Almaraz-Calderon et al., 2015). A systematic error was identified in the beam current integration leading to a factor of 100 increase in the measured cross-sections, and so the work was re-evaluated with cross-sections 100× smaller than originally published. These new cross-sections are consistent with our measurements.

All available modern experimental data for the ^{23}Na$(\alpha,p)^{26}$Mg reaction, along with the HF predicted cross-section, is shown in figure 5.1. The agreement is reasonable but there are still noticeable differences between the data. Some of this can be accounted for due to the fact that both Almaraz-Calderon et al. (2015) and Tomlinson et al. (2015) measured cross-sections over a very narrow angular range, and thus had to assume an angular distribution in order to obtain total cross-sections. Because the present work directly measured the angular distributions as shown in figure 4.7, we can apply these distributions to the other data sets to correct for this systematic uncertainty.

To perform this correction our angular distributions were additionally fitted to isotropic distributions using the high angle data only. This yields cross-sections equivalent to those obtained by Tomlinson et al. (2015) who assumed an isotropic distribution. For the data by Almaraz-Calderon et al. (2015) a distribution based on ^{27}Al$(\alpha,p)^{30}$Si was used, so instead a set of isotropic

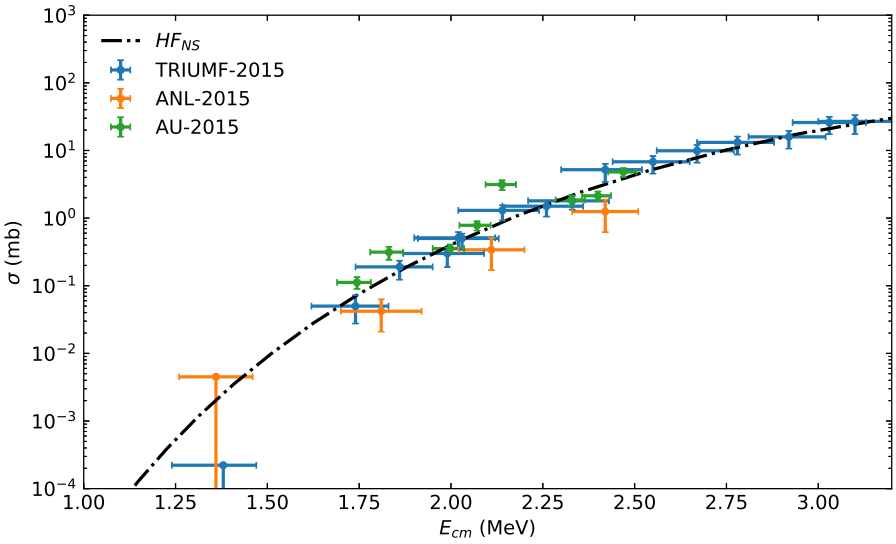

Figure 5.1: Published cross-sections for the ^{23}Na$(\alpha,p)^{26}$Mg reaction by Almaraz-Calderon et al. (2015) (ANL-2015), Tomlinson et al. (2015) (TRIUMF-2015), Howard et al. (2015) (AU-2015), and compared to the statistical cross-sections predicted by the Hauser-Feshbach code NON-SMOKER (HF_{NS}). These measurements have all been performed independently and are largely consistent. The discrepancies remaining between the three data sets are discussed in text.

cross-sections was calculated from the published differential cross-section data.

The summary of the cross-sections calculated, including isotropic cross-sections and ratio is shown in table 5.1. From this we find that on average the true cross-section is approximately 30% larger than the isotropic assumption, and approximately 250% larger than the distribution assumed by Almaraz-Calderon et al. (2015). The outlier at $E_{cm} = 1831$ keV is due to a strong resonance at 1800 keV which produces a nearly pure $\ell = 1$ distribution, which drops off strongly at angles above 120°.

The experimentally measured cross-sections for all three modern data sets, corrected for the angular distributions, is shown in figure 5.2, and a much better agreement between all the data sets is observed. The lowest energy point is an upper limit and therefore also fully consistent.

5.2 Combined Reaction Rate with Other Experimental Measurements

For the ^{23}Na$(\alpha,p)^{26}$Mg reaction in the C/Ne convective shell ($T_9 \approx 1.4$) the Gamow window is 1.8 ± 0.5 MeV, which has been directly measured by the

Table 5.1: Angle-integrated cross-sections compared to cross-sections utilising an isotropic assumption. All cross-sections are in mb.

E_{cm} (keV)	σ_{p0}	σ_{p0}^{ISO}	$\sigma_{p0}/\sigma_{p0}^{ISO}$	σ_{p1}	σ_{p1}^{ISO}	$\sigma_{p1}/\sigma_{p1}^{ISO}$
1744	0.05(1)	0.04	1.50	$0.06(^{+2}_{-2})$	—	—
1831	0.11(2)	0.02	4.88	$0.20(^{+6}_{-6})$	—	—
1998	0.09(2)	0.09	1.06	$0.26(^{+7}_{-8})$	0.17	1.57
2071	0.22(4)	0.17	1.33	$0.56(^{+12}_{-13})$	0.43	1.29
2139	0.34(8)	0.20	1.73	$2.80(^{+59}_{-65})$	1.68	1.66
2328	0.28(7)	0.22	1.26	$1.58(^{+33}_{-36})$	1.30	1.22
2400	0.62(13)	0.34	1.84	$1.52(^{+31}_{-34})$	1.45	1.04
2469	1.76(36)	1.19	1.49	$3.05(^{+62}_{-68})$	2.61	1.17

experimental work above. The experimental data and its uncertainties are therefore going to dominate the true stellar reaction rate and its uncertainties.

In order to obtain the reaction rate from the experimental cross-sections the convolution shown in equation 2.49 must be performed over a range of temperatures where the reaction is believed to occur. For the ^{23}Na$(\alpha,p)^{26}$Mg reaction this range is $T_9 = 1.0 - 2.5$ GK. Because the cross-section data is not a simple analytic function this convolution is performed by numerical integration.

This reaction rate is tabulated for temperatures in the range of $T_9 = 1.0 - 2.5$ GK by using the FORTRAN code EXP2RATE (Rauscher, 2003), which automatically performs the S-factor conversion above. Errors on the reaction rate are also computed incorporating the errors on both the energies (E_{cm}) and cross-sections (σ_{tot}). The tabulated reaction rates are calculated for the three experimental data sets separately, and are then combined by taking the weighted average to obtain the combined experimental reaction rate. This combined rate is shown in figure 5.3

For most astrophysical models, a large reaction database such as REACLIB (Cybert et al., 2010) is used. These databases store the reaction rates for isotopes as coefficients to the function:

$$N_A\langle\sigma v\rangle = \exp\left[a_0 + \sum_{i=1}^{5} a_i T_9^{\frac{2i-5}{3}} + a_6 \ln\left(T_9\right)\right], \tag{5.1}$$

which accurately captures the temperature dependence of most reaction rates (Cybert et al., 2010). The combined tabulated ^{23}Na$(\alpha,p)^{26}$Mg reaction rate was fitted to this function using the Computation Infrastructure for Nuclear Astrophysics (CINA) system (Smith et al., 2004), and the coefficients obtained are tabulated in table 5.2

The reverse reaction rate, ^{26}Mg$(p,\alpha)^{23}$Na, is similarly calculated from the same data by utilising the reciprocity theorem as discussed in chapter 2. The

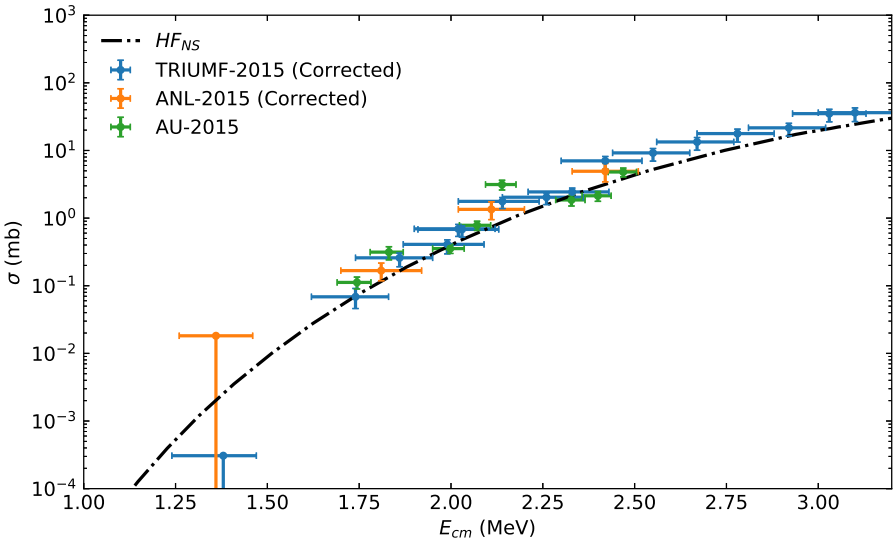

Figure 5.2: Cross-sections for the ^{23}Na$(\alpha, p)^{26}$Mg reaction by Almaraz-Calderon et al. (2015) (ANL-2015), Tomlinson et al. (2015) (TRIUMF-2015), Howard et al. (2015) (AU-2015), and compared to the statistical cross-sections predicted by the Hauser-Feshbach code NON-SMOKER (HF_{NS}). The measured cross-sections for TRIUMF-2015 and ANL-2015 have been corrected for assumed angular distributions using directly measured distributions from AU-2015. The three corrected data sets are fully consistent within error.

Table 5.2: REACLIB (Cybert et al., 2010) coefficients of equation 5.1 for the ^{23}Na$(\alpha, p)^{26}$Mg reaction.

	Recommended Rate	Lower Limit	Upper Limit
a_0	0.121543×10^3	0.956302×10^2	0.144559×10^3
a_1	-0.332135×10^2	-0.641287×10^2	0.493696×10^1
a_2	0.604369×10^3	0.130912×10^4	-0.278552×10^3
a_3	-0.735190×10^3	-0.141396×10^4	0.126051×10^3
a_4	0.390392×10^2	0.714716×10^2	-0.259029×10^1
a_5	-0.236980×10^1	-0.425212×10^1	0.725512×10^{-1}
a_6	0.397412×10^3	0.798600×10^3	-0.108493×10^3

partition functions $G(T)$ are interpolated from the tabulated data (Rauscher & Thielemann, 2000) for the appropriate temperatures. The reverse reaction rate was also fitted using the CINA system and the coefficients obtained shown in table 5.3. Both sets of coefficients can then be inserted into a REACLIB database for astrophysical modelling.

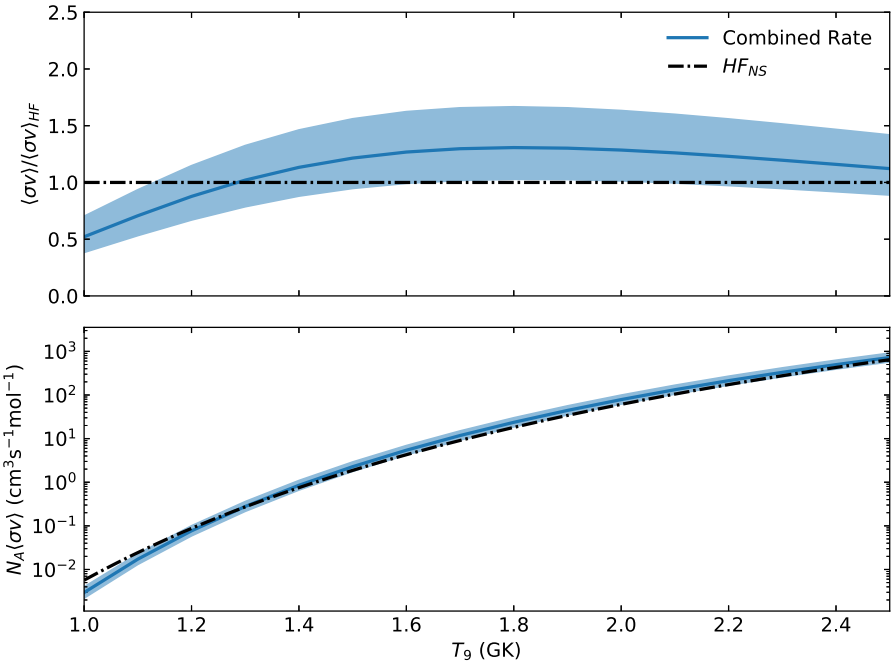

Figure 5.3: Experimental reaction rate and its uncertainty for the ^{23}Na$(\alpha, p)^{26}$Mg reaction relative to HF (top) and absolute (bottom). This rate is obtained by taking the weighted average of the reaction rates for the three/four sets of corrected cross-sections.

Table 5.3: REACLIB (Cybert et al., 2010) coefficients of equation 5.1 for the ^{26}Mg$(p, \alpha)^{23}$Na reverse reaction. Untabulated coefficients are identical to those in table 5.2.

	Recommended Rate	Lower Limit	Upper Limit
a_0^{rev}	0.124121×10^3	0.982085×10^2	0.147137×10^3
a_1^{rev}	-0.543414×10^2	-0.852566×10^2	-0.16191×10^2

5.3 Astrophysical Modelling: NuGrid and PPN

The NuGrid project is a set of tools for large scale nucleosynthesis post-processing in stellar scenarios. Post-processing involves taking a precomputed model of a star's evolution and calculating a large network of reaction rates over this evolution path in order to obtain isotopic abundances. For reasons of computation time a full stellar model will only include the nuclear reactions important to energy generation within a star – the ones that drive the stellar evolution. In comparison, a post-processing code does not need to model the hydrodynamics of the star and can take into account a much larger number of reactions and isotopes, usually many 1000s, although studies cannot be done of reactions which drive stellar evolution in post-processing (for example a study of the $^{12}C + {}^{12}C$ rate would not be feasible in post-processing.).

The principal software programs of NuGrid are the related PPN and MPPNP. Both programs perform the post-processing of reactions on a 1D stellar model output, and use the same set of physics to do so. Their difference is that PPN operates in a single "zone" (thin mass shell), using the temperature, pressure and density at that coordinate for each point in time to calculate reaction rates. MPPNP on the other hand is a parallel multi-zone calculation which can incorporate mixing at each time step into the calculation, using mixing coefficients produced from the stellar model input. As PPN is a single zone code it is able to perform calculations very quickly, making it ideal for initial analysis and sensitivity studies. Comparatively, MPPNP requires much more time and processing power to run (usually on large cluster computers), but produces a more elaborate study of isotopic abundances in regions where mixing effects can be important. A schematic of the two programs is shown in figure 5.4.

One of the main inputs into PPN aside from the stellar model is the set of reaction rates used in post-processing, which primarily come from the REACLIB reaction database, storing data as coefficients to equation 5.1. In order to analyse the impact of the $^{23}Na(\alpha, p)^{26}Mg$ reaction multiple sets of REACLIB databases were produced: using the original REACLIB rate from HF calculations, using the experimental rate and reverse rate, using the lower limit of the experimental rate, and using the upper limit of the experimental rate. By investigating abundances from all four of these rates we can not only see any changes in abundance with the new experimental rate, but more importantly, provide constraints on isotopic abundances with the reduced uncertainty on the experimental rate compared to the HF rate.

Based on previous sensitivity studies the main stellar scenarios which are affected by the $^{23}Na(\alpha, p)^{26}Mg$ rate are massive stars (Iliadis et al., 2011) and type 1 supernovae (Bravo & Martínez-Pinedo, 2012). Both of these scenarios were investigated to determine the impact of the new rate.

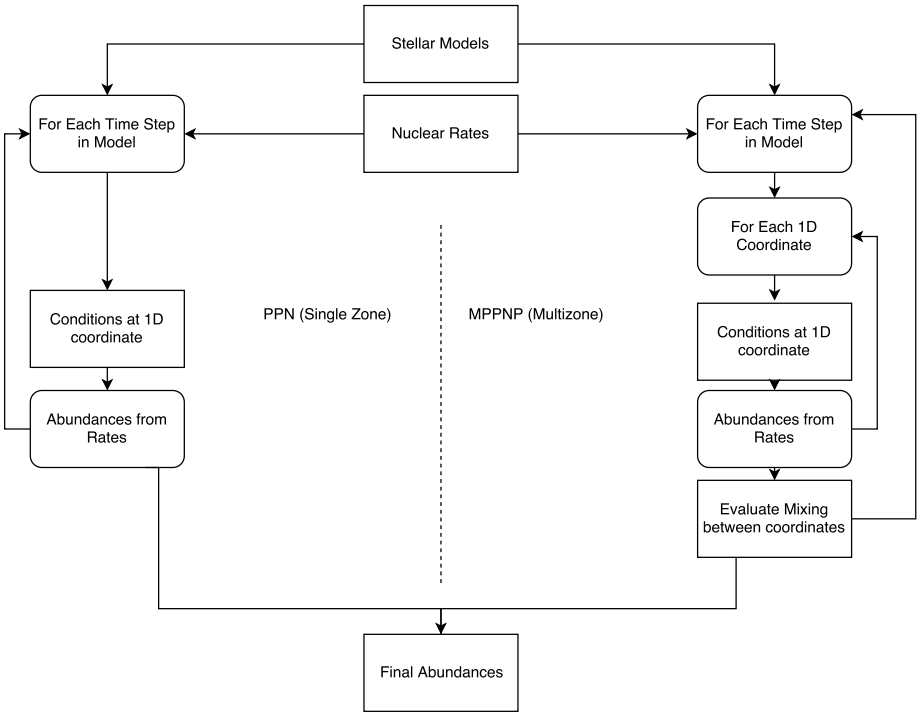

Figure 5.4: Schematic of the NuGrid software suite, highlighting the interplay between individual components. Both the multi-zone (MPPNP) and single-zone (PPN) use a shared physics (reaction rates, etc) and solver (coupled differential equation solver) package to calculate the isotopic abundances.

5.4 Massive Stars

The massive star models were based on initial stellar input produced by the code GENEC (Eggenberger et al., 2008), which are included as part of the NuGrid stellar data set 1 (Pignatari et al., 2016). Two models were used for the studies: a $60M_{\odot}$ star and a $25M_{\odot}$ star, both with a near solar metallicity of $Z = 0.02$. The HR diagram of the $60M_{\odot}$ star's evolution is shown in figure 5.5. The PPN calculations are performed on 1D trajectories extracted from previously post-processed stellar model data from MPPNP.

From this MPPNP data, a specific mass coordinate and time range is chosen, which corresponds to the deepest area of the C/Ne convective shell. This is identified by the use of a Kippenhahn diagram, which clearly identifies the individual shells and stages of a star's evolution, figure 5.6. At these mass coordinates (vertical axis) and times (horizontal axis) within the desired range the temperature, density and pressure are extracted to form a 1D trajectory (t, T, P, ρ) for PPN. In addition, the isotopic abundance at the start of the desired time is extracted to provide the initial abundance for PPN. PPN is then run with a network of 1100 isotopes with changes solely to the $^{23}\mathrm{Na}(\alpha, p)^{26}\mathrm{Mg}$

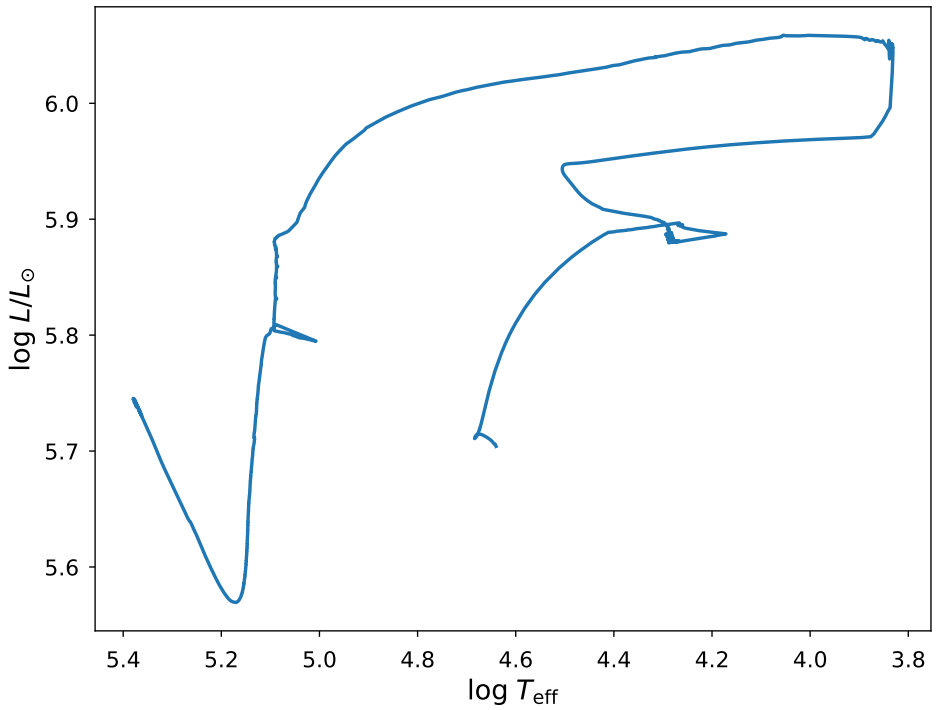

Figure 5.5: Hertzprung-Russell (HR) diagram for the $60M_\odot$ star as simulated by the code GENEC (Eggenberger et al., 2008) and used as input for the reaction rate impact calculations.

reaction and its time reverse reaction.

A total of seven PPN evaluations were performed for evaluation of the impact: The original NON-SMOKER rate and its best case upper & lower limits (a factor of 2 scaling), the new combined experimental reaction rate and its upper and lower limits, and the rate from Almaraz-Calderon et al. (2014). From these seven evaluations the abundance of elements relative to solar was obtained, shown in figure 5.7. This graph shows the elemental abundance in the C/Ne shell and highlights the shell as a source of Na and Al production (including ^{26}Al). However due to the scale it can be hard to identify differences between the present work and NON-SMOKER, as expected due to the similar cross-sections. The differences between the present work and the ANL-2014 rate is significant though, with the ANL-2014 producing a significant decrease in the abundance of sodium. The same evaluations were performed on a $25M_\odot$ star as well, shown in figure 5.8. The same impact on the ^{23}Na$(\alpha, p)^{26}$Mg rate is observed between the two models.

A comparison of abundances relative to the original NON-SMOKER rate is shown in figure 5.9 where the impact of the rates and uncertainties is much clearer. In particular the uncertainty on elemental production is greatly re-

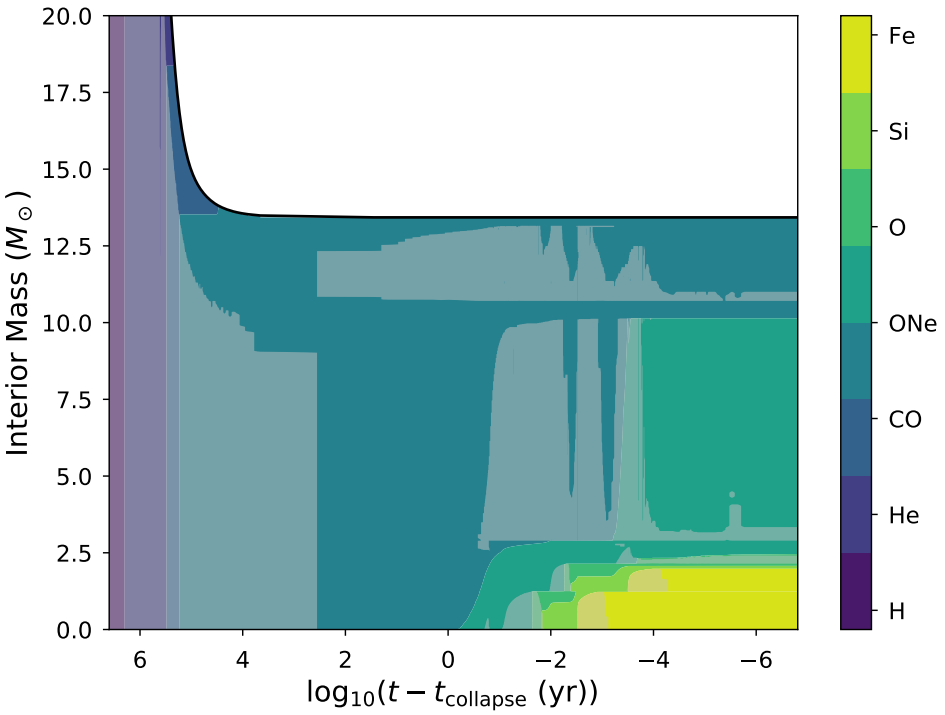

Figure 5.6: Kippenhahn diagram of the $60M_\odot$ star, showing the entire evolution of the star. The individual burning shells are easily visible by the change in temperature (colour, related to primary isotope undergoing fusion) and the presence of convection (grey overlay).

duced with the new experimental rate, constraining abundance ratios to within 10%. The Na abundance is changed by a factor of $1.04(^{+8}_{-7})$ compared to the NON-SMOKER rate, and the ^{26}Al abundance changed by a factor $0.98(^{+8}_{-7})$. The impact on intermediate mass elements such as Ti is minimal.

5.5 Type 1a Supernovae

The impact on Type 1a supernovae was also evaluated in a similar way to the massive stars, although with some significant differences due to the nature of supernovae models. The model used is a 2D Chandrasekhar-mass deflagration-detonation transition (DDT) model by Parikh et al. (2013), which was subsequently analysed using Parikh's post-processing code. The results are shown in figure 5.10, and tabulated in 5.4. Only the ANL-2014 rate differs significantly from the NON-SMOKER rate: the radioisotopes ^{26}Al and ^{44}Ti are impacted, being a factor of two larger and 15% lower, respectively (Parikh, 2016). The uncertainty on the rate in the present work varies the

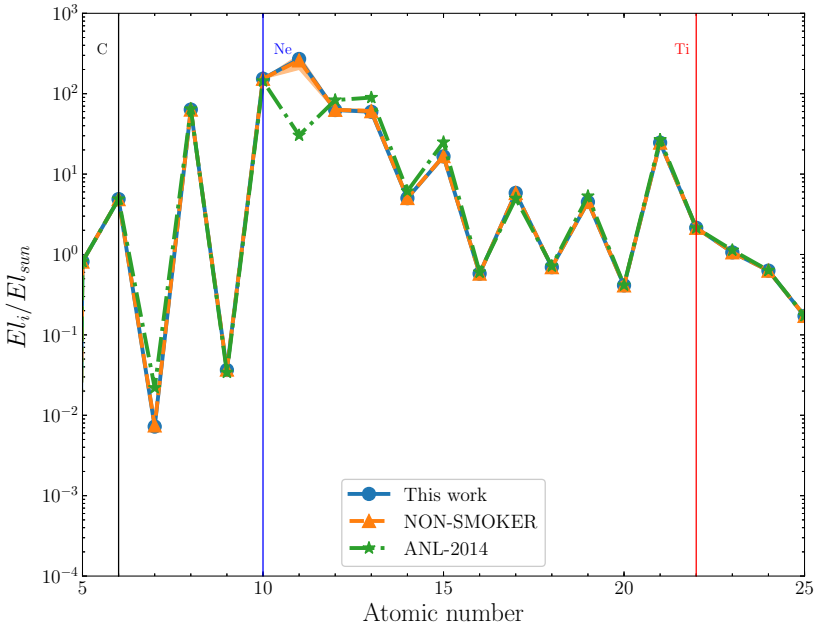

Figure 5.7: Abundances of elements in the $Z = 5 - 25$ region at the end of the C/Ne shell burning phase, relative to the solar abundance, for a $60M_{\odot}$ star. Differences between the present work and NON-SMOKER rates are more clearly highlighted in the relative abundances, figure 5.9.

amount of ^{23}Na by approximately 15%, whereas most other species are within 5% (Parikh, 2016).

5.6 Summary of Impact

The new experimental reaction rates for the $^{23}\mathrm{Na}(\alpha, p)^{26}\mathrm{Mg}$ reaction significantly reduce the uncertainty on light element production in massive stars and type 1a supernovae. The recommended rate itself differs only slightly from the previous rate from statistical models, but the uncertainty on those models can vary from a factor of 2 up to even a factor of 10 due to the low level density of the Na nucleus and the uncertainty of alpha induced reaction potentials.

In comparison, all the data sets are experimentally robust, being direct measurements of the reaction with few, if any, assumptions necessary to obtain a reaction rate. Therefore, the uncertainty is much less than before, evaluated at 30% primarily due to systematic effects of target thickness and contaminant

Table 5.4: Mass-fraction ratio of the present rate and the ANL-2014 rate compared to the previous HF rate, for mass numbers $A = 18 - 63$.

A	Present/HF	ANL-2014/HF
18	1.02	1.32
19	1.04	1.27
20	1.00	0.88
23	0.94	0.30
24	1.00	1.94
25	0.99	0.87
26	1.02	1.76
27	1.00	1.66
28	0.99	1.08
29	0.99	1.82
30	0.99	1.43
31	0.99	1.20
32	1.01	0.78
34	0.99	1.12
35	1.00	0.82
36	1.03	0.59
37	1.01	0.71
38	1.00	0.89
39	1.02	0.60
40	1.04	0.61
41	1.03	0.57
42	1.02	0.68
43	1.01	0.76
44	1.01	0.87
45	1.05	0.46
46	1.04	0.49
47	1.02	0.66
50	1.02	0.72
59	1.03	0.74
60	1.02	0.70
62	0.99	1.26
63	1.01	1.14

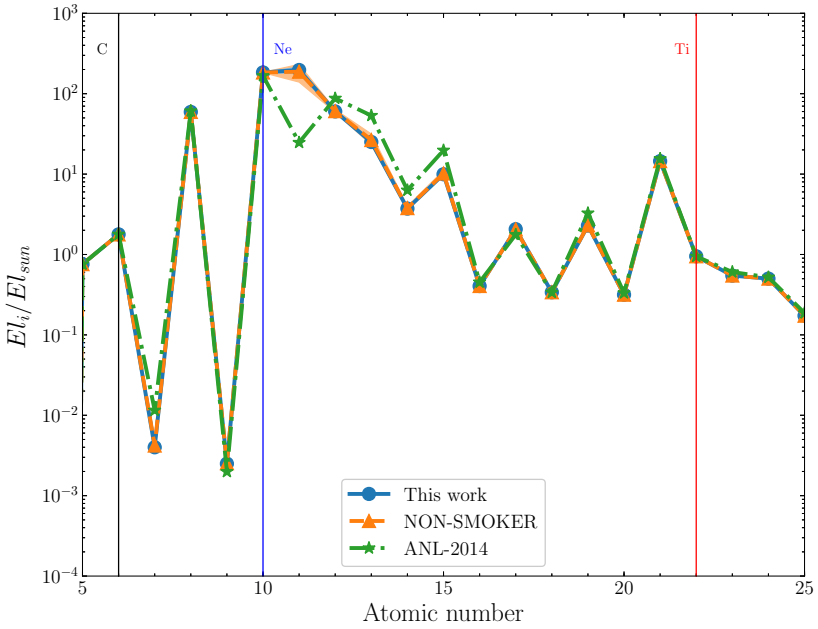

Figure 5.8: Abundances of elements in the $Z = 5-25$ region at the end of the C/Ne shell burning phase, relative to the solar abundance for a $25M_{\odot}$ star.

states. The data also confirm a reliable trend of α induced cross-sections at low energies by Mohr (2015), which was previously concerned with the high cross-sections measured by Almaraz-Calderon et al. (2014).

The elemental abundances have been evaluated through nuclear post-processing and most are now constrained to within 10% of the best estimate. The Na abundance is observed to increase slightly compared to the NON-SMOKER abundance, changing by a factor $1.04(^{+8}_{-7})$. The ^{26}Al abundance is changed by a factor $0.98(^{+8}_{-7})$. The uncertainty on the ^{26}Al abundance is now dependent only on uncertainties in other rates lacking good experimental data, some of which are highlighted by Iliadis et al. (2011). The discrepancy between observed Na abundance and that predicted by the rate measured by Almaraz-Calderon et al. (2014) is no longer present with the new combined rate.

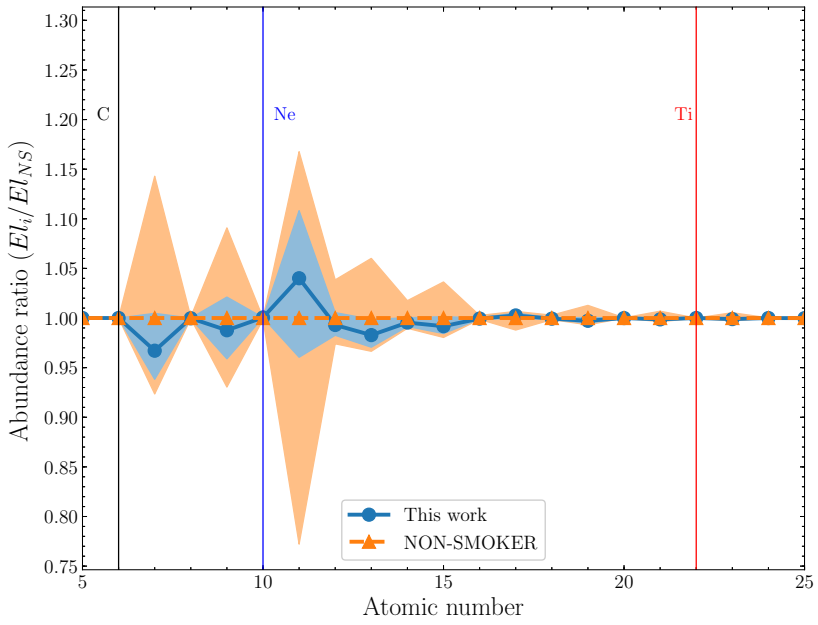

Figure 5.9: Abundances of elements in the $Z = 5-25$ region at the end of the C/Ne shell burning phase, for a $60M_{\odot}$ star, relative to the abundance produced by the NON-SMOKER reaction rate. The shaded region corresponds to the uncertainty of the rate.

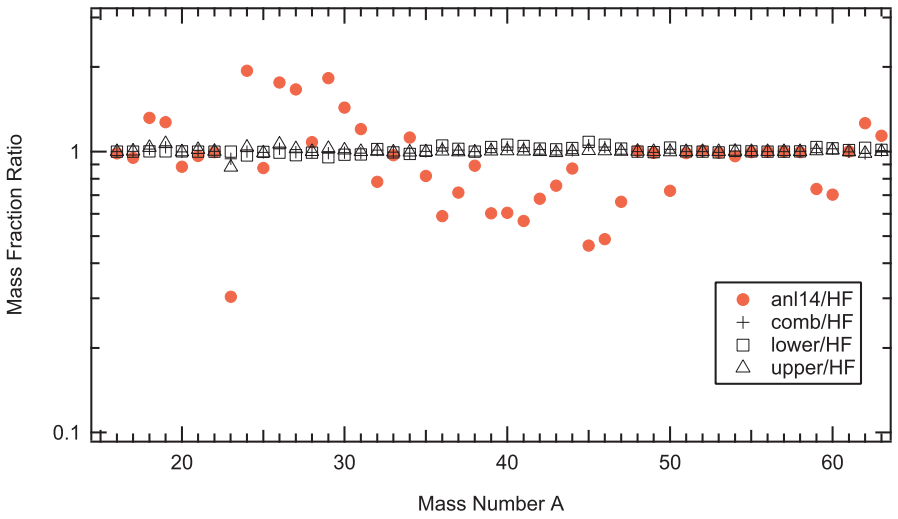

Figure 5.10: Figure of elemental abundance in a type 1 supernova (Parikh, 2016).

Part III

Studies of ^{12}C at iThemba LABS

Chapter 6

Search for the 0^- State

6.1 Motivation

As a light and stable nucleus, the low-lying states in ^{12}C are typically well studied, with the less understood states typically being those with a strong α-cluster nature. Single-particle shell-model-like states on the other hand tend to be well-studied, being well-populated by transfer reactions, having a narrow width, and providing clean identification by γ-ray decay: particularly below the proton-decay threshold at 16 MeV.

Despite this, a strong shell-model-like state, around the proton threshold, remains unidentified despite theoretical predictions. Shell-model calculations using the WBP and WBT interactions (Warburton & Brown, 1992) place the lowest 0^- ($T = 0$) state at $E = 15.1$ MeV (WBP) and $E = 16.3$ MeV (WBT). The ^{11}B(^{3}He,d)^{12}C reaction was identified as having a very high cross-section for the population of this state: the spectroscopic factor C^2S is 0.33 (WBP) and 0.26 (WBT), based on the addition of a proton in the $0d_{3/2}$ orbital to the ^{11}B $3/2^-$ ground state. This state has also been identified in no-core shell model calculations using the NNLO$_{\text{opt}}$ interaction (which included nucleon-nucleon interactions only) (Ekström et al., 2013), in these calculations the state is placed at $18.9 - 19.5$ MeV, above the proton threshold. Additionally, parity conversation dictates that a 0^- state in ^{12}C cannot undergo α-decay, and hence below the proton threshold must decay only via γ-decay. A summary of the predicted low-lying states in ^{12}C is shown in figure 6.1, the 0^- state of interest is highlighted in blue.

The ^{11}B(^{3}He,d)^{12}C reaction has been used in the past to study ^{12}C states that are well described via the proton transfer mechanism, such as the predicted 0^- state. The 14-16 MeV region, below the proton threshold and where the shell model places the states, has been studied via the ^{11}B(^{3}He,d)^{12}C reaction by Hinds & Middleton (1961); Bohne et al. (1968); Miller et al. (1969). The only state experimentally observed with uncertain properties is a narrow state at 14.7 MeV identified by Hinds & Middleton (1961), with a width of 15

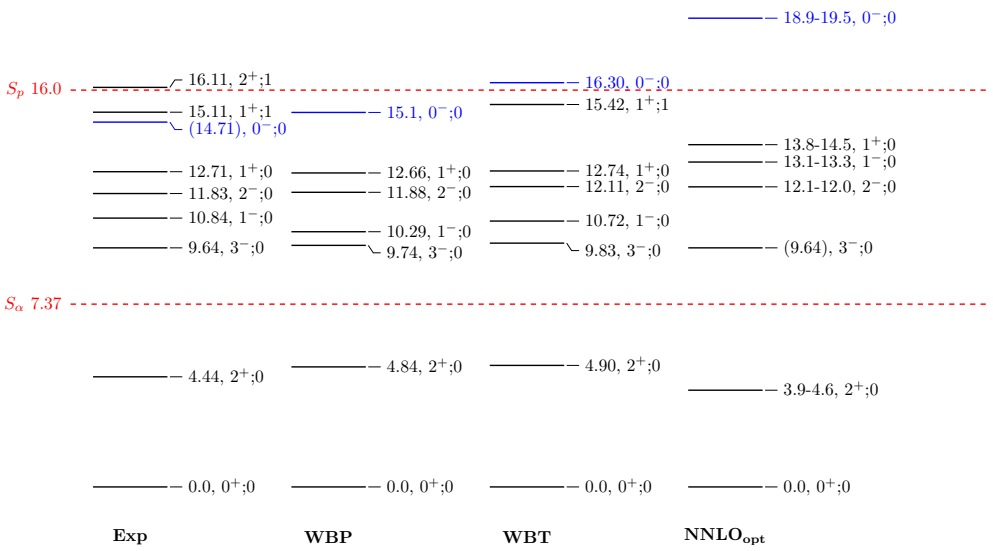

Figure 6.1: Excitation energy of low-lying states in ^{12}C, from experimental measurements, two shell-model predictions (WBP, WBT) and a no-core shell model prediction (NNLO$_{opt}$). The predicted but not previously identified 0^- state is highlighted in blue.

keV, shown in figure 6.2 This state was close to the edge of their experimental acceptance and was unassigned a spin-parity. This state was also identifed by Bohne et al. (1968) who suggested an $\ell = 0$ proton transfer, and hence a spin-parity of 1^- or 2^-, a spectroscopic factor of $0.01 - 0.02$ was calculated. No theoretical calculation matches this observation, and this state was not confirmed by Miller et al. (1969). Despite this state not being consistent with the predicted 0^-, its nature as the only contentious state in this region has led this state to be of interest, as such it is highlighted in figure 6.1.

Based on the predictions and surprising lack of experimental observation, a new ^{11}B(^{3}He,d)^{12}C reaction was performed at iThemba LABS, in order to try to identify this predicted 0^- state. The experiment studied the energy region around 14-16 MeV, where the shell model places the state, and above the proton threshold where the no-core shell model places the state. The high resolution K600 spectrometer, located at 0°, was used to identify the excited states in ^{12}C, and coincident detectors were utilised to observe the populated states' decay modes. Below the proton threshold a 0^- state can only decay via γ-decay, whereas above the threshold proton decay will become the preferred decay mechanism. As such both γ-ray and charged particle detectors were employed. An additional second state experiment was performed without the coincident detectors, but with the K600 spectrometer located at non-zero angles, in order to measure the angular distributions of the populated states, to further confirm the 0^- state's assignment, if identified.

In the region where the shell model places the 0^- state, γ-ray identification

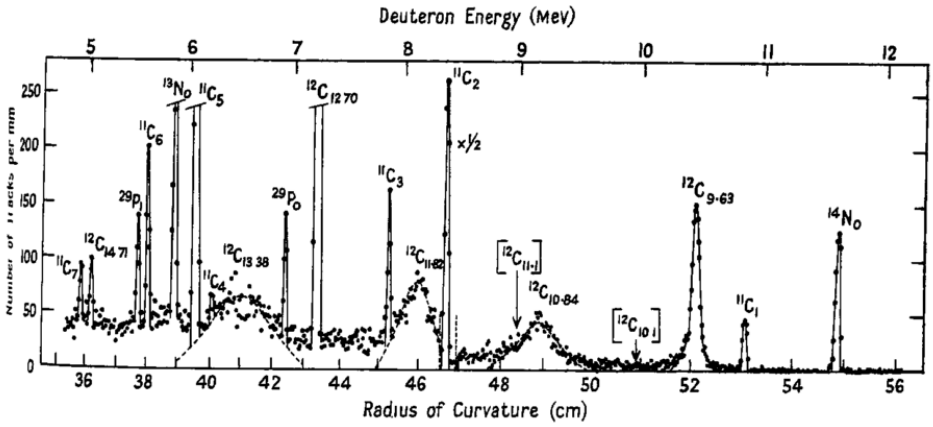

Figure 6.2: Deuteron energy spectrum from the ^{11}B(^{3}He,d)^{12}C reaction, by Hinds & Middleton (1961). A state at 14.71 MeV (Deuteron energy 5 MeV) is shown at the far left, and has not been assigned a definite spin-parity.

Table 6.1: γ-decay branching ratios for the 0^- state predicted by the shell-model using the WBP interaction.

E_f (MeV)	J^π	B_γ
4.86	2^+	88.6%
10.29	1^-	5.2%
11.88	2^-	2.4%
13.61	2^-	3.8%

will be the primary method to identify the 0^- state. Due to angular momentum conservation the 0^- state cannot decay directly to the ground state (0^+), WBP predictions of the branching ratios for the 0^- decay are shown in table 6.1, where the dominant decay is to the 4.44 MeV 2^+ state (placed at 4.86 MeV in the shell-model calculation), which itself will subsequently decay to the ground state by emission of a 4.44 MeV γ-ray. Observation of this γ-ray will therefore provide a strong indication of the 0^- state. In addition, a strong narrow 1^+ state as 15.1 MeV is well-known and near the predicted 0^- state, meaning discrimination of the two states is necessary. The 15.1 MeV state decays predominately directly to the ground state, with a branching ratio of 92(2)% , and 2(1)% to the 4.44 MeV state (Alburger & Wilkinson, 1972). Therefore, γ-ray observations will clearly separate the two states.

Table 6.2: Predicted Excitation Energies of 0^- states with the WBP Interaction by Warburton & Brown (1992).

Nucleus	J^π	E_x Experimental (MeV)	E_x Theory (MeV)	Δ
^{14}N	0^-	4.915	4.522	0.393
^{14}N	0^-	9.216	9.337	−0.121
^{16}O	0^-	10.957	10.820	0.137
^{16}O	0^-	13.016	13.080	−0.064
^{18}F	0^-	1.081	1.293	−0.212

6.2 Shell-Model and No-Core Shell-Model

The shell-model interactions (Warburton & Brown, 1992) used to predict the 0^- are constructed in the cross-shell model space connecting the $0p$ and $1s0d$ shells. These effective interactions are obtained by fitting experimental binding energies to single-particle energies and either two-body matrix elements or potential parameters. The interaction for the $1s0d$ shell is determined by the W interaction (Brown & Wildenthal, 1988), assuming no cross-shell components, whereas the p-shell component is obtained from fitting to the two-body matrix elements (PWBP) or the 45-variable model-independent fit (PWBT) to simulate p-shell and cross-shell data. These combined interactions are hence named WBP and WBT respectively. The calculations were performed with the shell-model code OXBASH. These calculations have been shown to reproduce experimental states within approximately 500 keV in many cases, and successfully reproduced many 0^- states, as shown in table 6.2. In particular the two lowest energy 0^- states of ^{16}O were offset from experimental measurements by 0.137 and 0.064 MeV.

The interaction employed for the no-core shell model (NCSM) is an optimised chiral nucleon-nucleon interaction at Next-to-Next-to-Leading Order ($\mathrm{NNLO_{opt}}$) by Ekström et al. (2013). This new chiral force yields $\chi^2 \approx 1$ per degree of freedom for laboratory energies below 125 MeV. While NNLO interactions introduce three-nucleon forces (3NFs), the contribution of Ekström et al. (2013) was on improving the precision of the nucleon-nucleon force by utilising modern least-squares optimisation. The 3NF was adjusted to the binding energies in $A = 3, 4$ nuclei after the optimisation procedure. The ^{12}C nucleus was studied using this interaction using the ab initio no-core shell model formalism formulated by Barrett et al. (2013). The model space used 6 harmonic oscillators for positive parity states and 7 for negative states, no 3NF are included. Due to limitations of the NCSM the positive and negative parity energies do not converge, and thus the energies are relative to the lowest state of the appropriate parity. A summary of the states produced is shown in table 6.3. The 1^- and 2^- states are in the wrong order compared

Table 6.3: Predicted Excitation Energies of ^{12}C states via the no-core shell model using the optimised next-to-next-to-leading order interaction (Ekström et al., 2013).

J^π	E_x Theory (MeV)	E_x Experimental (MeV)
0^+	0	0
2^+	4.54	4.44
1^+	14.46	12.71
3^{-1}	0	0
2^{-1}	2.62	2.2
1^{-1}	3.66	1.2
0^{-1}	9.45	—

[1] E_x Relative to the 3^- state, experimentally at $E_x = 9.641$ MeV

to experiment, which may vary with model space (Forssén, 2017), the lack of 3NFs is known to cause the 1^+ state to be placed too high in excitation energy, as observed in these predictions (Forssén, 2017). The 0^- state was found at a higher energy level than the shell-model, although still close by and in a region lacking any experimental 0^- observations.

6.3 DWBA

An estimation of the differential cross-section, and more importantly, the angular distribution of the differential cross-section, was calculated using the distorted-wave Born approximation (DWBA) as discussed in chapter 2. DWBA is suited to describing direct reactions such as the ^{11}B(^{3}He,d)^{12}C reaction, and performs well at forward angles such as employed with the K600 spectrometer. The program TWOFNR (Tostevin, 2017) was employed to perform the DWBA calculation, utilising the companion program FRONT to automatically choose appropriate potentials for the (^{3}He,d) transfer reaction employed. The potential used for the incoming ^{3}He channel was by Pang et al. (2009) and the potential for the outgoing deuteron channel was by Daehnick et al. (1980). For the predicted 0^- state the proton transferred from the ^{3}He nucleus to the ^{11}B nucleus was assigned $\ell = 2$ with total spin $J = 3/2$ and with 0 nodes (corresponding to the predicted $0d_{3/2}$ proton coupling) at an excitation energy of $E_x = 15$ MeV. Additionally, in order to compare distributions other states were analysed: the $\ell = 1$ transfer to the 1^+ 15.1 MeV state, which may lie close to the 0^- state of interest, and to the 12.7 MeV and 16.1 MeV states for verifying the calculations. The distributions were evaluated for the $\ell = 0$ transfer to the broad 1^- state at

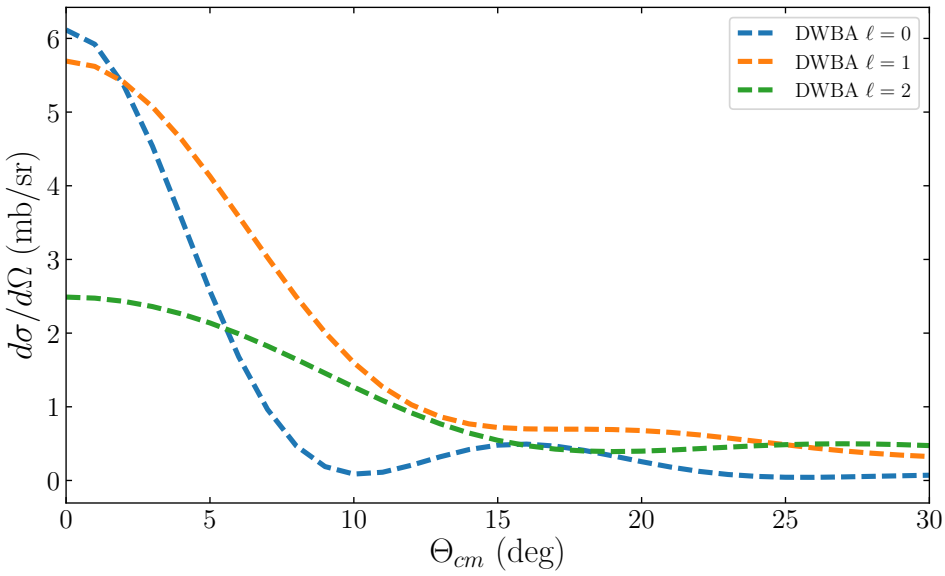

Figure 6.3: Predicted angular distributions for $\ell = 0, 1, 2$ transfer of a proton via the ^{11}B(^{3}He,d)^{12}C reaction, predicted via the distorted-wave Born approximation (DWBA).

10.8 MeV, although as a broad state the predictions of DWBA may not be as robust as for the narrow states. The predicted distributions for $\ell = 0, 1, 2$ transfers are shown in figure 6.3.

6.4 R-matrix

Although the R-matrix theory discussed in chapter 2 is not applicable to direct reactions such as ^{11}B(^{3}He,d)^{12}C, the population of ^{12}C via this mechanism and the subsequent decays can be explained using R-matrix theory, in this case the reaction treated is of the form ^{11}B($p_T q$,ν), where ν is the decay particle emitted from the excited state in ^{12}C (α-particle or proton), and p_T represents the proton transfer performed via the ^{11}B(^{3}He,d)^{12}C reaction. This proton transfer cannot be treated the same as the outgoing proton decay, or incoming resonant proton reactions that may otherwise be used with R-matrix theory.

The mechanism for the proton transfer component is not known exactly, but can be described by unknown matrix elements, which are subsequently fit to:

$$\sigma(E) \propto \sum_x \left| \sum_{\lambda\mu} g_{\lambda x} \gamma_{\lambda c} A_{\lambda\mu} \right|^2 , \tag{6.1}$$

where $g_{\lambda x}$ refers to the proton transfer matrix element via channel x, popu-

lating level λ, taking place of the reduced width amplitude for the incoming channel, $\lambda_{\lambda c}$ the reduced width amplitude of the outgoing channel c, and A the A-matrix:

$$(A^{-1})_{\lambda\mu} = (E_\lambda - E)\delta_{\lambda\mu} - \sum_c \gamma_{\lambda c}\gamma_{\mu c}(S_c - B_c + iP_c) \tag{6.2}$$

summed over all decay channels c. This formalism is analogous to that of beta-decay R-matrix (Barker & Warburton, 1988), which uses an equally unknown beta decay matrix element. In beta-decay x can only refer to Fermi or Gamow-Teller beta decay transitions, whereas for proton transfer the selection rules are the standard angular momentum rules for particle coupling. States populated via the proton transfer mechanism can therefore be studied by adapting R-matrix fitting programs written for beta-decay R-matrix, such as AZURE2.

6.5 AZURE2

AZURE2 (Azuma et al., 2010) is a multilevel, multichannel R-matrix code primarily designed for applications in nuclear astrophysics. The program's focus is to obtain level energies and partial widths by fitting to experimental data. The program is divided into two primary subroutines, connected by the fitting package MINUIT (James & Winkler, 2004). The first routine calculates necessary quantities that are not dependent on the R-matrix parameters, the second subroutine calculates the cross-section from R-matrix parameters, and determines the χ^2 value between the calculated and experimental cross-sections. This second subroutine is then called iteratively by MINUIT, varying the R-matrix parameters in order to minimise χ^2. A powerful feature of AZURE2 is its graphical user interface (GUI) which allows easy management of reaction channels and individual resonances.

As a multichannel R-matrix program, as many channels as permitted by conservation of angular momentum may be included in the analysis, and are simultaneously fitted. Interferences are automatically taken into account, providing additional constraints on the fitted parameters and allowing analysis of regions with overlapping states. AZURE2 also provides additional routines to correct for target thickness, beam energy resolution and inverse kinematics. It supports more advanced R-matrix applications including bound states, photon channels, and β-delayed particle emission. The β-delayed particle emission routines were modified in order to support the proton transfer reaction being studied, removing the dependence on β-decay phase space, accounting for penetrability of the charged proton, and replacing the β-decay selection rules with angular momentum conservation rules. A detailed description of the modifications made are included in appendix A.

Chapter 7

The K600 Facility at iThemba LABS

In order to identify the 0^- state, ^{12}C was populated via the proton transfer reaction ^{11}B(^{3}He,d)^{12}C at iThemba LABS. This mechanism was predicted from shell-model calculations to have a high cross-section for the production of the 0^- state. The ^{3}He beam was accelerated by the SSC cylcotron to an energy of 85 MeV and reacted with targets of enriched ^{11}B of thicknesses 150 μg/cm^2 and 500 μg/cm^2. These targets were produced with a backing of 180 μg/cm^2 of polyethylene naphthalate (PEN) plastic (carbon and oxygen). For background subtraction, data was also taken on a target of 180 μg/cm^2 plastic. The deuterons ejected were detected in the K600 high resolution magnetic spectrometer, whose aperture was positioned at horizontal angles of 0, 8, 12, 16 and 20 degrees relative to the beam. The spectrometer has a resolution of approximately 40 keV. In the measurement at 0° the target was additionally surrounded by the CAKE and SIMNEL coincidence detectors in order to measure protons, α-particles and γ-rays emitted from the decay of the excited ^{12}C states. Two weekends of measurements were allocated: one was performed entirely at 0 degrees with the coincidence detectors and the K600, the other was taken at non-zero angles with the K600 spectrometer only.

7.1 iThemba LABS

The iThemba LABS accelerator complex is shown in figure 7.1. The high energy beams for the ^{11}B(^{3}He,d)^{12}C reaction are produced by the iThemba LABS Separated Sector Cyclotron (SSC), capable of accelerating light ions up to 240 MeV. The initial beam is ionised by the MINIMAFIOS ECR ion source and injected into the solid pole injector cyclotron (SPC2) which accelerates the beam to the energy required for the SSC. This beam is then injected into the SSC itself where it is accelerated to the final desired energy. The final beam is then delivered to the K600 spectrometer via a high resolution double

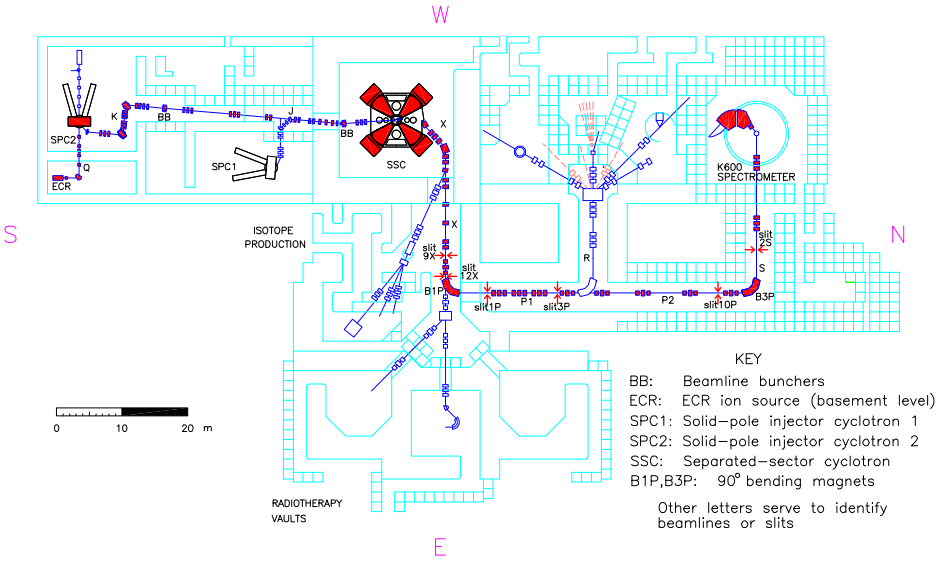

Figure 7.1: Schematic of the accelerator complex at iThemba LABS, highlighting the accelerators which produce the beams required for the K600 spectrometer, as described in the text. By Neveling et al. (2011).

monochromator system of beam lines. The horizontal and vertical slits after the SSC, named 9X, form the object slit for the spectrometer, and the slits 12X form the emittance slits, both must be finely tuned to obtain dispersion-matching (Neveling et al., 2011).

7.2 The K600 Spectrometer

The K600[1] Magnetic Spectrometer is a high-resolution QDD (quadrupole, dipole, dipole) spectrometer (Neveling et al., 2011). A magnetic spectrometer separates charged particles based on their magnetic rigidity $B\rho = \frac{pc}{q}$: Within a magnetic field, charged particles experience a Lorentz force, in which the field within the spectrometer guides the particles along a circular trajectory whose radius depends on the particle's momentum. The "focal plane" of a spectrometer is the plane at which the perpendicular position of the particle is dependent solely on the magnetic radius and not the initial trajectory, as shown in fig 7.2. Position sensitive particle detectors placed at the focal plane can thus be used to determine the momentum of an ion, and subsequently the excitation energy of the nucleus produced in the target. Conversely, detectors placed off the focal plane additionally provide some information on the initial trajectory of the particle. The K600 employs detectors both on and off the

[1] K is the energy constant, defined as $K = \frac{mE}{q^2}$ for magnetic devices

focal plane to reconstruct the trajectory of the particle, while maintaining optimal momentum resolution.

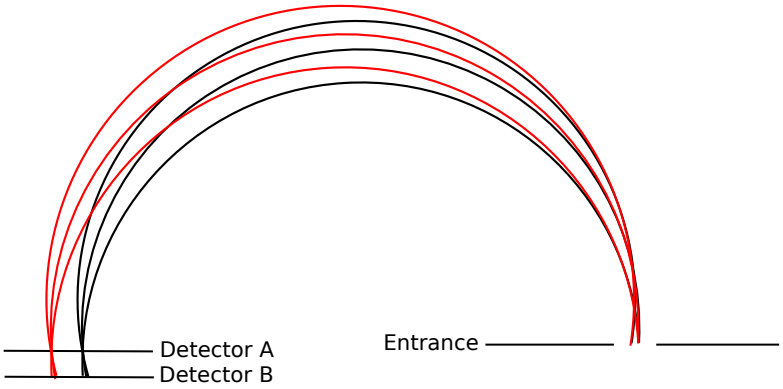

Figure 7.2: An example of focussing in a magnetic spectrometer. The black and red lines start from the same three initial trajectories, but differ in radius of curvature. At the focal plane (Detector A) all the same coloured lines converge, and the only difference in position is due to the radius of curvature (and thus is proportional to the particle's momentum). At Detector B the lines diverge again and the particle's initial trajectory can be obtained with the information from both detectors.

The magnetic elements of the K600 are shown in figure 7.3. The primary focussing elements are two dipole magnets which provide the linear magnetic field which separates the charged particles, and focuses them along the focal plane. The ratio (R) of the two dipoles determines where the focal plane lies, whereas the absolute field strength determines the excitation energies which cross the focal plane detectors. The K600 has three focal planes: the medium-dispersion focal plane ($R = 1.00$) and the high-dispersion focal plane ($R = 1.49$), and an unused low-dispersion focal plane. The high-dispersion focal plane provides greater momentum separation (and hence resolution) at the expense of a reduced energy range covered. The medium-dispersion focal plane is used in this experiment to cover an excitation energy range of about $8 - 24$ MeV.

The K600 spectrometer contains 3 additional magnetic elements for achieving focus. A quadrupole magnet at the entrance is used to focus the beam in the vertical direction, although typically this is intentionally slightly off-focus to provide information on the vertical trajectory through the spectrometer, which is important for analysing angular dependent properties. An entrance hexapole is also installed, but is unused. Two trim coils, termed H and K, are utilised to correct higher order kinematic aberrations. H is a dipole+quadrupole to correct for $(x|\theta)$ and K is a dipole+hexapole to correct for $(x|\theta^2)$ (This notation is described in Enge (1981)). These kinematic

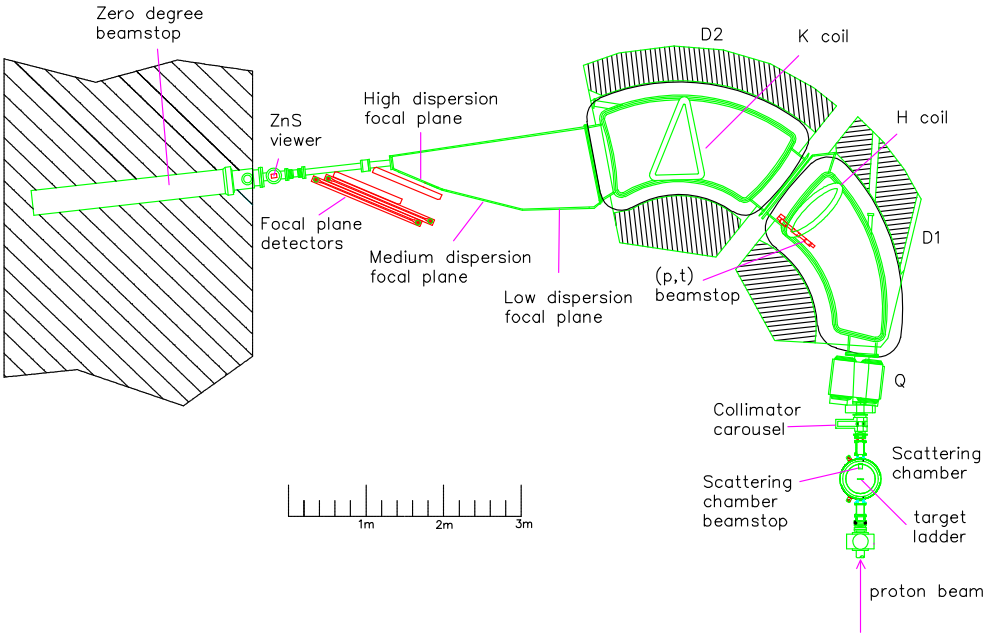

Figure 7.3: Schematic of the K600 Spectrometer at iThemba LABS. Momentum analysis is performed by the two dipole magnets, with the quadrupole used to achieve vertical focus. The H and K coil are used to correct for higher order kinematic aberrations. Figure by Neveling et al. (2016).

aberrations are isotope dependent, and must be optimised for the isotope of interest. Analysis of the x dependence on θ can be used to distinguish between different isotopes, particularly at non-zero angles.

As previously discussed, the excitation energy of the ^{12}C nuclei can be extracted from the measured momentum of the deuteron. In practice however this analysis is limited by the spread of energies in the incoming ^{3}He beam from the cyclotron accelerator, which can be many 100s of keV – much higher than desirable for the spectrometer resolution. The energy resolution can be improved by a technique known as dispersion-matching, which disperses the beam on the target so that deuterons produced from beam particles with lower momentum travel less distance through the spectrometer to compensate for the increased bending they experience. This *lateral* dispersion-matching results in a momentum dependence on the ejectile's angle through the focal plane, which can be removed by employing *angular* dispersion matching, allowing accurate reconstruction of the scattering angle of the deuteron. With this technique the spectrometer energy resolution can be as low as 10 keV FWHM, with typical resolutions of $30 - 40$ keV FWHM.

With the K600 this dispersion matching condition is achieved via the faint-beam technique, which involves inserting meshes into the beam-line to reduce

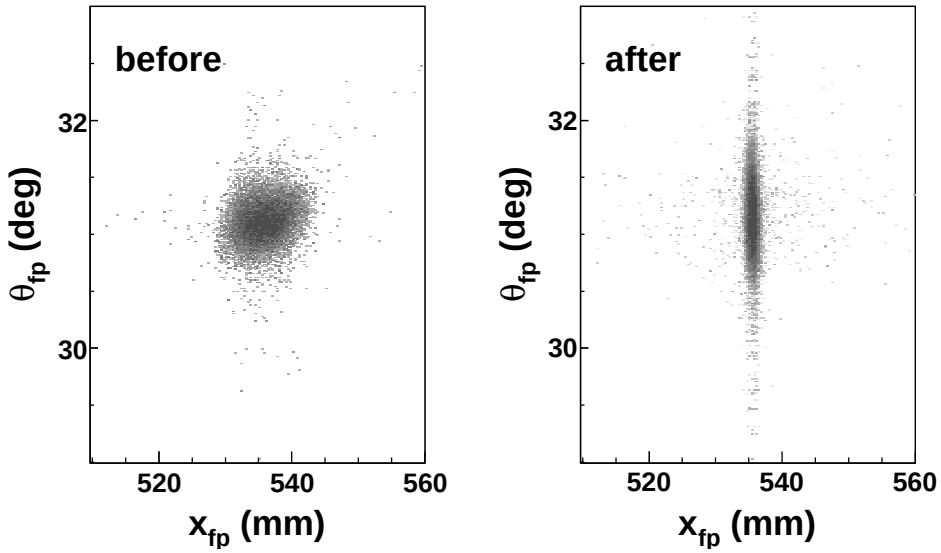

Figure 7.4: The faint beam image before and after dispersion matching for 200 MeV protons (Neveling et al., 2011).

the intensity of the beam by many orders of magnitude. This faint beam can then be steered directly on to the focal plane of the spectrometer. As the full intensity beam would destroy the detectors, an interlock system is in place to prevent the beam from being steered onto the detectors without the faint-beam meshes being inserted. Once the beam is on the focal plane, the focus can be adjusted by optimising beam-line elements, primarily quadrupoles, and the H and K trim coils, in order to optimise the resolution in (x_{fp}, θ_{fp}). The effect of dispersion matching on resolution is shown in figure 7.4.

7.3 Focal Plane Detectors

Position measurements at the focal plane are measured by one or two multi-wire drift chambers, referred to as vertical drift chambers (VDCs), which contain a set of 198 vertical signal wires for measurement of horizontal position (X wires). In addition, newer VDCs contain a set of 143 wires at 50° to the horizontal plane (U wires), which can be used to measure the vertical position at the focal plane. In this experiment the setup involves one new (XU) VDC at the focal plane, and one old (X) VDC behind it. The VDCs consist of two high-voltage cathode planes with a signal wire anode plane midway between them (XU VDCs have two signal wire planes and share the cathode plane between them, leading to three cathode planes). The detector is filled with a gas mixture of 90% Ar and 10% CO_2 and the cathodes are held at a negative high voltage of approximately −3500 V. The signal wires are held at 0 V potential, and interspersed with guard wires, held at approximately −500

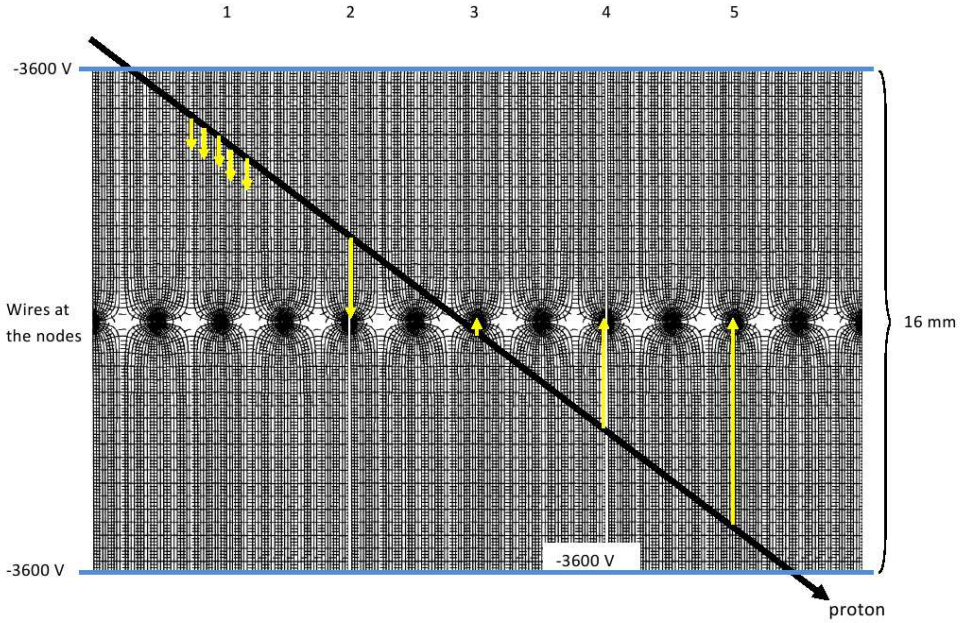

Figure 7.5: Schematic of the field lines and the ionisation produced by a charged particle passing through a VDC. The drift lengths (yellow arrows) can be used to reconstruct the proton's trajectory. Figure by Neveling et al. (2016).

V, which shape the electric field and provide cells around each field wire of about 4 mm. Charged particles interact with the gas mixture to produce ionisation electrons which drift along the shaped field lines to the signal wires. These signal wires are connected to CAEN V1190A TDCs (time to digital converters), which measure the relative time between the trigger and the signal wire firing, with a precision of 100 ps. These drift times are converted into drift lengths: the distance from the signal wire where the ionisation occurred, via a look-up table produced from a structureless 'white-spectrum' region of the focal plane: where drift lengths are uniformly distributed. Because a particle will ionise multiple signal wires, the path through the detector can be reconstructed via *ray-tracing* the measured drift lengths. This provides much greater resolution than the 4 mm cell size. The field lines and an example event are shown in figure 7.5.

Behind the VDCs are two plastic scintillator detectors, named paddles due to their geometry. These detectors are used to provide the trigger signal to the data acquisition system, as well as to measure $\Delta E - \Delta E$ energy loss to aid in particle identification. In this experiment the thickness of these

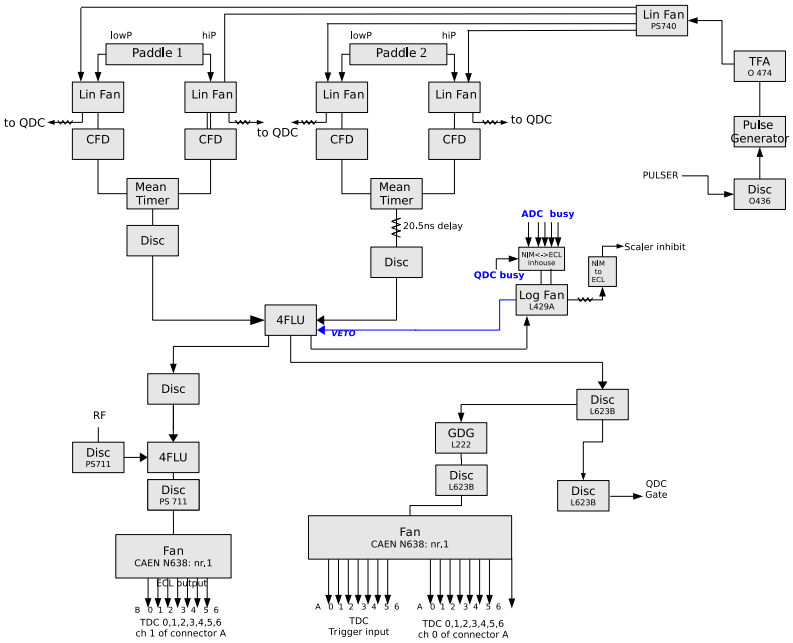

Figure 7.6: Schematic of the K600 trigger electronics. Figure by Neveling et al. (2016).

scintillator detectors is 1/4" (6.35 mm) for the first detector, and 1/2" (12.70 mm) for the second detector. The light from these scintillators is collected and amplified by a built-in PMT (photomultiplier tube) and the subsequent charge is recorded by a Caen V792 QDC (charge to digital converter) with a full-scale range of 400 pC. The signal produced by the scintillators is also connected to a constant-fraction discriminator in order to produce the trigger signal. The Caen V1109A TDCs store the time of events (from the focal plane) in a rolling buffer, which is read out when the trigger signal is received, acting as a common stop. The TDC runs on a 25 MHz clock, and as such these times are susceptible to a jitter of up to 40 ns, depending on when in this window the trigger signal arrived. To compensate for this the trigger is additionally copied into channel 0 of each TDC module, and the difference from channel 0 provides a constant time reference between modules, although further alignment is necessary to correct for differences in cable lengths and electronics processing. The time of flight of particles can be obtained by taking the difference between the trigger signal and the cyclotron RF signal (which is recorded in channel 1 of each TDC module). The electronics for the scintillator trigger system are shown in figure 7.6

Particle identification is performed by comparing the time of flight against the energy loss in the first scintillator, with the energy loss in both scintillators providing additional identification if necessary. Particle identification can be made cleaner by increasing the time separation between two events.

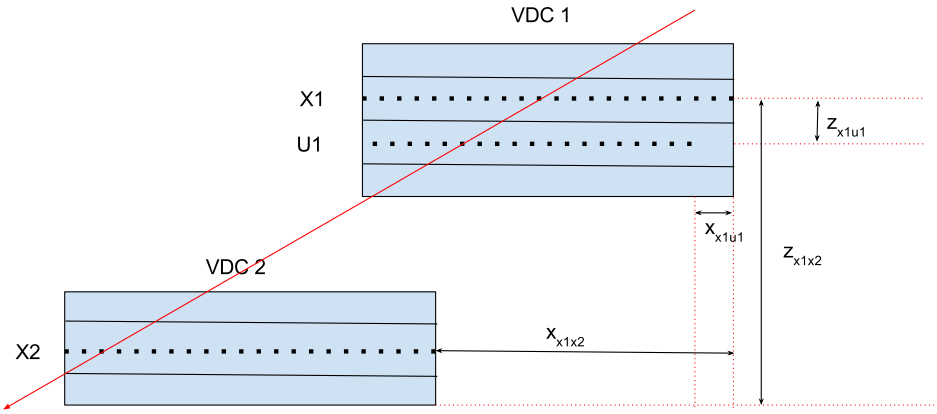

Figure 7.7: Schematic of the relative positioning of the two VDCs and their wire-planes, showing the necessary parameters for the calculation of θ_{fp} and y_{fp}. An example particle trajectory is in red. The definitions of the terms are described in the text.

For this purpose a pulse selector is installed in the accelerator RF system, which deflects some proportion of the RF pulses before the cyclotron. This increased separation also improves coincidence measurements by improving the correlations between focal-plane and silicon events.

Information on the horizontal and vertical components of the trajectory through the spectrometer is obtained from measurements from the two X wire-planes and the U wire-plane. (The horizontal angle could in theory be obtained directly from ray-tracing from the first X wire-plane only, however using the two wire-planes provides much greater sensitivity due to the larger distances used to determine the angle). The positions along the wire-planes (X_1, X_2, U_1) are converted into more intuitive coordinates of the particle at the focal plane $(x_{fp}, \theta_{fp}, y_{fp})$ via simple trigonometry of the focal plane system, shown graphically in figure 7.7:

$$x_{fp} \equiv X_1 \tag{7.1}$$

$$\theta_{fp} = \tan^{-1}\left(\frac{z_{x1x2}}{(X_2 + x_{x1x2}) - X_1}\right) \tag{7.2}$$

$$y_{fp} = -\left(\frac{U_1 \tan\theta_{fp} - z_{x1u1}\sin\theta_U}{\sin\theta_U \tan\theta_{fp}} \tan\theta_U + x_{x1u1}\right) . \tag{7.3}$$

Here X_1, U_1, X_2 refer to the detected position along the appropriate wire-plane. z_{x1x2} is the separation of the two focal planes in the direction of the beam, and x_{x1x2} is the offset of the second focal plane from the first focal plane in the direction of momentum separation, these are measured during the experimental setup procedure. θ_U is the angle of the U wires to the horizontal (50°), x_{x1u1} is the offset of the first U wire from the first X wire (29.21 mm) and z_{x1u1} is the offset of the U wire plane from the X wire plane

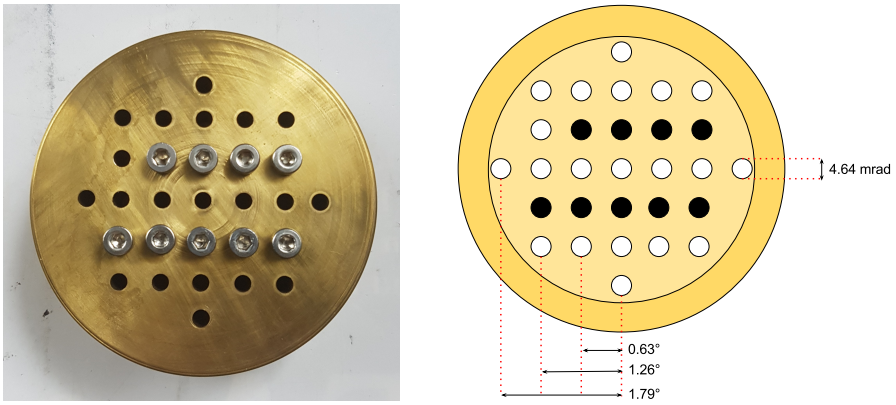

Figure 7.8: Photo (left) and schematic (right) of the pepperpot collimator used to calibrate focal plane angles. The angular distance from 0° for the horizontal holes is noted, which are the same for the vertical holes.

in the direction of the beam (16.0 mm), these are fixed from the construction of the VDCs.

These coordinates can then be related to horizontal (θ_{scat}) and vertical (ϕ_{scat}) scattering angles between the aperture of the focal plane and the target. These conversions are obtained by fitting data using a special calibration pepperpot collimator with multiple holes at known angular positions, figure 7.8, using the following fit relations (Neveling et al., 2011):

$$\theta_{scat} = \theta_{fp} \sum_{i=0}^{2} a_i x_{fp}^i + \sum_{i=0}^{2} b_i x_{fp}^i \tag{7.4}$$

$$\phi_{scat} = y_{fp} \sum_{i=0}^{3} \sum_{j=0}^{2} c_{ij} x_{fp}^j \theta_{fp}^i + \sum_{i=0}^{3} \sum_{j=0}^{2} d_{ij} x_{fp}^j \theta_{fp}^i \,, \tag{7.5}$$

with $x_{fp}, \theta_{fp}, y_{fp}$ as defined above in equations (7.1–7.3). These values range from -2 to +2 degrees, which is the angular size of the aperture. These scattering angles themselves can then be used to determine Θ, the azimuthal angle at which the ejected deuteron was emitted:

$$\Theta = \sqrt{(\theta_{scat} + \theta_{K600})^2 + \phi_{scat}^2} \,, \tag{7.6}$$

which can be used for the determination of angular distributions with a finer granularity than the 4° aperture size: typically 1° divisions can be used. θ_{K600} is the horizontal angle of the spectrometer aperture with respect to the beam direction.

7.4 Zero Degrees

For scattering and reactions with low angular momentum transfer, the differential cross-section is largest at small angles, peaking at 0°, and so the spectrometer at 0° would yield maximum statistics. In addition, the high selectivity towards low angular momentum transfer can simplify the analysis of spectra (Neveling et al., 2011). High resolution spectroscopy at 0° is experimentally challenging, however, due to the importance of separating the beam from the reaction particles within the spectrometer. This challenge becomes greater with inelastic scattering due to the small differences in rigidity between the beam and the scattered particles – making the measurements very sensitive to beam halo and background components.

Due to these requirements, beam delivery is subject to stringent requirements: the beam should have small energy spread, a small emittance and little halo, and equally these conditions must remain stable over time (Neveling et al., 2011). With (^{3}He,d) reactions as performed in this experiment, beam delivery is not as strict as with inelastic scattering, due to the greater ease of distinguishing between scattered ^{3}He and deuterons via the energy loss in the scintillator compared to the time of flight and because the unreacted beam has a lower rigidity than the deuterons of interest, so it is bent more easily by the magnetic field and into a beam stop internal to the first dipole of the K600. Nonetheless, it is important to minimise beam halo to ensure the trigger rate of the data acquisition system is not too high, and to ensure the separation of the beam halo remains clean. Periodically throughout the experiment beam halo is checked by using an empty target and observing the trigger rate of the system, and the beam was adjusted if the trigger rate was above 50 Hz.

7.5 The CAKE Silicon Array

Using the K600 spectrometer in a stand-alone mode, we are able to study the structure and property of, and identify the population of excited states. With the addition of coincidence detectors the decays of these excited states can be measured, providing additional information on the structure of the states: These include additional information on spin-parity assignments, and measurement of branching ratios and partial widths. As 0^- states cannot decay via α-decay due to parity conservation, states observed to α-decay can be excluded as candidate 0^- states. In addition, if the 0^- state does lie above the proton threshold, it is predicted to primarily decay via proton decay.

The Coincidence Array for K600 Experiments (CAKE) is a silicon array for the detection of charged particles (Adsley et al., 2017). It is comprised of five double-sided silicon strip detectors (DSSDs) of the MMM design from Micron Semiconductor Ltd. (fig 7.9). The detectors are 400-μm thick and

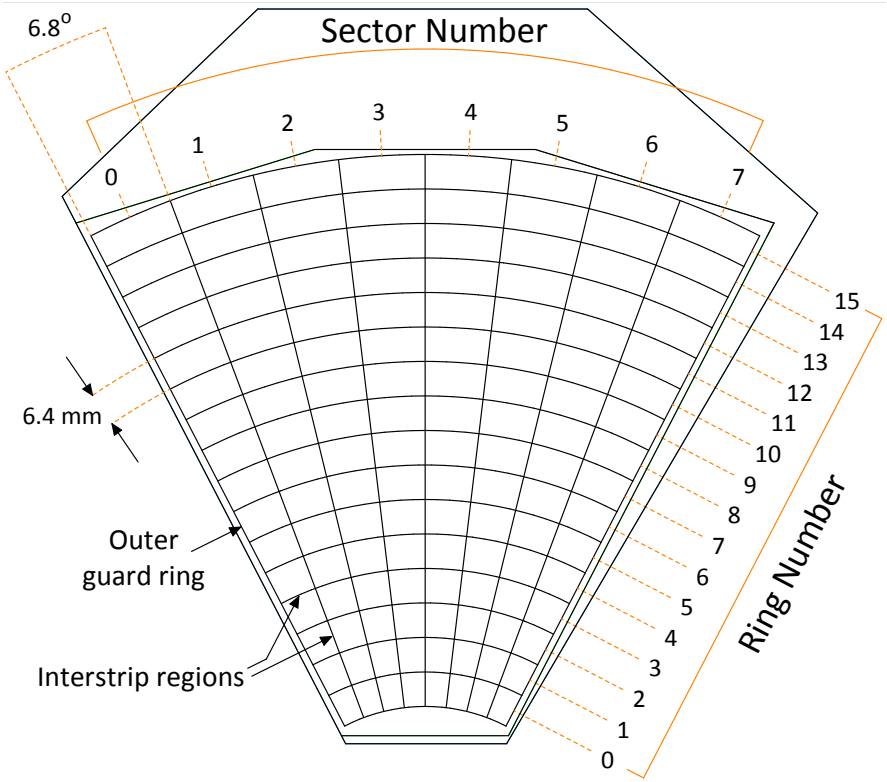

Figure 7.9: Schematic of an MMM type DSSD detector, highlighting the dimensions of the individual segments. Figure by Li (2015).

contain 16 ring channels on the junction side and 8 sector channels on the ohmic side.

MMM design detectors are wedge-shaped detectors with an azimuthal angle of 54°, a length of 102.5 mm and an active area of 54000 mm^2 (Micron Semiconductor Ltd, 2018). Each detector covers approximately 5% solid angle. The 5 MMM detectors can be packed together to form a lampshade configuration, making the total efficiency 25%, which is located at backward angles, covering an angular range of $115° - 165°$. The use of additional detectors at forwards angles to yield an efficiency of 50% is not possible due to the rate of scattered beam being too high. A figure of the CAKE array and its location within the scattering chamber is shown in fig 7.10. CAKE does not significantly impact background in the 0°-mode due to its aperture being larger than the target frame and being upstream of the target, reducing the likelihood of elastically scattered particles entering the spectrometer (Adsley et al., 2017).

The CAKE detectors are connected to Mesytec MPR-16 and MPR-32 preamplifiers via vacuum feedthroughs, which provide the initial charge collection and signal amplification. These signals are then fed to Mesytec MSCF-16

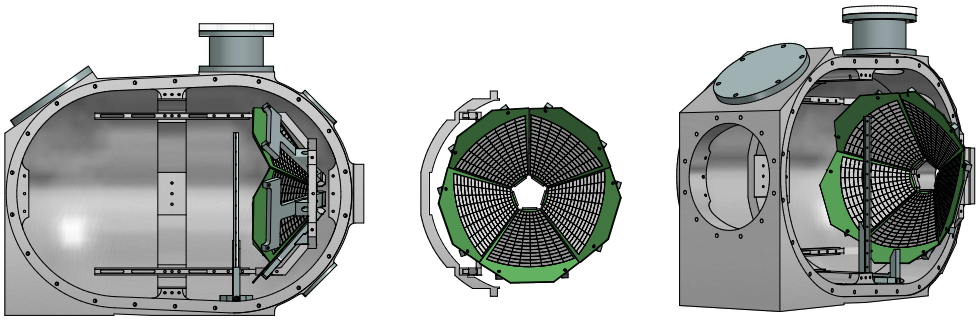

Figure 7.10: Rendering of the CAKE array (centre) and its location within the target scattering chamber. The beam enters the right of the left-most figure, and leaves the left. Figure by Li (2015).

shaping amplifiers which perform shaping and amplifying of the preamplifier signals to be fed to the ADCs, and provide timing signals via the constant fraction method to be fed to the TDCs. The charge-signal peak-heights converted by the ADCs determine the energy of the emitted charged particle, and together with excitation energy from the K600 can determine the breakup final state in ^{8}Be or ^{11}B. Timing signals are used to discriminate between α-particles and protons. The ADCs are CAEN V785 ADCs, and the TDCs are CAEN V1190A TDCs. The TDCs store the timing signals in a rolling buffer and are capable of directly measuring offsets of 800 ns before and 1200 ns after the trigger (from the K600). This means the CAKE timing signals do not have to be delayed. The ADCs perform digitisation in a 6 μs window after the trigger, and so the CAKE analog signals must fall in this window. A 1 μs shaping time on the amplifiers effectively achieves the necessary delay.

7.6 The SIMNEL Array

The 0^- state is predicted by the shell model to lie below the proton separation threshold in ^{12}C, and is forbidden to α decay due to parity conservation. Thus if the state is located in the predicted energy region it will not emit charged particles to be detected by CAKE. In order to measure the emitted γ-rays the SIMNEL (Sodium Iodide for Measurement of Nuclear Energy Levels) array was installed outside the scattering chamber. This array is composed of 5 individual NaI scintillator detectors in order to observe emitted γ-rays. NaI scintillator detectors have poor resolution but high efficiency, and are capable of covering a large range of gamma energies.

The NaI crystals are 3”x3” and are positioned at backward angles approximately 17 cm from the scattering chamber. The absolute efficiency for 4.44 MeV γ-rays was estimated at 0.46%. The energy resolution for the detectors is approximately 6.5%. The detectors are directly attached to photomulti-

plier tubes (PMTs) which amplify the light emitted from the scintillation and convert the light into electrical signals for further processing. The signals are then connected to shaping amplifiers as with CAKE, and the analogue energy and timing signals are fed to ADCs and TDCs respectively.

Chapter 8

Analysis of ^{12}C Below the Proton Threshold

8.1 Spectrometer Analysis at 0°

The raw data (TDC, ADC, QDC) recorded for the experiment were converted into physical parameters for analysis utilising the sort code K600ANALYSER produced at iThemba LABS using the MIDAS analysis package (Adsley et al., 2014). This program converts the TDC times from the focal plane into positions along each focal plane by utilising the ray tracing algorithm discussed in chapter 7. The time of flight and uncalibrated energy from the plastic scintillators are also recorded. Events where the number of focal plane wires which fire is between 3 and 6, and where the ray tracing algorithm successfully converges with reduced $\chi^2 < 1$ are termed good events — other events are considered invalid and are excluded from subsequent analysis.

Once the data have been sorted for analysis, the deuterons must be separated from background events, such as events caused by scattered ^{3}He. This is performed using a particle identification (PID) plot comparing particle time-of-flight through the spectrometer to the energy lost in the first scintillator paddle. Due to the large rigidity difference between the deuterons and scattered ^{3}He, the deuterons appear clearly as a well-separated region in the PID. The PID and the deuteron gate are shown in figure 8.1.

Following identification of the deuterons, the focal-plane position (x_{fp}, equation 7.1) is corrected for aberrations with the horizontal scattering angle at the aperture (θ_{SCAT}, equation 7.4). Although in principle these are corrected by the K and H trim coils in the K600 spectrometer (Neveling et al., 2016), software based corrections can improve the position resolution further. An example of an uncorrected plot of x_{fp} vs θ_{SCAT} is shown in figure 8.2, where the states are observed to bend slightly as θ_{SCAT} changes. The correction process involves finding the peak x_{fp} coordinate for various values of θ_{SCAT}, these values of (x_{fp}, θ_{SCAT}) are then fitted to a third order polynomial

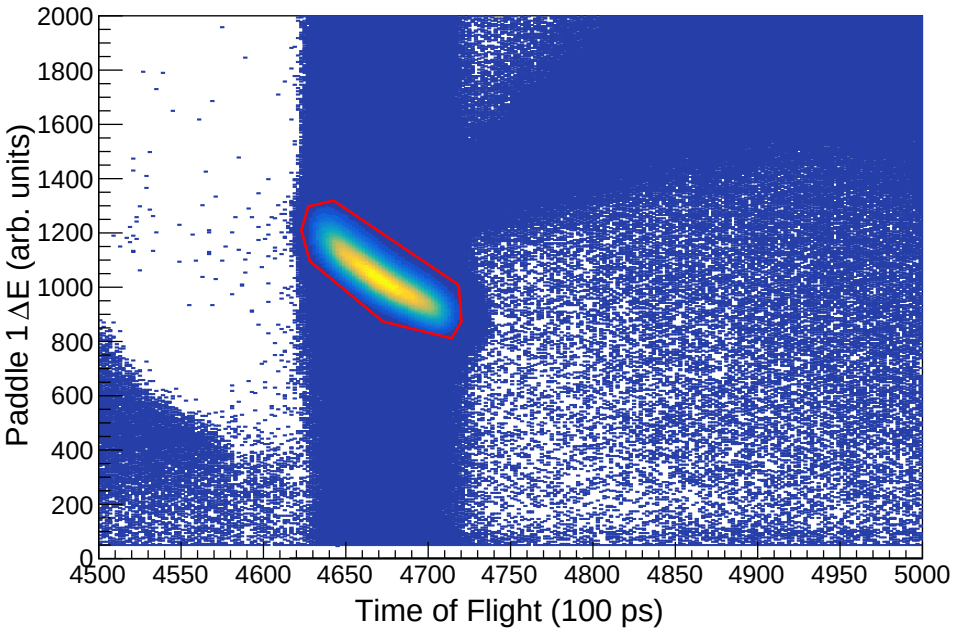

Figure 8.1: Particle Identification (energy loss in the first scintillator vs time of flight) for deuterons in the K600 spectrometer. The gate used to identify deuterons is shown in red.

with x_{fp} at $\theta_{SCAT} = 0$, $x_{fp,c}$:

$$x_{fp,c} = x_{fp} + a\theta^3_{SCAT} + b\theta^2_{SCAT} + c\theta_{SCAT} \ . \tag{8.1}$$

The corrected plot is shown in figure 8.3 where the bending is reduced, improving the resolution.

After the focal-plane position has been corrected for kinematic aberrations, the positions can be converted into excitation energies of the populated ^{12}C nucleus. Positions along the focal-plane are proportional to magnetic rigidity $B\rho$, and the relationship is obtained by fitting to calibration states of known excitation energy and rigidity. An initial linear fit is performed to three very strong states: the ground state and 2.3 MeV state of ^{13}N (populated in ^{12}C(^{3}He,d)) and the ground state of ^{17}F (populated in ^{16}O(^{3}He,d)), shown in figure 8.4. The strong peak at $x_{fp} = 210$ mm corresponds to a doublet and was not used for calibration. This initial fit is then refined by using additional weaker states in ^{14}N and ^{13}C, fitting to a quadratic polynomial. This fit result is shown in fig 8.5, where excellent linearity is observed.

The rigidities are converted into excitation energies in ^{12}C via kinematic relations, using conservation of momentum in the z-direction to determine the

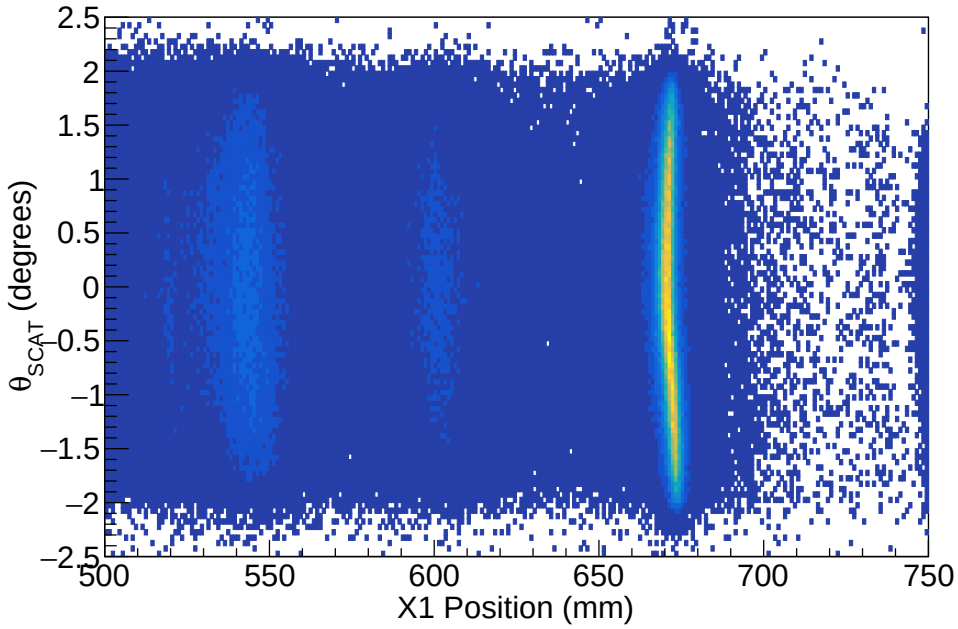

Figure 8.2: Dependency of x_{fp} position on θ_{SCAT} before aberration corrections in software.

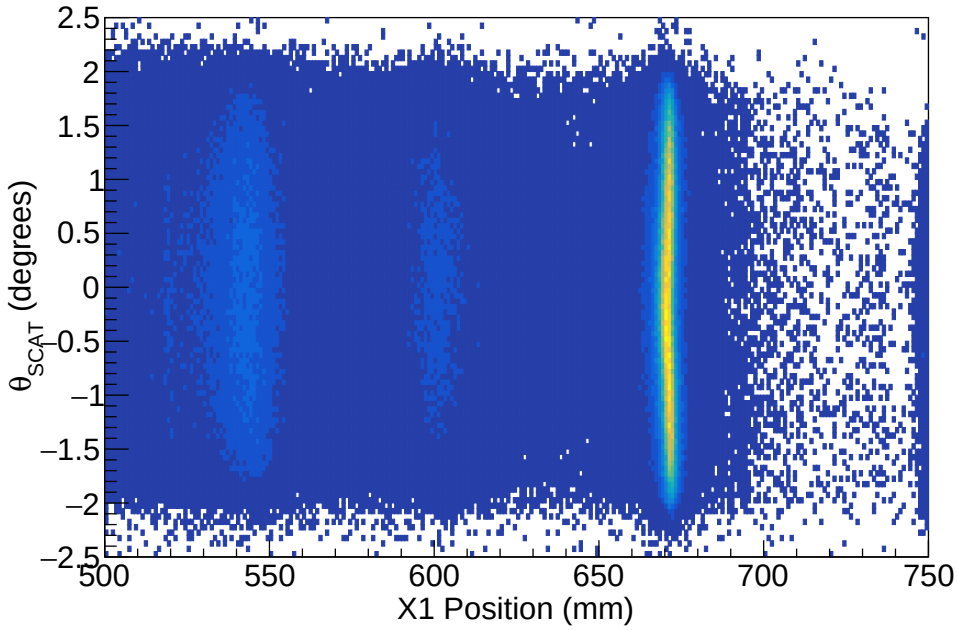

Figure 8.3: Dependency of x_{fp} position on θ_{SCAT} after aberration corrections in software.

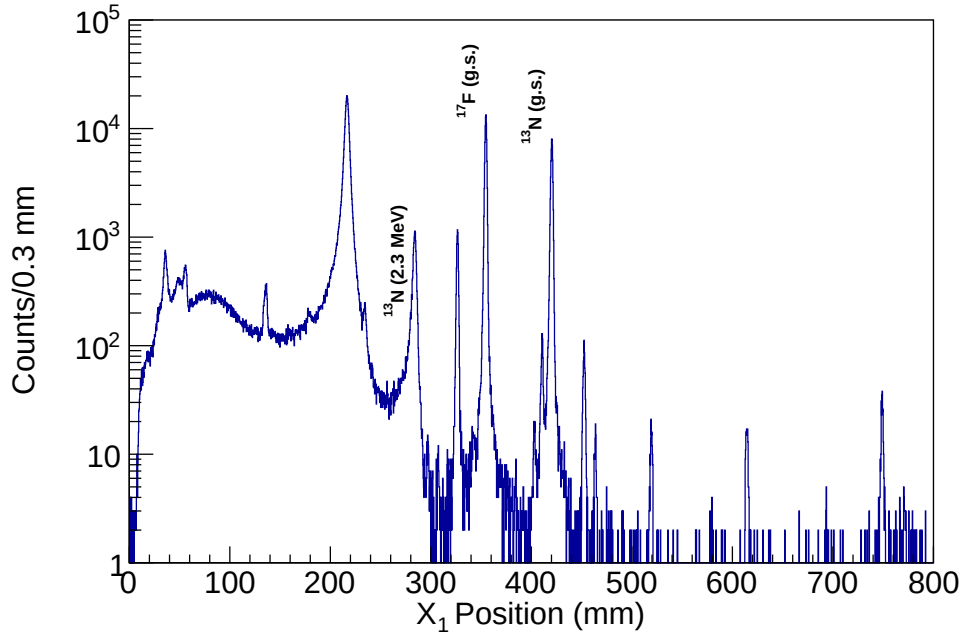

Figure 8.4: Focal-plane spectrum of the plastic target, highlighting three strong background states used for initial excitation energy calibration.

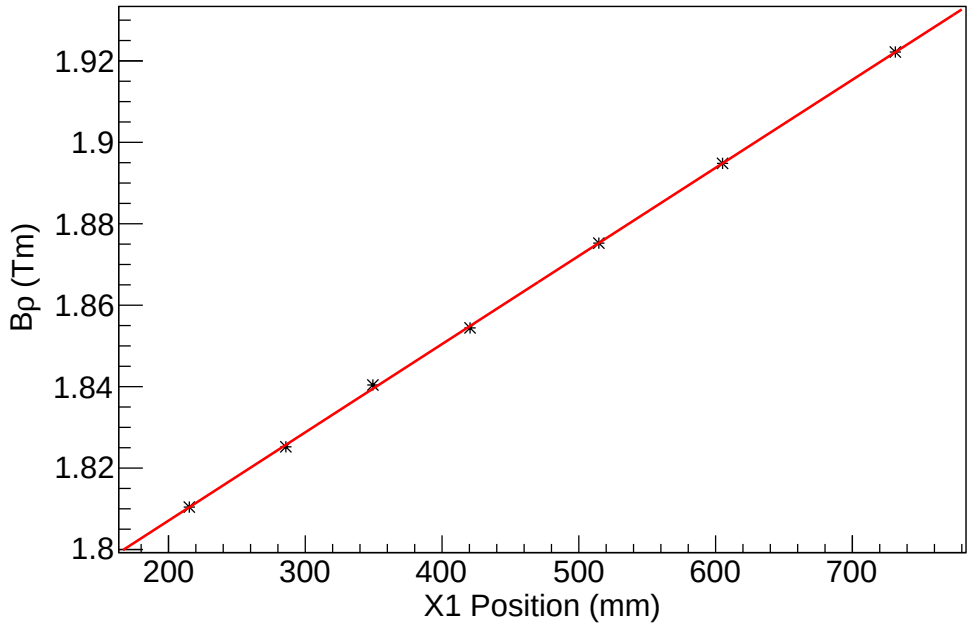

Figure 8.5: Calibration of the focal plane to magnetic rigidity $B\rho$.

momentum of the ^{12}C recoil.

$$p_{beam} = \sqrt{T_{beam}(T_{beam} + 2m_{beam})} \tag{8.2}$$

$$p_d = B\rho c \tag{8.3}$$

$$T_d = \sqrt{p_d^2 + m_d^2} - m_d \tag{8.4}$$

$$p_{12C} = p_{beam} - p_d \tag{8.5}$$

$$T_{12C} = \sqrt{p_{12C}^2 + m_{12C}^2} - m_{12C} \tag{8.6}$$

$$E_x = T_{beam} - T_d - T_{12C} + Q \ , \tag{8.7}$$

where Q represents the Q-value of the ^{11}B(^{3}He,d)^{12}C reaction producing ^{12}C in its ground state: 10.463 MeV.

The final excitation energy spectra after these corrections have been performed is shown in figure 8.6. Data taken with the plastic target is scaled to data taken with the ^{11}B target, so that the strong background peak at 17.5 MeV has the same number of counts in both spectra. Strong well-known states in ^{12}C are labelled. The 15.1 MeV 1^+ state overlaps with the ground state of ^{17}F from the oxygen present in the plastic backing, and as such this contaminant should be eliminated in coincidence spectra. The same graph, but focussing on the region above the proton separation energy is shown in figure 8.7.

8.2 Spectrometer Analysis at Non-Zero Angles

In order to obtain angular distributions, data were additionally taken with the K600 spectrometer at angles of $8, 12, 16$ and $20°$, no coincident detectors were employed. Raw data (TDC, QDC) is recorded and initially analysed as with the zero-degree data. The initial calibration stages are the same, the first step is identification of the deuterons at the focal plane using the time-of-flight and scintillator energy. Compared to zero degree this stage is simplified due to the fact the beam and the spectrometer are no longer colinear, and hence the beam is stopped before entering the spectrometer – reducing the scattered beam particles that may reach the focal plane. A sample particle ID spectrum for 8° is shown in figure 8.8, and can be compared to figure 8.1. Following this, the focal plane is calibrated as described via equations 8.2–8.7, except p_{12C} is redefined to account for the non-zero scattering angle:

$$\theta_{12C} = \arctan \frac{\sin(\theta_{K600})}{p_{beam}/p_d - \cos(\theta_{K600})} \tag{8.8}$$

$$p_{12C} = p_d \frac{\sin(\theta_{K600})}{\sin(\theta_{12C})} \ . \tag{8.9}$$

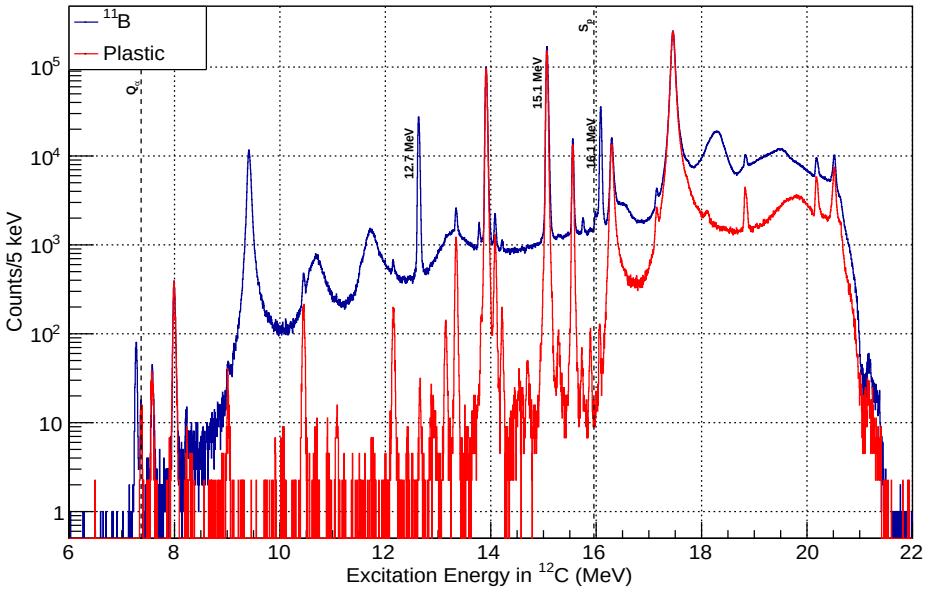

Figure 8.6: Spectra of deuterons detected in the K600 spectrometer, over the full acceptance of the spectrometer, on ^{11}B and plastic targets. Data on the plastic target is scaled to data on the ^{11}B target.

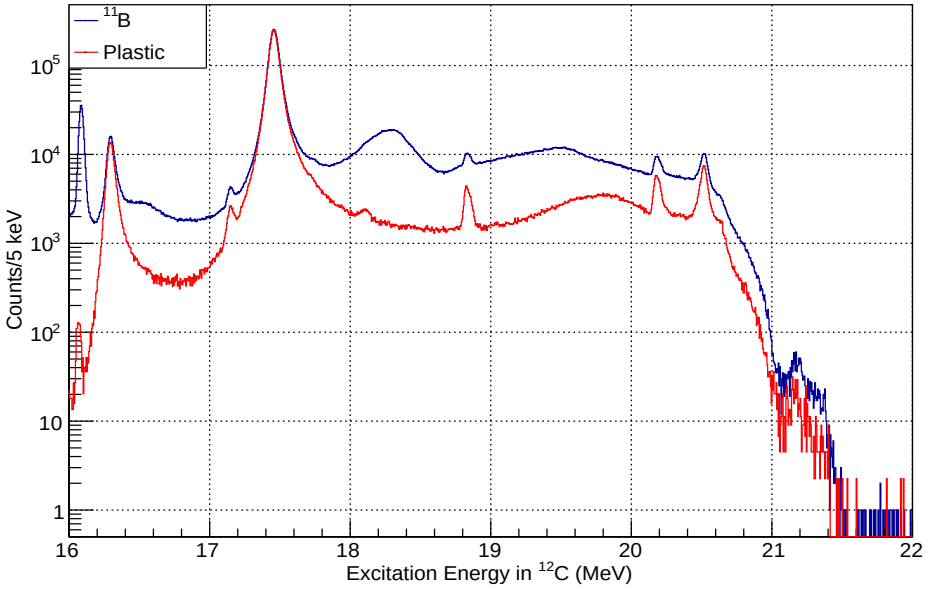

Figure 8.7: Same as figure 8.6 but focusing on the region above the proton separation energy at 15.9 MeV.

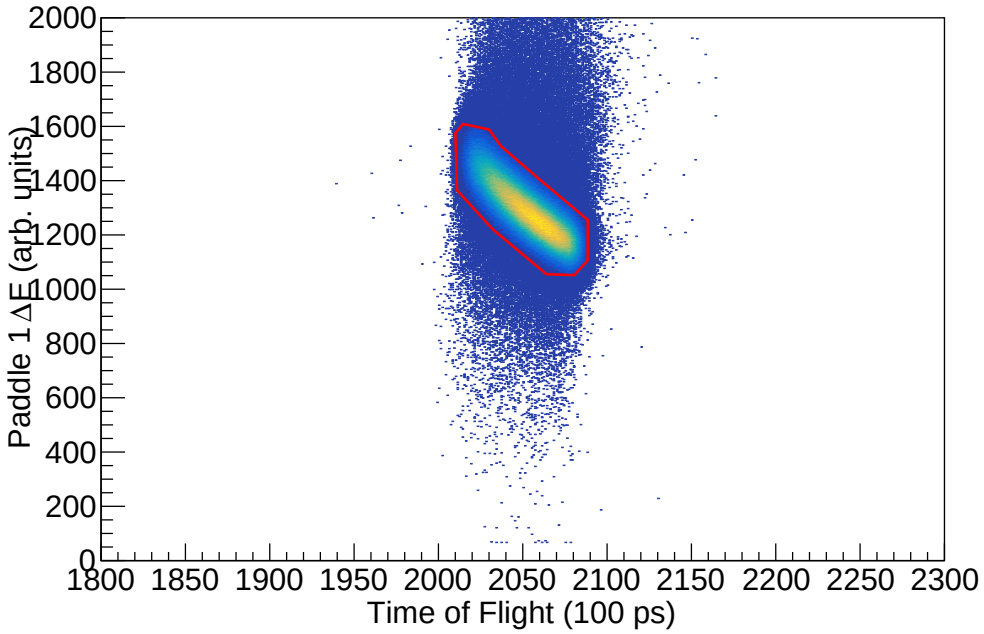

Figure 8.8: Particle identification (PID) of the K600 focal plane with the spectrometer at 8° relative to the beam direction.

In order to obtain angular distributions at a finer resolution than the 4° aperture of the K600 spectrometer, it was important to accurately determine horizontal and vertical scattering angles at the aperture. Measurements with the focal-plane detectors may be transformed into scattering angles using equations 7.1–7.3 described in chapter 7. In order to obtain the fit parameters, a special calibration collimator (shown in figure 7.8) was employed. A plot of y_{fp} vs θ_{fp} using this collimator is shown in figure 8.9, and restricted to a narrow x_{fp} region in figure 8.10. For various x_{fp} regions across the focal plane, the peak θ_{fp} and y_{fp} positions were obtained for each blob via fitting to a Gaussian distribution. The corresponding θ_{SCAT} and ϕ_{SCAT} for each of these blobs were calculated, and subsequently fitted to equations 7.4 and 7.5, via a multi-dimension linear fitter. The final calibrated ϕ_{SCAT} vs θ_{SCAT} is shown in figure 8.11. From this calibrated spectrum, it is possible to calculate Θ as given by equation 7.6. Regions of $\Delta\Theta = 1°$ were employed in order to obtain the distributions. A plot of the distribution in a normal collimator is shown in figure 8.12, with the red circle signifying the aperture of the K600 spectrometer. The same figure but focussed in a $\Theta = 1°$ region of $\Theta = 6° - 7°$ is shown in the figure 8.13. This area depends on ϕ_{SCAT}, θ_{SCAT} and θ_{K600}, and in order to calculate the differential cross-sections it is necessary to determine this area accurately. For a given Θ and θ_{K600} the maximum Φ can be

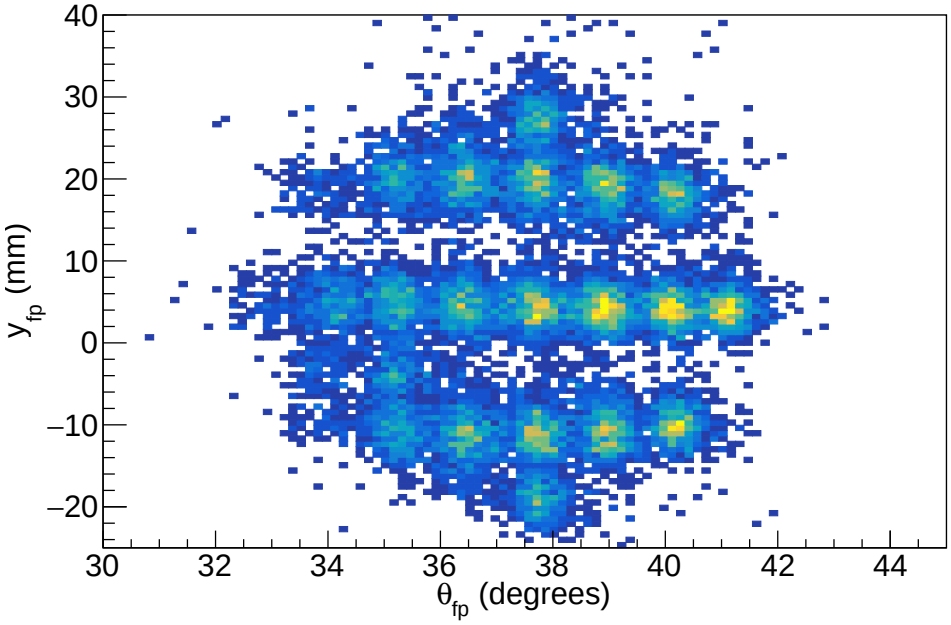

Figure 8.9: Uncalibrated scattering angles using the pepperpot calibration collimator shown in figure 7.8.

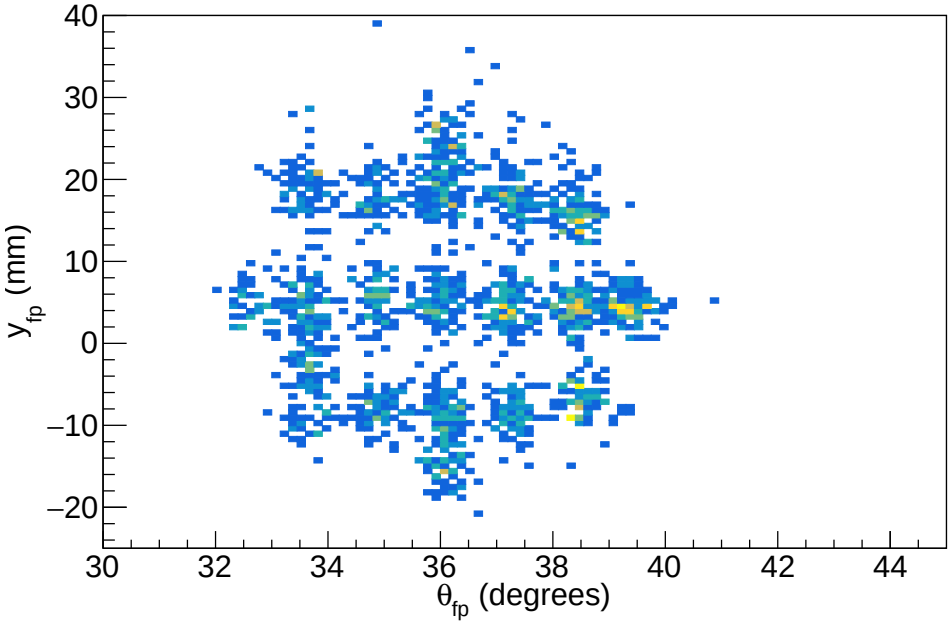

Figure 8.10: The same as figure 8.9 but focused on a single X_{fp} peak.

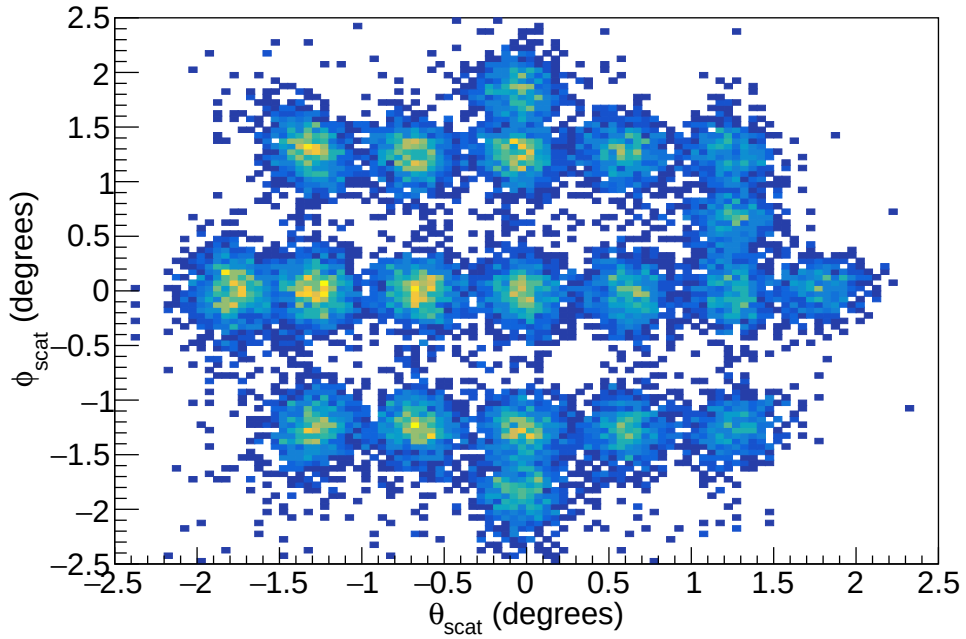

Figure 8.11: Calibrated scattering angles using the pepperpot calibration collimator

calculated as (Adsley, 2017):

$$\Phi_{max}(\Theta, \theta_{K600}) = \cos^{-1}\left(\frac{1}{\sin\Theta\sin\theta_{K600}}\left(\frac{r_0}{\sqrt{\alpha^2 + r_0^2}} - \cos\Theta\cos\theta_{K600}\right)\right), \tag{8.10}$$

and the solid angle $\Delta\Omega$ for a region between Θ_1 and Θ_2 can be obtained via integration of Θ and Φ_{max}:

$$\Delta\Omega = \int_{\Theta_1}^{\Theta_2} 2\sin\Theta\Phi_{max}(\Theta, \theta_{K600})\,\mathrm{d}\Theta\,, \tag{8.11}$$

where r_0 refers to the distance between the target and the aperture, and α the radius of the aperture. For the $\Theta = 6° - 7°$ region shown in figure 8.13 the solid angle is calculated as 0.6897 msr, for $\Theta = 17° - 18°$ with the spectrometer at 20° the solid angle is 0.73245 msr.

Once this calibration has been performed, the x_{fp} positions can be corrected for kinematic aberrations with θ_{SCAT} as described for zero degrees; the difference between different isotopes is much more noticeable than at zero degrees, as shown in figures 8.14 and 8.15, and the K600 trim coils were intentionally not tuned for optimal aberration corrections. As such, this correction is much more important than at zero-degrees, and states from isotopes other than ^{12}C will have a noticeably more distorted shape in the excitation energy

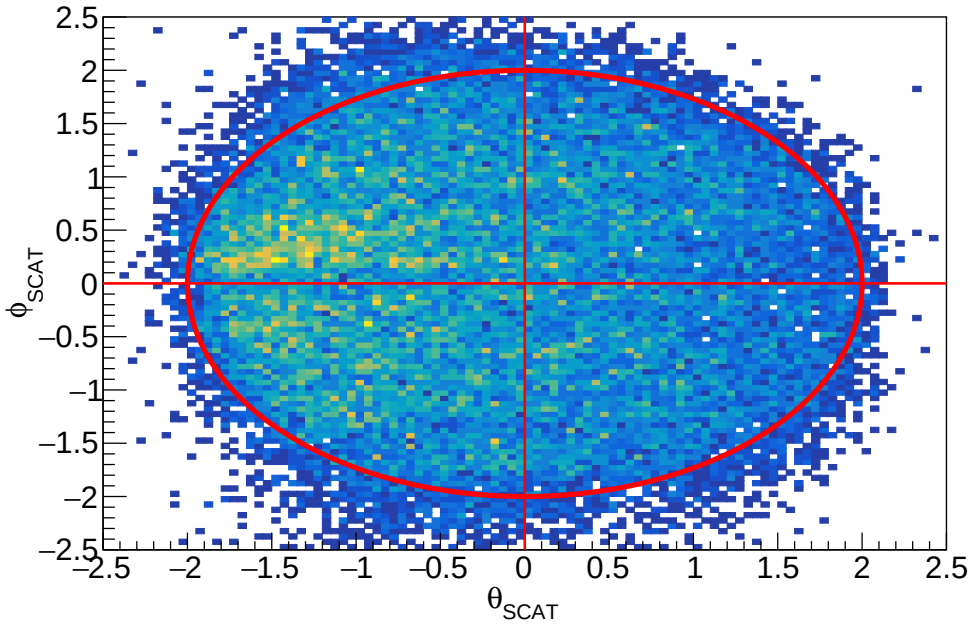

Figure 8.12: Scattering angles of the ^{11}B(^{3}He,d)^{12}C reaction at the K600 aperture at 8°. The aperture itself is signified by a red circle.

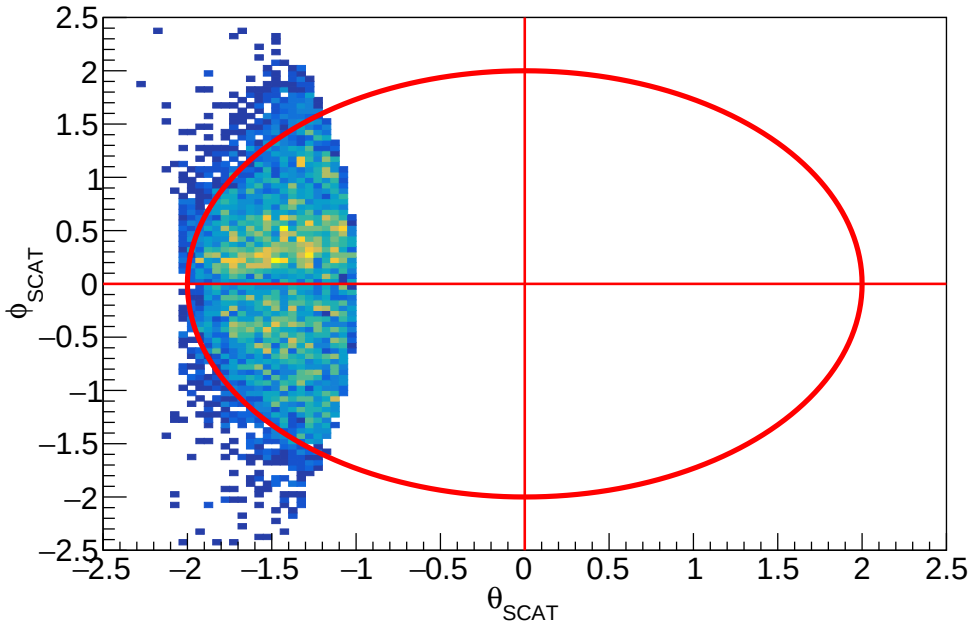

Figure 8.13: The same as figure 8.13 but restricted to the region $\Theta = 6° - 7°$.

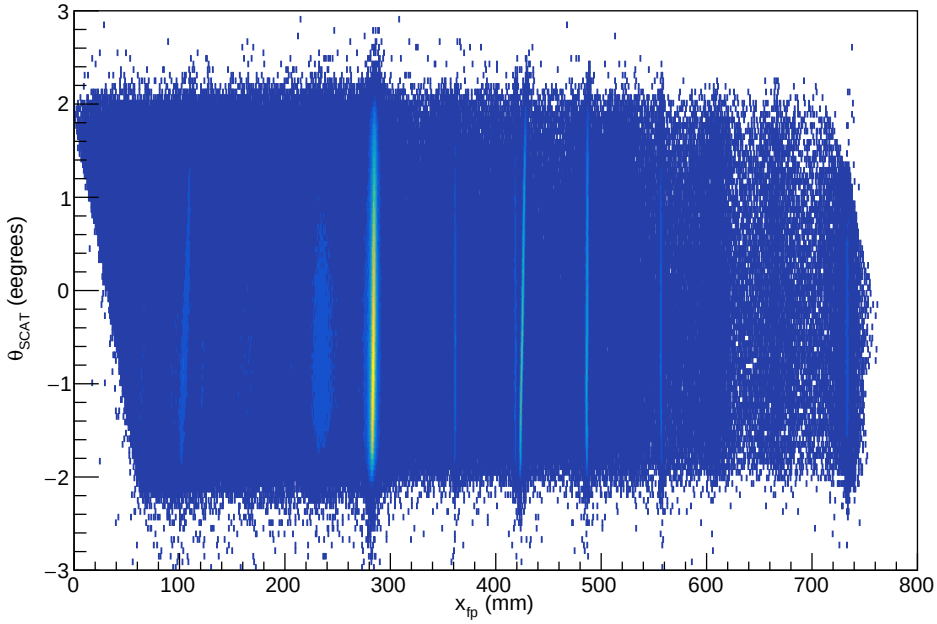

Figure 8.14: Dependence of focal-plane position x_{fp} with horizontal scattering angle θ_{SCAT} with the K600 spectrometer at 8°.

spectrum. The excitation energy spectra for all angles are shown in figure 8.16.

The efficiency of the focal-plane detector system is important for calculating the differential cross-section. For a specific wire-plane the intrinsic efficiency of the detector is given by

$$\epsilon = \frac{N_{accepted}}{N_{total}} \ , \tag{8.12}$$

where N_{total} is the total number of events recorded in the focal-plane of the spectrometer, and $N_{accepted}$ is the number of valid events recorded. For the X_1 wire-plane this can be quantitatively calculated based on the number of good events in all three wire-planes (Fujita, 2004):

$$\epsilon_{X1} = \frac{\text{Number of good events in } X_1, X_2, \text{ and } U_1 \text{ wire-planes}}{\text{Number of good events in } X_2 \text{ and } U_1 \text{ wire-planes}} \ , \tag{8.13}$$

where a good event is defined by a good particle ID cut (figure 8.8), $3-6$ wires being hit, and χ^2 (reduced) < 1. A similar calculation can be performed for the X_2 and U_1 wire-planes, and a total efficiency then calculated by multiplying the three:

$$\epsilon = \epsilon_{X1}\epsilon_{X2}\epsilon_{U1} \ , \tag{8.14}$$

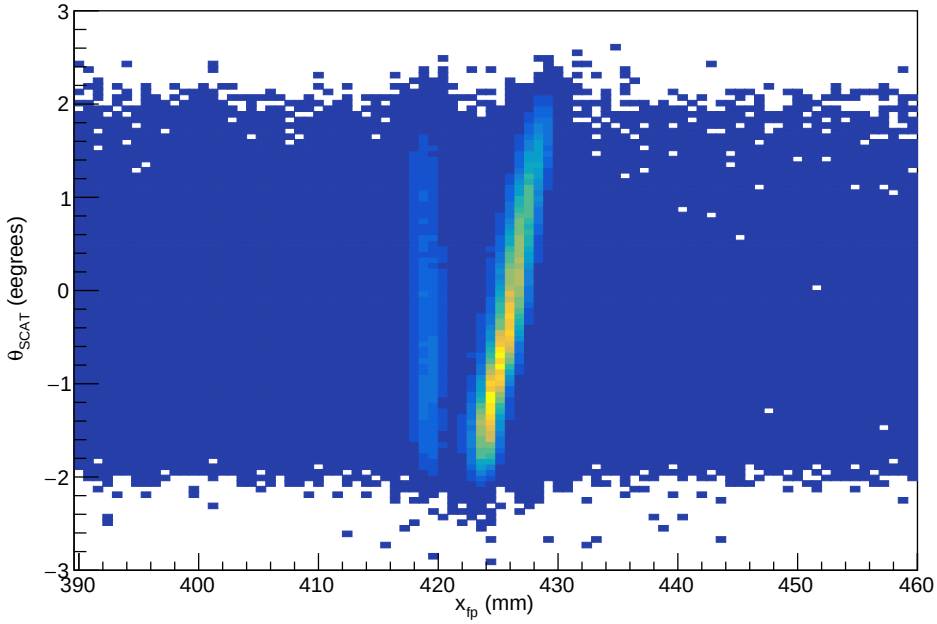

Figure 8.15: As figure 8.14 but zoomed in to highlight the different dependence of ^{12}C states (left) and background states (right).

the efficiencies calculated were approximately 90% over all the angles measured.

The integrated beam current during the measurement was recorded using a beam current digitiser, which integrates the total beam over one second, recording a value of $0 - 1000$, where 1000 corresponds to the maximum of 20 nC, although this range is adjustable during the experiment if higher beam intensities are employed. The total integrated current Q in ions is obtained by the following:

$$Q = \frac{CR}{1000q} \,, \tag{8.15}$$

where C is the sum of the 1-second values over the entire measurement, R is the range in Coulombs, and q is the electronic charge.

In order to compare the measured differential cross-sections with those calculated from DWBA it is necessary to convert the differential cross-sections from the laboratory coordinates to centre-of-mass coordinates. Assuming the cross-section solely depends on θ and not on ϕ the following relationship is obtained (Iliadis, 2008):

$$\frac{(d\sigma/d\Omega)_{cm}}{(d\sigma/d\Omega)_{lab}} = \frac{d\Omega_{lab}}{d\Omega_{cm}} = \frac{\mathrm{d}(\cos\theta_{lab})}{\mathrm{d}(\cos\theta_{cm})} \,, \tag{8.16}$$

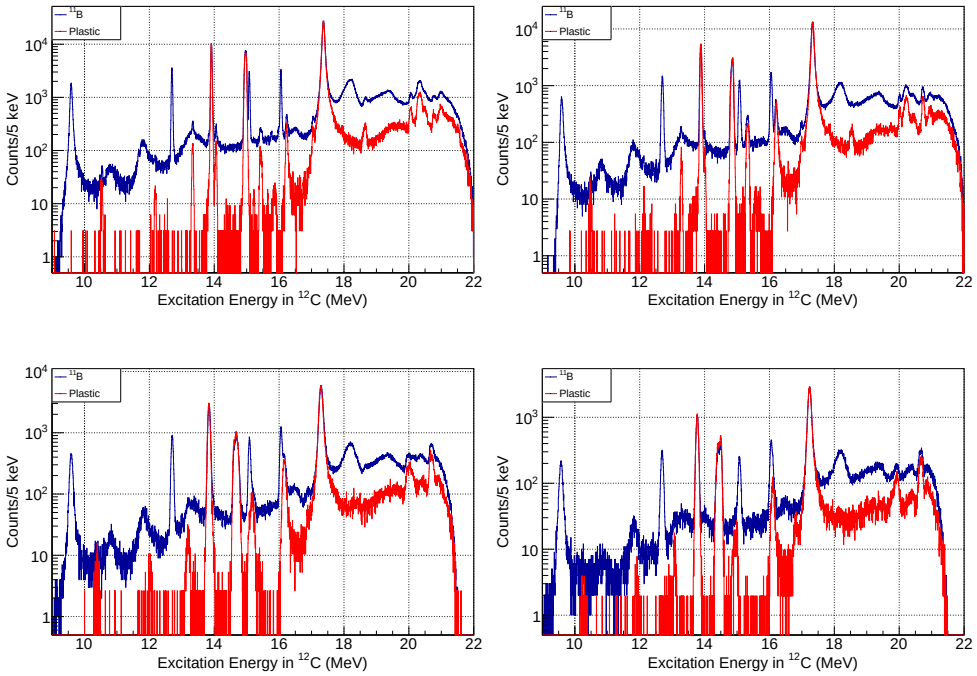

Figure 8.16: Excitation energy spectra with the K600 spectrometer set at non-zero angles. Top left: 8°, top right: 12°, bottom left: 16°, bottom right: 20°.

where θ_{cm} can be obtained from θ_{lab} via kinematic calculations such as those obtained by the program CATKIN (Catford, 2004).

8.3 SIMNEL Analysis

Compared to CAKE, analysis from SIMNEL is simpler as there is only one channel per detector, and no matching can be performed. In order to reduce background events, a timing gate was made, restricting events to within 30 ns of the peak time recorded in the TDC. Unlike CAKE there is no energy dependency of the timing. Detectors #3 and #5 were identified as being faulty with this timing gate, and were excluded from further analysis.

Energies from the SIMNEL detectors were calibrated with an AmBe-Fe source: Americium α-decays naturally, and the α-particles subsequently interact with the beryllium to produce neutrons via the ^{9}Be(α, n) reaction; these neutrons themselves interact with the iron and other elements via (n, n') and (n, γ) reactions to produce γ-rays over a large energy range. Gamma rays up to 4.44 MeV (from ^{12}C$(n, n')^{12}$C) were observed in the calibration data, with higher energy peaks being too weak to be observed clearly. An annotated

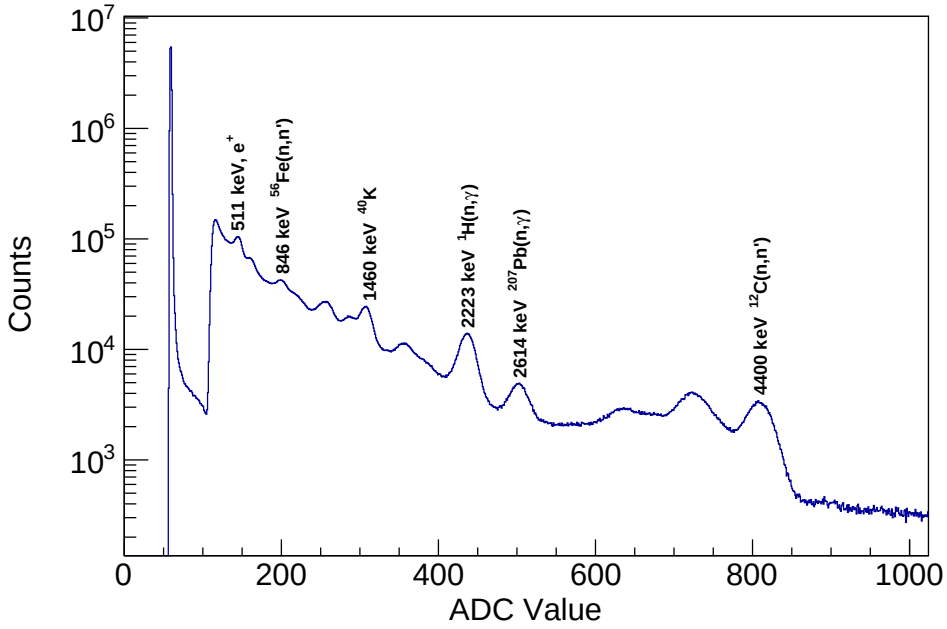

Figure 8.17: γ-ray spectrum from the AmBe-Fe calibration source, with the peaks used to calibrate the detector highlighted.

spectrum from the AmBe-Fe source is shown in figure 8.17.

Due to the need to analyse high energy γ-rays where non-linearity in the detector response is likely, an additional calibration point was taken of the 15.1 MeV γ-rays emitted from the 15.1 MeV state in ^{12}C produced by the ^{11}B(^{3}He, d)^{12}C reaction. All calibration points were fitted to a quadratic polynomial, where the quadratic coefficient was about 4×10^{-4} MeV/channel^2 for all three detectors. The 12.7 MeV γ-ray, also from ^{12}C, was used to verify the calibration, but is very weakly populated and thus excluded from the fit itself. The result of the calibration for the three detectors is shown in figure 8.18.

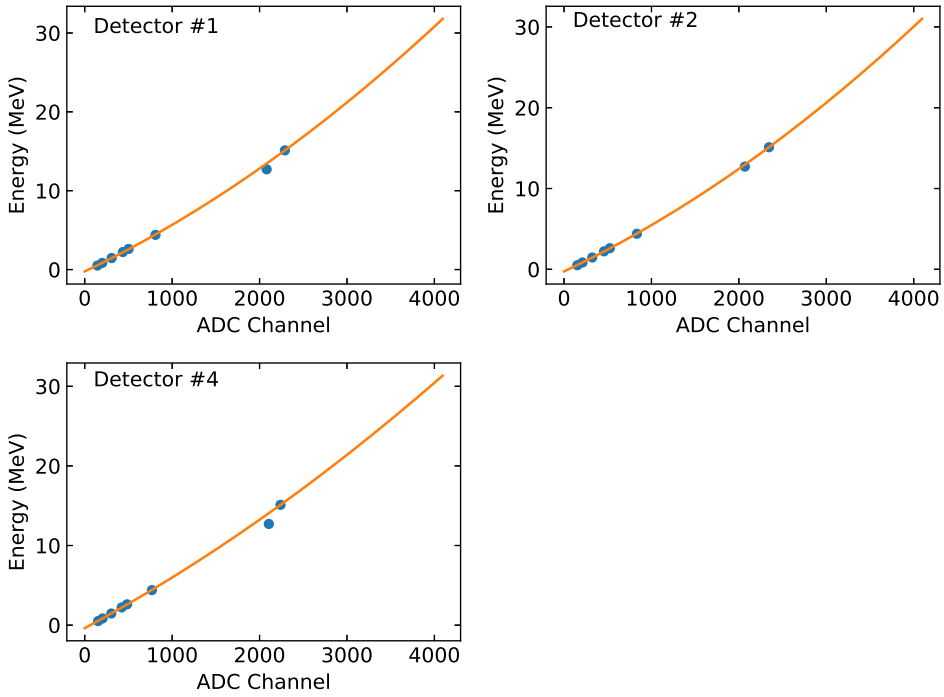

Figure 8.18: Calibration of the SIMNEL detectors. The points below 4.44 MeV were obtained from an AmBeFe source and the 15.1 MeV point from ^{12}C was used to obtain a non-linear calibration for high energies. The 12.7 MeV point from ^{12}C is shown to verify the fit but was excluded due to low statistics.

8.4 Angular Distributions and Spin Assignments

The shell-model calculations predict the 0^- state to lie in the region of 15 ± 0.5 MeV. Analysis of the states in this region show no previously unidentified states (figures 8.6, 8.16). Weak states not due to ^{12}C were observed, but are consistent with known states in ^{11}C, indicative of an expected small ^{10}B contamination within the ^{11}B target. Based on this, focus is on the 15.1 MeV state which contains contributions from both the ^{17}F ground state at small angles, and the strong 15.1 MeV 1^+ state. Angular distributions are used to identify any potential 0^- strength under this state.

The differential cross-section for a specific state at a specific Θ can be obtained from the number of counts Y within the peak observed in the excitation energy spectra. The number of counts were obtained after subtracting a linear background obtained via the fitting of a Gaussian plus a linear background, the Gaussian parameters were not used, instead the number of counts was obtained from the histogram. The centre-of-mass differential cross-section is given by:

$$\frac{\mathrm{d}\sigma}{\mathrm{d}\Omega}(\Theta) = \frac{Y}{N_t Q \Delta\Omega_{cm} \epsilon} \,, \tag{8.17}$$

where N_t is the number of ions in the target: $N_t = N_A t/A$, with t being the target thickness in g/cm^2, A the target mass in amu, and N_A is Avogadro's number. Q is the beam current from equation 8.15, $\Delta\Omega_{cm}$ is the centre-of-mass solid angle obtained by converting the lab solid angle from equation 8.11 with equation 8.16, and ϵ is the efficiency of the K600 from equation 8.14. The differential cross-section at zero-degrees was obtained over the total aperture, whereas at non-zero angles the cross-section was obtained in 1° intervals, for 4 points over the 4° aperture.

In order to verify the comparison of experimental and DWBA cross-sections, evaluations of well-known states were performed. For $\ell = 1$ two narrow strong states at 12.7 MeV (1^+) and 16.1 MeV (2^+) were used, shown in figure 8.19. The DWBA cross-sections were scaled so that the zero-degree point matches experiment. Agreement between experiment and DWBA is very good, particularly up to the first minimum. For other values of ℓ comparisons are more complex due to the lack of states, the $\ell = 0$ transfer to the 10.8 MeV 1^- state is shown in figure 8.20, where the sharp drop between 0° and 8° is well reproduced. As a broad state ($\Gamma = 315$ keV) there are difficulties with a full comparison of the DWBA predicted distributions and experimental data, in addition a broad 0^+ background is known to be present in this region, which will provide an $\ell = 3$ contribution to the angular distribution. The predicted 0^- state will have an $\ell = 2$ distribution, which would be matched by the 3^- state at 9.6 MeV, however this state is at the edge of the focal-plane's acceptance and obscured by a strong resonance at 9.5 MeV from the first excited state of ^{11}C at 2.0 MeV, from the ^{10}B impurities

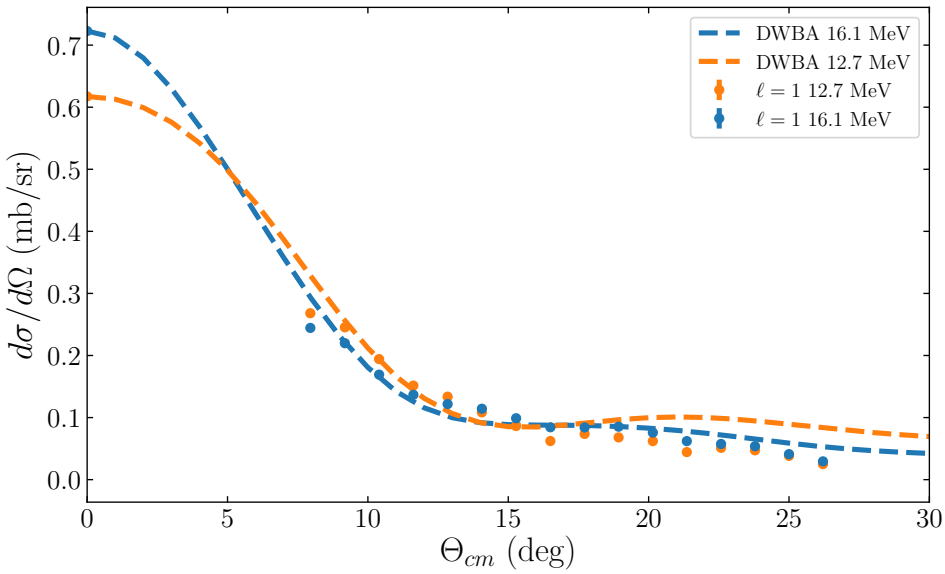

Figure 8.19: Experimental differential cross-sections and DWBA predicted angular distributions for two well-known $\ell = 1$ states in ^{12}C. The DWBA differential cross-sections are scaled to the zero-degree experimental data point. The error bars are plotted but are too small to be visible.

in the target. The good description of $\ell = 0, 1$ states shown indicate than any $\ell = 2$ contribution due to the 0^- state can be well identified.

With the confirmation that DWBA describes states well, the 15.1 MeV region was analysed, and compared to both the $\ell = 1$ distribution from the known 1^+ state and the $\ell = 2$ distribution from any 0^- strength within the region. The results are shown in figure 8.21. No point at 0° was obtained due to the overlap with the ^{17}F ground state at this energy. The separation between the ^{12}C state and the ^{17}F increases with Θ and there is still potential overlap at $6° - 10°$. Due to this the DWBA cross-sections were adjusted to match at 12°, where the contaminant is well separated. The points reproduce the $\ell = 1$ distribution well, as expected, with no indication of significant $\ell = 2$ distribution. Further analysis of 0^- strength is obtained from the γ-ray coincidence analysis in the next section.

8.5 γ-decay of the 15 MeV Region

The angular distributions in the previous section are entirely consistent with the 15.1 MeV strength solely being due to the known 1^+ state. A more rigorous analysis of potential 0^- strength can be performed by utilising the γ-ray coincidence data from SIMNEL. The 1^+ state is known to decay primarily

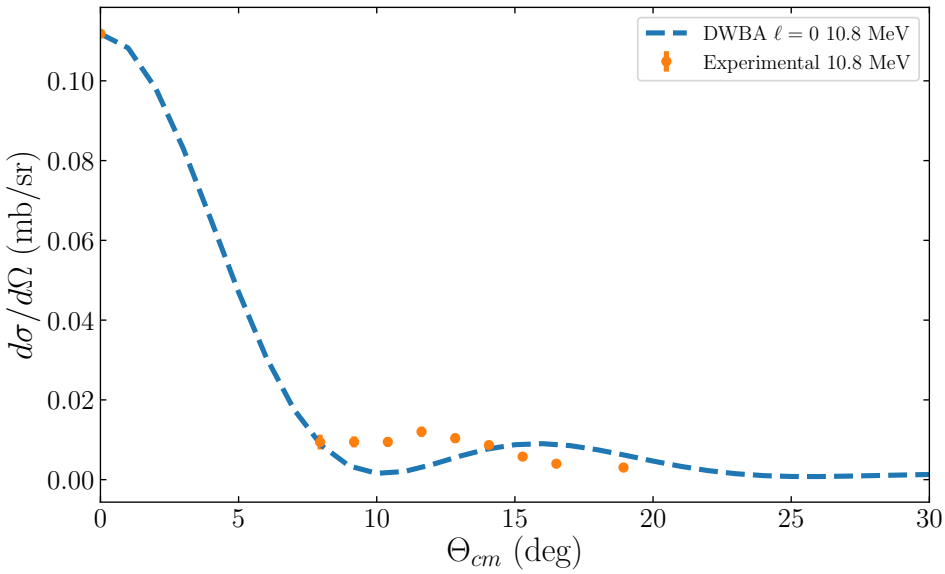

Figure 8.20: Experimental differential cross-sections for 10.8 MeV $\ell = 0$ states and DWBA predictions. The 10.8 MeV state is a broad state, which will reduce the reliability of DWBA predictions. The DWBA differential cross-sections are scaled to the zero-degree experimental data point. The error bars are too small to be visible.

to the ground state, with approximately 2% of decays occurring via the 4.44 MeV state. Conversely, the 0^- is predicted to decay primarily to the 4.44 MeV state. Calculation of the observed branching ratio can indicate the presence of any 0^- strength in this region.

A 2D plot of γ-ray energy vs the excitation energy in ^{12}C is shown in figure 8.22. Lines corresponding to decays to the ground state (γ_0) and from the 4.44 MeV state to the ground state are shown by red lines. To identify the potential 0^- state alongside the 15.1 MeV state a projection of the γ-ray spectra from $15 - 15.2$ MeV was taken, which is shown in figure 8.23. From this graph we can see 1681 counts within the 15.1 MeV region, from the 1^+ state which primarily decays directly to the ground state ($E_\gamma = 15.1$ MeV).

At the 4.44 MeV region the number of events above the background was 187(22), compared to the number of events in the 15.1 MeV region which is 1681(41). Using calculated detector efficiencies of 0.46% at 4.44 MeV and 0.07% at 15.1 MeV yields an intensity of the 15.1 MeV peak normalised to the 4.44 peak of 11046(270), and assuming the branching ratio of the 15.1 MeV state to the ground state as 92% from Alburger & Wilkinson (1972) we calculate a branching ratio to the 4.44 MeV state of at most 1.6(10)%. This is consistent with the previously measured branching ratio of 2.3(9)% (Alburger

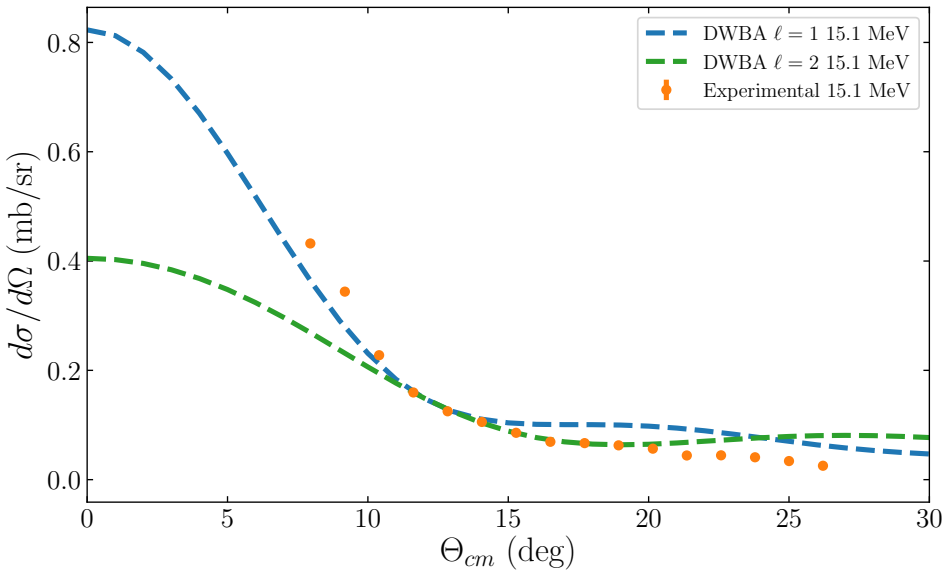

Figure 8.21: Experimental differential cross-sections for the 15.1 MeV state. Comparison with DWBA predictions for $\ell = 1$ from the known 1^+ state and $\ell = 2$ from the potential 0^- state are included. The DWBA differential cross-sections are scaled to the zero-degree experimental data point. The error bars are too small to be visible.

& Wilkinson, 1972).

There is therefore no evidence from the angular distributions or the γ-ray data for the existence of a 0^- state in the region of 15.0 ± 0.5 MeV. This is particularly significant considering the high cross-sections predicted by shell-model calculations for population via the (^{3}He,d) mechanism. Further analysis will therefore focus on the region above the proton separation energy, where no-core shell models place the state.

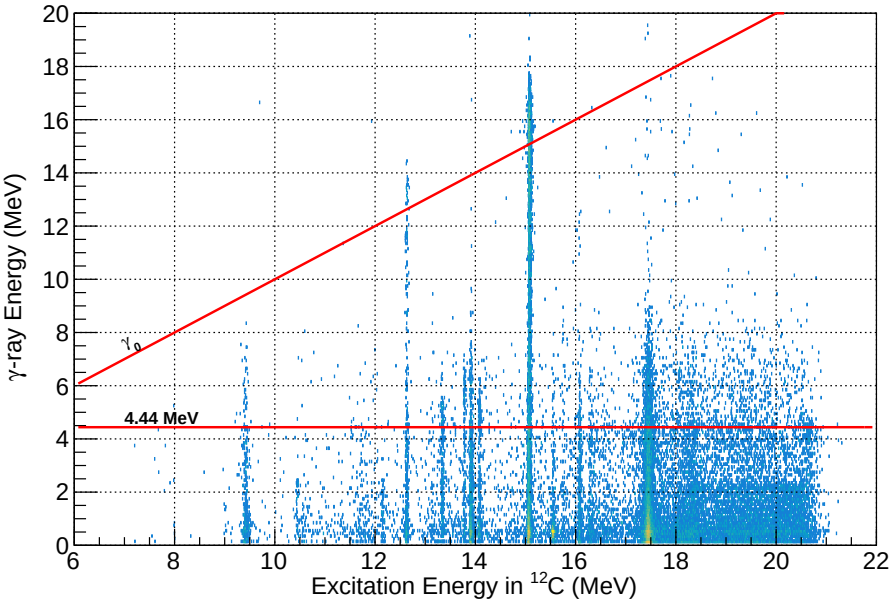

Figure 8.22: 2D histogram of γ-rays in coincidence with deuterons. The decays to the ground state (γ_0) and 4.44 MeV γ-rays from the first excited state to the ground state are shown by red lines.

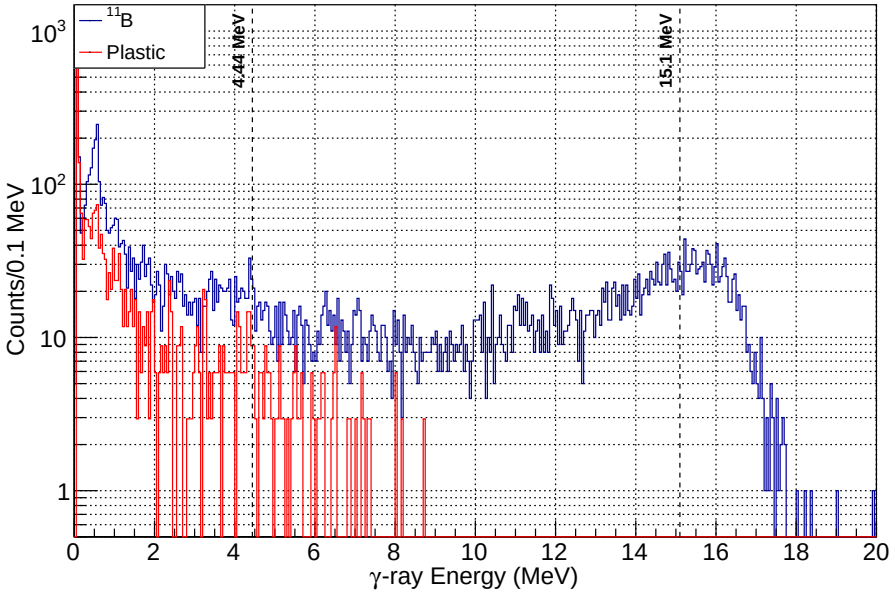

Figure 8.23: Projection of figure 8.22 showing the γ-ray spectra from the 15.1 MeV region in ^{12}C.

Chapter 9

Analysis of ^{12}C Above the Proton Threshold

9.1 CAKE Analysis

Raw data from CAKE is mapped to physical events by looking for events which are recorded in both the front strip (junction) and rear strip (ohmic) TDC channels for a single detector. The corresponding ADC values recorded are then checked to verify both front and rear strip values exceed a defined ADC value threshold and are within approximately 100 keV of each other. If this test passes the front-back pair is considered a good silicon hit, and the energy, time and position are recorded. The pixel position is identified from the TDC channels. Time values are aligned such that the peak time for each channel, after adjusting for spectrometer time-of-flight, occurs at the same value. Energy values are obtained from the ADC value by performing a linear fit to calibration data using a ^{228}Th source, which emits α-particles of fixed, known, energies. A calibration spectrum for a single channel is shown in figure 9.1.

With both energy and time information, particle identification can be performed, by plotting silicon time against silicon energy. For a given energy, α-particles will have a slower velocity and hence will be detected later than protons. Due to the timing being relative to the time the focal-plane registers an event, which occurs after the silicon detectors register an event, a greater time value corresponds to an earlier event time. Due to the alignment procedure discussed above the absolute value is arbitrarily set such that 0 corresponds to the peak time value. This is shown in figure 9.2 where two distinct regions are observed, with the top region corresponding to detected protons and the bottom region to detected α-particles. The gates used in the following analysis are also highlighted. As α-particles can be emitted with a higher energy within the accepted excitation energy range, the α-particle gate extends to higher energies. The proton region can be observed to divide

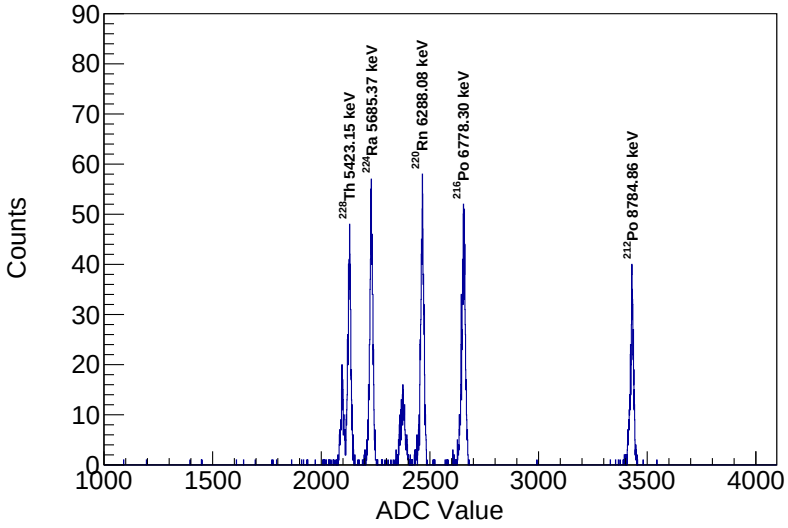

Figure 9.1: Silicon ADC Values for the ^{228}Th calibration source, with the peaks from α-particle decays used for calibration highlighted.

into two at high energies, with the bottom line corresponding to scattered deuterons, this occurs at energies higher than possible for protons emitted from ^{12}C.

9.2 Decays above 18 MeV

For analysis above the proton separation energy, the dominant decay mode for the 0^- state shifts to proton decay instead of γ-ray decay, and as such charged particle data from CAKE is analysed. Because both proton and α decay channels are open at these energies, it is important to be able to discriminate the two particles in CAKE. In addition to searching for the 0^- state, other states in this region have tentative or missing spin/parity assignments (Kelley et al., 2017) which can be identified by the present work.

A 2D coincidence plot of α-particle energy vs ^{12}C excitation energy is shown in figure 9.3 and the region above the proton threshold is shown in more detail in figure 9.4. These α-particle spectra are made more complicated due to the fact that the nucleus which ^{12}C α-decays into – ^{8}Be – also α-decays into two α-particles promptly. The two regions corresponding to α-decay to the ^{8}Be ground state (0^+) and to the ^{8}Be first excited state (2^+) are shown in the two figures. The available decay channels can give insight into the states' spin and parity, for example states with unnatural parity ($\pi \neq (-1)^J$) cannot decay into the ^{8}Be ground state.

A similar 2D coincidence plot for the proton case is shown in figure 9.5. Compared to α-particles the kinematics are simplified due to the fact that ^{12}C

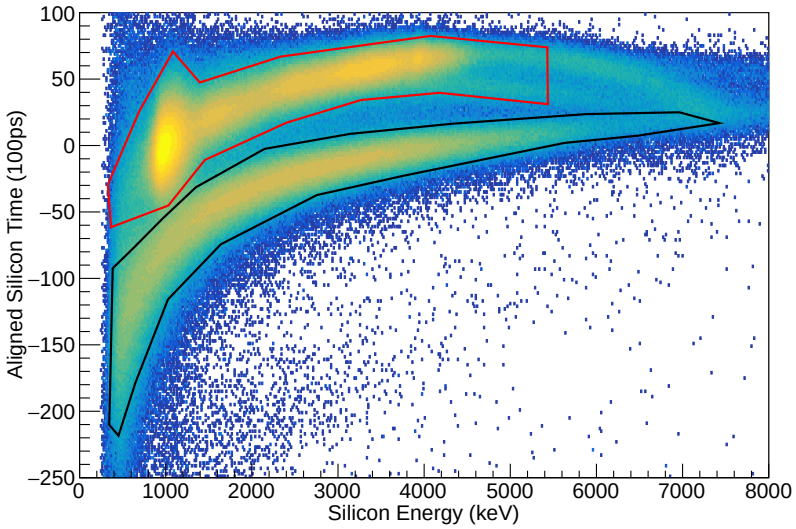

Figure 9.2: Silicon energy vs silicon time (corrected for time of flight differences). The protons and α-particles are visible as two distinct loci. The α-particles locus is shown in black, and the proton locus is in red.

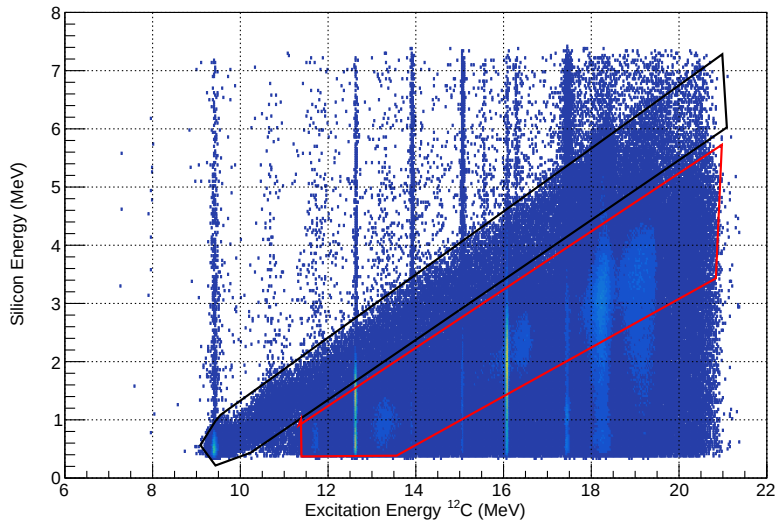

Figure 9.3: 2D histogram of deuterons in the K600 in coincidence with an α particle in CAKE. The two diagonal loci correspond to α particles to the ground state (black) and first excited state of ^{8}Be (red).

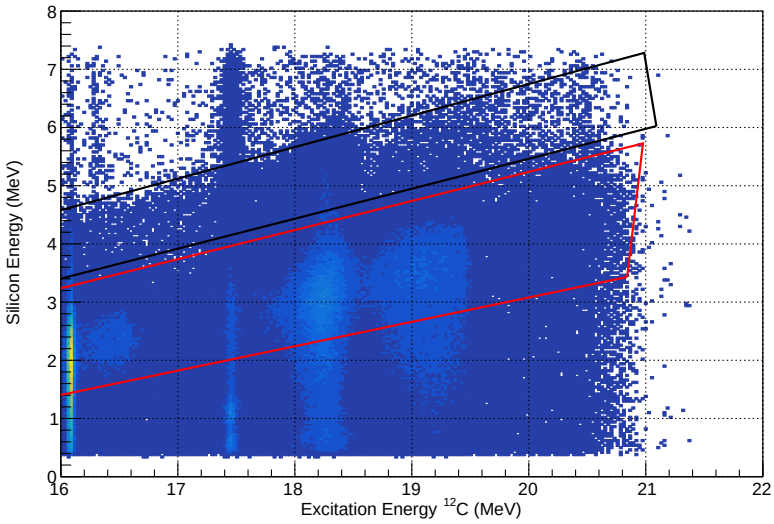

Figure 9.4: Same as figure 9.3 but focusing on states above the proton separation energy.

proton decay is a two-body process. This and the reduced straggling result in an improved energy resolution for the decay particle. Separation of the regions corresponding to ^{12}C proton decay and ^{17}F proton decay due to ^{16}O contamination in the target can be observed. p_0 decays to the ground state of ^{11}B, with a spin/parity of $3/2^-$, are observed from 18 MeV upwards, with the strong ^{13}N background state obscuring decays in the 17 MeV region. p_1 decays to the first excited state of ^{11}B, at 2.12 MeV and with a spin/parity of $1/2^-$, can be observed at energies above 19 MeV. For observation p_1 decays closer to the p_1 threshold (18.1 MeV) it is possible to utilise the SIMNEL array, looking for coincidences with the 2.12 MeV γ-decay from the first excited state of ^{11}B, this γ-gated p_1 spectrum is shown in figure 9.6.

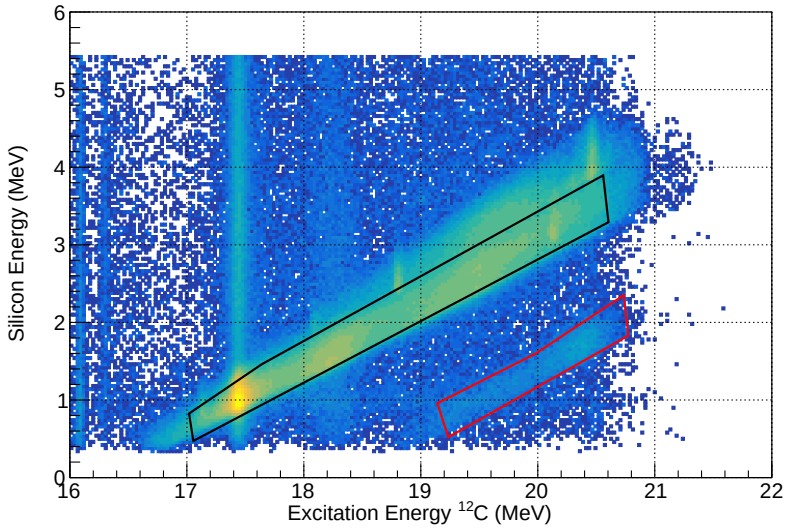

Figure 9.5: 2D histogram of deuterons in the K600 in coincidence with a proton in CAKE. The two diagonal loci correspond to protons to the ground state (black) and first excited state of ^{11}B (red). The states above the ground state loci are from ^{16}O in the target backing.

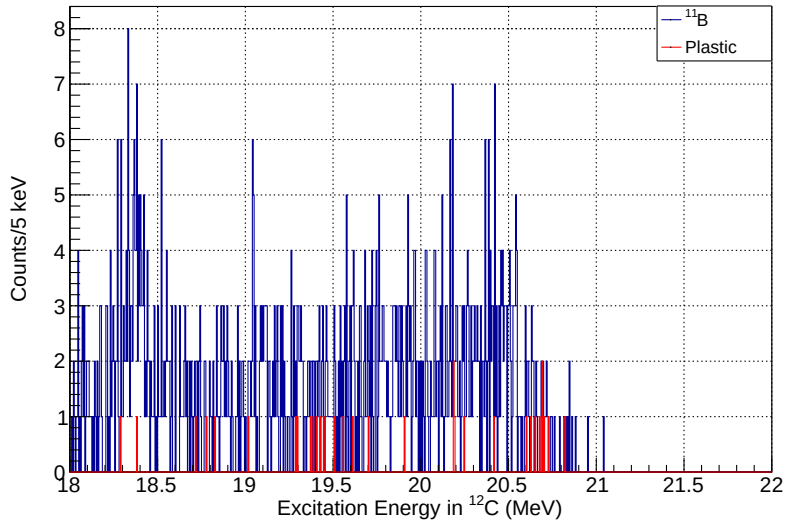

Figure 9.6: ^{12}C excitation energy spectrum measured in coincidence with a 2.1 MeV γ-ray from the decay of the first excited state in ^{11}B, identifying p_1 decays within ^{12}C.

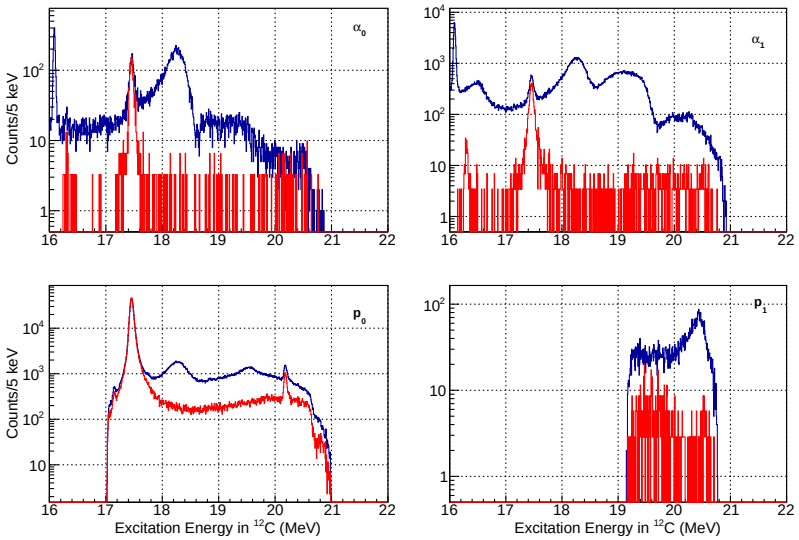

Figure 9.7: ^{12}C excitation energy spectra gated on the specific charged particle decay channels.

9.3 Identification of states

From the coincidence spectra shown in the previous section, information on states in ^{12}C and their spins and parities can be obtained. For example: states undergoing α-decay to the ground state of ^{8}Be can only be natural parity ($\pi = (-1)^J$) states. The region of interest is states near the proton threshold, around $18 - 20$ MeV, which is where the no-core shell model places the 0^- state. Excitation energy spectra gated on type of particle decay are shown in figures 9.7 and 9.8.

The region $17.6 - 18.6$ MeV is composed of two or more states, due to its asymmetric appearance tailing off more slowly at lower energy: a single peak would be asymmetric in the opposite direction. Two states have been tentatively observed in this region, one at 18.160(70) MeV with a spin-parity assignment of 1^+ and one at 18.350(50) MeV with a spin-parity assignment of $3^-/2^-$. Both states undergo α-decay to both the 0^+ and 2^+ states of ^{8}Be. Neither state is consistent with a 0^- configuration.

In the γ-gated p_1 data, shown in figure 9.6, there is a state at 18.4 MeV which cannot be seen in the other spectra due to dominance from the stronger 18.35 MeV state. A state with this energy has been previously seen in ^{11}B$(p,p')^{11}$B (Bair et al., 1955; Segel et al., 1965), and was assigned 0^- based on an assignment of $\ell = 0$ for the detected protons, and determining that a 1^- is inconsistent with the observed narrow widths (Segel et al., 1965). The state was not identified in elastic scattering (p_0), and the large strength of the 18.35 MeV state was attributed as one of the possible causes (Segel et al.,

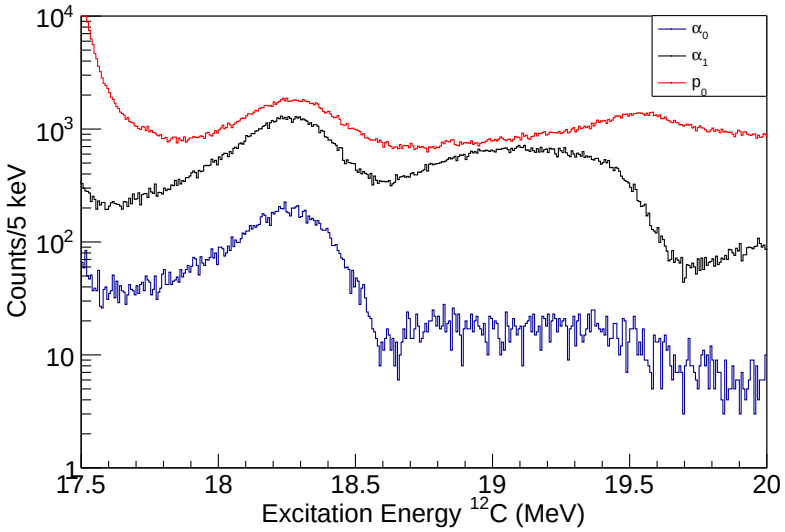

Figure 9.8: Overlay of ^{12}C excitation energy spectra for α_0 (blue), α_1 (black) and p_0 (red).

1965).

A strong peak is observed in the α-decay to the 2^+ state in ^{8}Be (α_1). The shape is again inconsistent with a single state. In this region only one state has been previously identified, at 19.2 MeV with a width of 1.1 MeV and spin/parity of 1^-. In the proton decay to the ground state of ^{11}B (p_0) there is a peak observed at 19.5 MeV. This is consistent with an observed 19.550(5) MeV state, with a width of 490 keV and a spin/parity of 4^-. This state is not observed in the α-decay spectra, and would be excluded from α_0 decay via parity conservation.

Peaks at 20 MeV can be seen in the spectra for both α_1 and p_1 decays, and seem to be independent states. The state undergoing α_1 decay may correspond to the 20.270(50) MeV (1^+) state, which has not been observed in ^{11}B(^{3}He,d) before. The state undergoing p_1 decay peaks at 20.4 MeV and may correspond to the 20.5(1) MeV (3^+) state, which has also not been observed in ^{11}B(^{3}He,d) before. The unnatural parity of these states is consistent with the non-observation in the α_0 spectra.

A summary of the states identified is shown in table 9.1. The spins listed are taken from previous work when identified. Further analysis using R-matrix theory is discussed in the following section and can calculate the energies and widths of the state, and constrain the spin-parity assignments.

Table 9.1: Summary of states above the proton threshold in ^{12}C.

Energy (MeV)	Previous J^π	Observed Decays
18.1[1,2]	(1^+)	α_0, α_1
18.3	$2^-/3^-$	α_0, α_1, p_0
18.4[2]	(0^-)	p_1
19.2	(1^-)	α_1
19.3[3]	—	α_1
19.5	(4^-)	p_0
20.3[2]	(1^+)	α_1
20.5[2]	(3^+)	p_1

[1] Previous spin assignment inconsistent with decay mode
[2] Not observed in ^{11}B(^{3}He,d)^{12}C before
[3] Not observed before

9.4 R-matrix Analysis of States

The states in the 18-20 MeV region summarised in 9.1 were fitted using R-matrix theory and AZURE discussed in chapter 6, modelling the reaction as $^{11}\mathrm{B}(p_T, x)$, where p_T refers to a proton transferred via the (^{3}He,d) mechanism, and x to either a proton or alpha decay. The four output channels included were $\alpha_0, \alpha_1, p_0, p_1$, using an R-matrix radius of $a = 5$ fm. The yield data were divided into the regions of $18 - 19$ MeV, $19 - 20$ MeV in order to simplify the fitting procedure. Background poles at an energy of 25 MeV were included to account for higher lying states and non-resonant contributions to the cross-section. The p_1 channel identified from SIMNEL data is fitted separately to the data from CAKE.

The 18 MeV region

One previous states has been identified in the region of 17.6-18.6 MeV via ^{11}B(^{3}He,d)^{12}C : At 18.350 MeV, with two definitions: one with spin-parity 3^- and width 220 keV, and the other with spin-parity 2^- and width 350 keV. The presence of α_0 data excludes a 2^- assignment. Additionally, the shape of the spectra implies more than one state. This is visually demonstrated in figure 9.9, where a single 3^- state is fitted, with $\chi^2 = 3307$.

A better fit was obtained by including a second 3^- state in order to describe the high energy drop-off in the α_0-gated spectra. In addition, including a non-interfering 1^- state explained the long low-energy tail present in the spectra. This fit is shown in figure 9.10, with $\chi^2 = 254.7$. The parameters' errors were calculated using the MINOS subroutine, and the final parameters are shown in table 9.2. None of these states are consistent with a 0^- configuration.

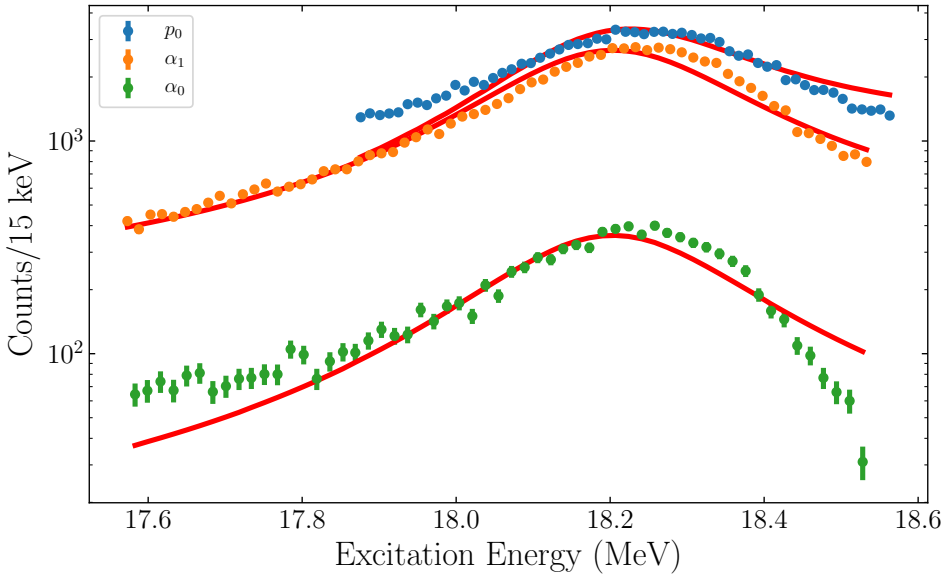

Figure 9.9: R-matrix fit to a single state in the 18.2 MeV region, plus one background pole at 25 MeV.

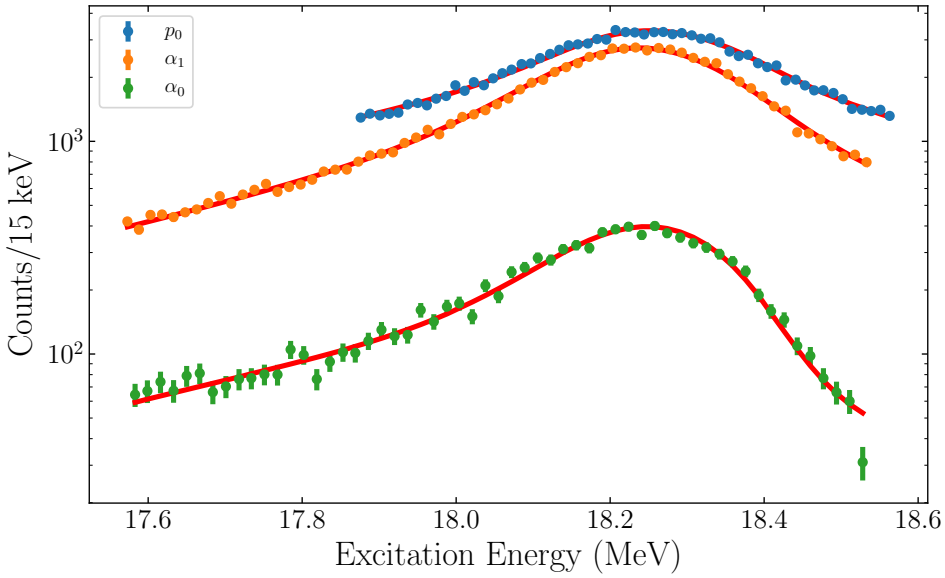

Figure 9.10: R-matrix fit to three states in the 18.2 MeV region, plus one background pole at 25 MeV. The two interfering 3^- are necessary to explain the α_0 structure at high energies.

Table 9.2: States obtained from R-matrix fitting to the region 17.6 MeV - 18.6 MeV.

Energy	J^π	Γ
18.05(4) MeV	1^-	1.21(5) MeV
18.232(2) MeV	3^-	371(6) keV
18.398(9) MeV	3^-	285(10) keV

Table 9.3: States obtained from R-matrix fitting to the region 18.6 MeV - 19.6 MeV.

Energy	J^π	Γ
18.87(1) MeV	1^-	850(10) keV
19.63(4) MeV	1^-	480(20) keV

The 19 MeV region

Previous data on the 19.2 MeV region has identified one state at 19.2 MeV, with tentative spin-parity assignment 1^- and a width of 1.1 MeV, previously observed via the ^{11}B(^{3}He,d)^{12}C reaction. However the shape of the state observed in the present work is more complex than can described by a single state. This is confirmed by R-matrix analysis of a single 1^- state to this region, as shown in figure 9.11. The fit quality is visually poor, with $\chi^2 = 5256$ and $N = 75$. This can be quantitatively analysed by evaluating $\sqrt{2\chi^2}$, which converges to a Gaussian with $\mu = \sqrt{2n_{dof} - 1}$ and $\sigma = 1$ for large n_{dof}, where n_{dof} is the number of degrees of freedom (Barlow, 1989). These two values are 102.5 and 12.2 respectively, hence the likelihood of this χ^2 being due to statistical fluctuations is very low.

R-matrix analysis including a second state of spin-parity 1^- is shown in figure 9.12, where the two states with equal spin-parity permit interference effects to be accounted for. Allowing two states produces a qualitatively better fit, with $\chi^2 = 87.9$ and $n_{dof} = 72$. Performing the same quantitative analysis as above yields $\sqrt{2\chi^2} = 13.2$ and $\sqrt{2N - 1} = 11.9$, within the 95% confidence interval. The uncertainties were analysed using the fit routine MINOS, and the properties of the states are shown in table 9.3.

The 18.4 γ-gated observation in the ^{11}B* channel

A narrow state was identified in data gated on γ-rays from the first excited state in ^{11}B, with potential spin-parity 0^- based on previous identification by Segel et al. (1965). A constant background is present in the γ-ray coincidence data, noted by events around the p_1 threshold of 18.1 MeV. The background

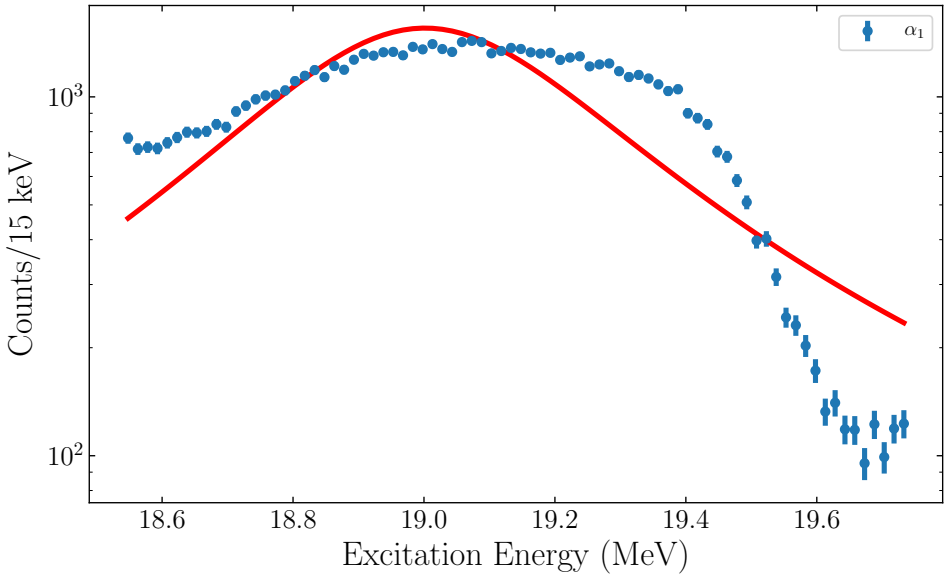

Figure 9.11: R-matrix fit to one state in the 19.2 MeV region, plus one background pole at 25 MeV. The data are visually and quantitatively poorly explained by a single state.

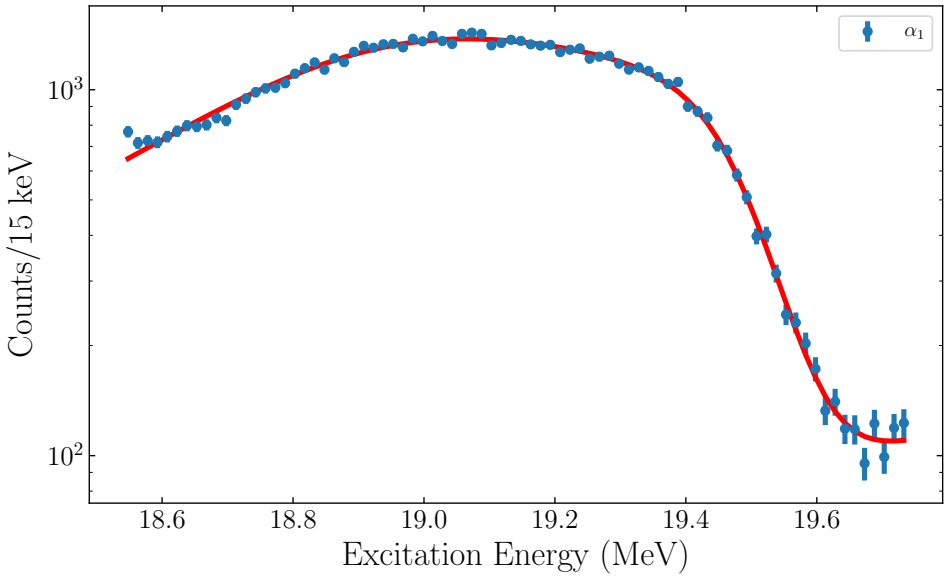

Figure 9.12: R-matrix fit to two interfering states in the 19.2 MeV region, plus one background pole at 25 MeV. The fit results are: 1^- state at 18.87(1) MeV, $\Gamma = 850(10)$ keV and 1^- state at 19.63(4) MeV, $\Gamma = 480(20)$ keV.

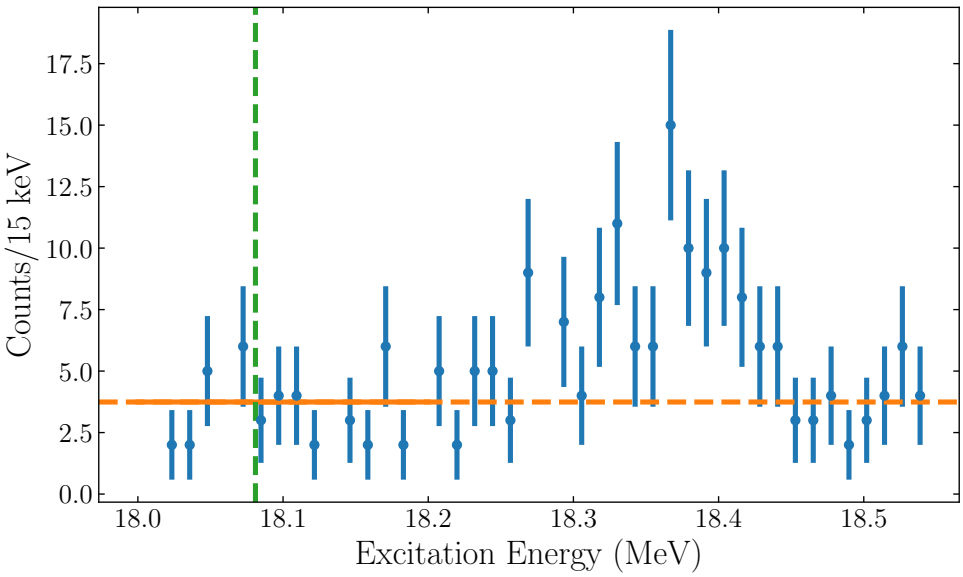

Figure 9.13: ^{12}C excitation energy spectum gated on γ-rays from p_1 decay in the 18.4 MeV region. The constant background is estimated from the region around the p_1 separation energy of 18.1 MeV, shown as a solid line in the background region, and a dashed line outside.

was calculated by taking a weighted average of the data between 18.0-18.2 MeV, producing an estimated background of 3.7 ± 0.5 counts. This is shown in figure 9.13. This background was subtracted from all data points before R-matrix fitting, and the error added to the $\sqrt{N}$ Poissonian error in quadrature.

The fitting procedure involved a single 0^- state at approximately 18.375 MeV to the background subtracted data. The 0^- state cannot decay via α decay, and but can decay by both p_0 and p_1 decay, although only p_1 data is used for fitting. The impact of the p_0 width was investigated and is shown in table 9.4. The optimal χ^2 is for zero p_0 width, which is due to the lack of information on the p_0 width available in the data: the fit is mostly sensitive to $\Gamma_{total} = \Gamma_{p0} + \Gamma_{p1}$. Zero p_0 width was used for the subsequent fits, and the results can be considered an upper limit on Γ_{p1}.

The resonance energy and p_1 width were subsequently fitted with zero p_0 width in order to obtain the optimal parameters. The calculated values were $E_R = 18.375$ MeV and $\Gamma_{p1} = 37$ keV, with $\chi^2 = 20.2033$. This fit is shown in figure 9.14. Due to the low statistics, the MINOS routine was unable to determine the errors on the fit parameters.

In order to evaluate the errors on the parameters, multiple fits were made with the parameter to analyse fixed at values around the minimum, while other parameters were allowed to be minimised. The distribution of χ^2 around

Table 9.4: Parameters of the potential 0^- state with varying Γ_{p0}.

Γ_{p0} (keV)	E_R (MeV)	Γ_{p1} (keV)	χ^2
0	18.374	36.9	20.2033
20	18.370	2.8	20.9153
40	18.371	4.2	20.279
60	18.365	6.1	22.38
80	18.372	20	23.7167

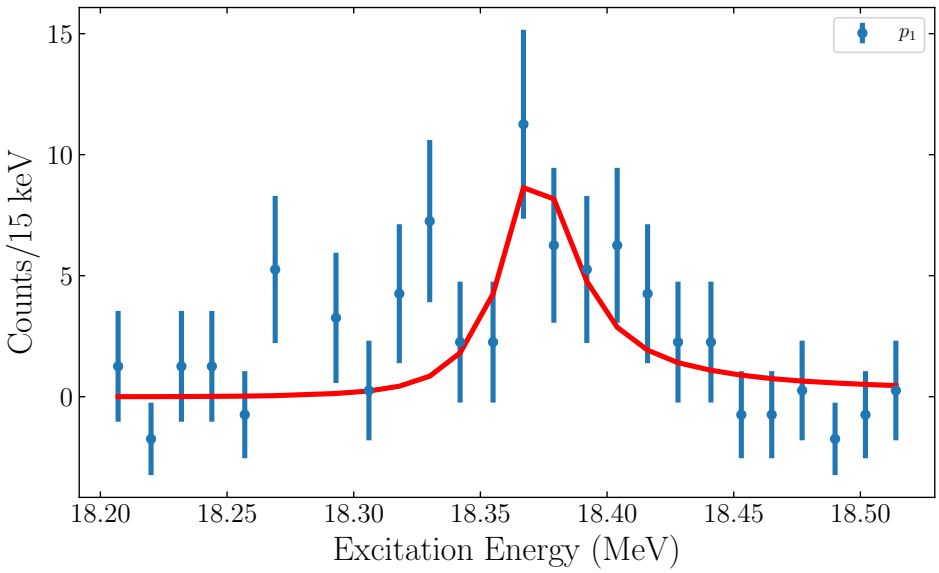

Figure 9.14: R-matrix fit to the γ-gated p_1 decay 18.4 MeV region, after background subtraction.

the optimal value allows evaluation of the error, with the 1σ uncertainties occurring at $\Delta\chi^2 = 1$ [1]. The variation of χ^2 is shown in figure 9.15 for E_R and figure 9.16 for Γ_{p1}. From these figures the fit parameters are E_R =18.375$(^{+7}_{-6})$ MeV and $\Gamma = 37(^{+20}_{-14})$ keV.

[1]This calculation is what MINOS tries to automate, however the low statistics lead to an unstable fit which causes the algorithm to fail

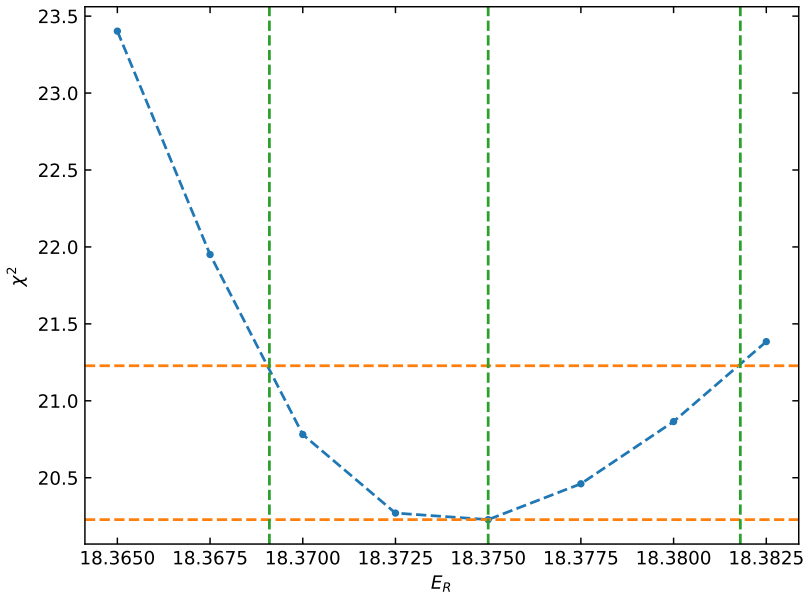

Figure 9.15: χ^2 as a function of E_R for the state around 18.4 MeV. The other parameters were allowed to vary for the fit.

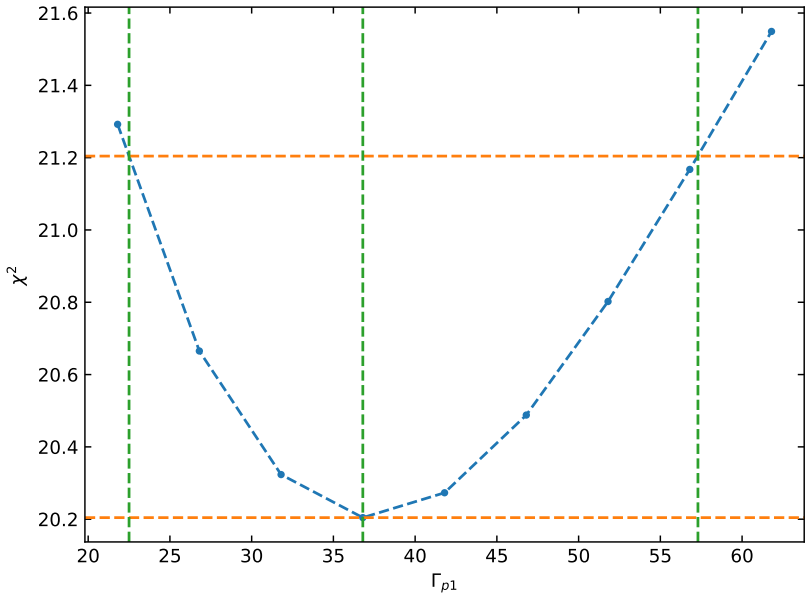

Figure 9.16: χ^2 as a function of Γ_{p1} for the state around 18.4 MeV. The other parameters were allowed to vary for the fit. $\Gamma_{p0} = 0$ is assumed.

Table 9.5: States obtained from R-matrix fitting to the region 17.6 MeV - 19.6 MeV.

Energy (MeV)	J^π	Γ
18.05(4)	1^-	1.21(5) MeV
18.232(2)	3^-	371(6) keV
$18.375(^{+7}_{-6})$	0^-	$37(^{+20}_{-14})$ keV
18.398(9)	3^-	285(10) keV
18.87(1)	1^-	850(10) keV
19.63(4)	1^-	480(20) keV

9.5 Summary

No indications of the predicted 0^- are found below the proton separation threshold, where the shell model places the state. The 15.1 MeV region has been evaluated and shows no indication of any 0^- component, with both angular distributions and γ-ray branching ratios excluding a 0^- state in this region.

States above the proton separation threshold have been analysed with R-matrix theory. A potential narrow 0^- state has been observed in coincidence with γ-ray decay from the first excited ^{11}B state, consistent with previous observations by Segel et al. (1965). This state is not observed in α-decay spectra, consistent with the 0^- assignment. A summary of the state energies and widths obtained from R-matrix fitting is shown in table 9.5.

Part IV

Summary and Outlook

Chapter 10

Summary and Outlook

Two experiments have been performed utilising nuclear reactions in order to determine the astrophysical ^{23}Na$(\alpha,p)^{26}$Mg reaction rate and to better understand the structure of the ^{12}C nucleus.

The new experimental reaction rate for the ^{23}Na$(\alpha,p)^{26}$Mg reaction significantly reduces the uncertainty on light elemental production in massive stars and type 1a supernovae. The recommended rate itself differs only slightly from the previous rate from statistical models, but the uncertainty on those models can vary from a factor of 2 up to even a factor of 10 for the ^{23}Na nucleus. In comparison the new combined experimental reaction rate has an uncertainty of 30%, based on three independent experimental measurements.

The elemental abundances have been evaluated by nuclear post-processing and most are now constrained to within 10% of the evaluated value. The Na abundance is observed to increase slightly compared to the NON-SMOKER abundance, changing by a factor of $1.04(^{+8}_{-7})$. The ^{26}Al abundance is changed by a factor of $0.98(^{+8}_{-7})$. The uncertainty on ^{26}Al abundance is now dependent on uncertainties in other rates lacking good experimental data, some of which are highlighted by Iliadis et al. (2011). The discrepancy between observed Na abundance and that predicted by the rate measured by Almaraz-Calderon et al. (2014) is no longer present with the new combined rate.

The structure of ^{12}C near the proton separation energy has been measured at iThemba LABS via the ^{11}B(^{3}He,d)^{12}C reaction. Theoretical shell-model and no-core shell-model calculations predict a previously unidentified 0^- state. The shell-model places the state in the 15 ± 0.5 MeV region, while the no-core shell-model places it in the 18 MeV region. The 0^- state is not found in the 15 MeV region as predicted by shell-model calculations, with both angular distributions and γ-ray coincidence analysis finding no evidence of the 0^- state within the strong 15.1 MeV region.

Above the proton separation energy, states have been analysed using a new R-matrix technique to account for the proton transfer into ^{12}C via ^{11}B(^{3}He,d)^{12}C and the subsequent particle decay. States previously observed

in the 17.6–18.6 and 18.6–19.6 MeV regions require additional interfering states to fully describe the structure observed in the present work. A weak, narrow, state at 18.4 MeV has been identified in γ-gated coincidence data of the first excited state in ^{11}B, with an energy of $18.375(^{+7}_{-6})$ MeV and width of $37(^{+20}_{-14})$ keV, respectively. This is consistent with a state observed previously by Segel et al. (1965) and assigned spin 0^- or 1^-. The state does not appear to α-decay in the present work, which strongly supports the previous 0^- assignment, and excludes the 1^-. This energy is consistent with the no-core shell-model predictions, and can be used to further understand and refine theoretical interaction models.

Appendix A

AZURE2 Modifications

This appendix will detail the modifications to the source code of AZURE2 version 1.0.0, released on 25 February 2015, necessary to adapt it for analysing the transfer+decay reactions discussed in chapter 6. These modifications in their current state replace the β-decay components of AZURE2, although it is entirely possible to add the transfer component as a new reaction type and therefore support both β-decay and transfer+decay. The source code for AZURE2 is available at `https://azure.nd.edu/downloads.php`, after registering.

A.1 Diff Notation

The appendix will list the files with modifications made, and a brief summary of the changes made. Following this the specific code modifications will be detailed in the *unified diff format*: a standard notation for recording the differences in text files, produced by the unix command `diff -u`. Each change within a file is termed a 'hunk', and is preceded with information about its location within the file:

```
@@ -l,s +l,s @@
```

Where `l` refers to the line number and `s` the number of lines. The first pair refer to the original file, and the second to the modified file. Following this is a list of lines, optionally prefixed with a `-` to indicate the line is *deleted*, or `+` to indicate the line is *added*. Changed lines are described by deleting the original and adding the replacement. Lines without a prefix are unmodified and used to determine context.

A.2 Modifications to the AZURE2 GUI

gui/src/AddPairDialog.cpp

This file is part of the AZURE2 GUI and is responsible for defining a particle pair. We modify the lines which restrict the β-decay pair from allowing input of the lighter particle's spin and mass.

```
@@ -157,13 +157,13 @@
channelRadiusText->setEnabled(false);
multBox->show();
} else if(index==2) {
- lightJText->setEnabled(false);
- lightJText->setText("0.5");
- lightPiCombo->setEnabled(false);
- lightPiCombo->setCurrentIndex(1);
+ lightJText->setEnabled(true);
+ //lightJText->setText("0.5");
+ lightPiCombo->setEnabled(true);
+ //lightPiCombo->setCurrentIndex(1);
lightZText->setEnabled(true);
- lightMText->setEnabled(false);
- lightMText->setText("0.0005");
+ lightMText->setEnabled(true);
+ //lightMText->setText("1");
//lightGText->setEnabled(false);
//lightGText->setText("2.0023");
seperationEnergyText->setEnabled(true);
```

gui/src/LevelsTab.cpp

This file is part of the AZURE2 GUI and is responsible for listing the compound nucleus levels, and determining the list of channels for each particle pair. We modify the *beta*-decay lines to produce a set of channels according to conservation of angular momentum rather than Gamow-Teller and Fermi decays:

```
@@ -382,14 +382,13 @@
}
}
} else if(pair.pairType==20) {
- if(fabs(pair.heavyJ-level.jValue)==0.&&pair.heavyPi==level.
    ↪ piValue) {
- ChannelsData gtChannel = {0,levelIndex,i,0.,1,'G',0.0};
- ChannelsData fChannel = {0,levelIndex,i,0.,0,'F',0.0};
```

```
- channels.push_back(gtChannel);
- channels.push_back(fChannel);
- } else if(fabs(pair.heavyJ-level.jValue)==1.&&pair.heavyPi==
    ↪ level.piValue) {
- ChannelsData gtChannel = {0,levelIndex,i,1.,1,'G',0.0};
- channels.push_back(gtChannel);
+ for(double s=fabs(pair.heavyJ-pair.lightJ);s<=pair.heavyJ+pair
    ↪ .lightJ;s+=1.0) {
+  for(double l=fabs(s-level.jValue);l<=s+level.jValue;l+=1.0) {
+  if(int(l*2.0)%2==0&&1*1*pow(-1,int(l))==level.piValue&&int(l)
    ↪ <=maxL) {
+  ChannelsData channel={0,levelIndex,i,s,int(l),'P',0.0};
+  channels.push_back(channel);
+  }
+  }
}
} else {
int numMult=1;
@@ -562,7 +561,8 @@
else if (pair.pairType==10&&level.energy==pair.excitationEnergy
    ↪ &&level.jValue==pair.heavyJ&&
level.piValue==pair.heavyPi&&channel.radType=='E'&&channel.
    ↪ lValue==2)
channelDetails->setNormParam(3);
- else if(pair.pairType==20) channelDetails->setNormParam(4);
+ //else if(pair.pairType==20) channelDetails->setNormParam(4);
+ else if(level.energy<(pair.seperationEnergy+pair.
    ↪ excitationEnergy)&&pair.pairType==20) channelDetails->
    ↪ setNormParam(1);
else channelDetails->setNormParam(0);
channelDetails->reducedWidthText->setText(QString("%1").arg(
    ↪ channel.reducedWidth));
channelDetails->show();
@@ -768,8 +768,8 @@
QChar radType;
if(pairType==0) radType='P';
else if(pairType==20) {
- if(channelL==0) radType = 'F';
- else radType = 'G';
+ if(channelL==0) radType = 'P';
+ else radType = 'P';
}
else {
int parityChange=heavyPi*levelPi;
```

gui/src/PairsModel.cpp

This file is part of the AZURE2 GUI and is responsible for formatting a particle pair in various forms in the GUI. We modify the β-decay type to print the appropriate light particle type with a subscript T to denote the transfer, rather than just $\beta^{\pm}$.

```
@@ -188,8 +188,18 @@
if(which!=-1) {
if(pair.pairType==10&&which==0) return "<center>&gamma;</center
    ↪ >";
else if(pair.pairType==20&&which==0) {
- if(pair.lightZ<0) return "<center>&beta;<sup>-</sup></center
    ↪ >";
- else return "<center>&beta;<sup>+</sup></center>";
+ //if(pair.lightZ<0) return "<center>&beta;<sup>-</sup></center
    ↪ >";
+ //else return "<center>&beta;<sup>+</sup></center>";
+ int tempZ=pair.lightZ;
+  int tempM=round(pair.lightM);
+ std::map<int, QString>::const_iterator it=elementMap.find(
    ↪ tempZ);
+ if(it!=elementMap.end()) {
+  if(tempM==1) {
+  if(tempZ==1) return "<center><i>p<sub>T</sub></i></center>";
+  else return QString("<center><i>%1<sub>T</sub></i></center>")
    ↪ .arg(it->second);
+  } else if(tempZ==2&&tempM==4) return "<center>&alpha;<sub>T</
    ↪ sub></center>";
+  else return QString("<center><sup>%1</sup>%2<sub>T</sub></
    ↪ center>").arg(tempM).arg(it->second);
+ } else return "?";
} else {
int tempZ;
int tempM;
@@ -214,8 +224,13 @@
std::map<int, QString>::const_iterator it=elementMap.find(pair.
    ↪ lightZ);
if(pair.pairType==10) lightLabel="&gamma;";
else if(pair.pairType==20) {
- if(pair.lightZ<0.) lightLabel="&beta;<sup>-</sup>";
- else lightLabel="&beta;<sup>+</sup>";
```

```
+ if(it!=elementMap.end()) {
+ if(round(pair.lightM)==1) {
+  if(pair.lightZ==1) lightLabel="<i>p<sub>T</sub></i>";
+  else lightLabel=QString("<i>%1<sub>T</sub></i>").arg(it->
    ↪ second);
+ } else if(pair.lightZ==2&&round(pair.lightM)==4) lightLabel="&
    ↪ alpha;<sub>T</sub>";
+ else lightLabel=QString("<sup>%1</sup>%2<sub>T</sub>").arg(
    ↪ round(pair.lightM)).arg(it->second);
+ } else lightLabel="?";
} else if(it!=elementMap.end()) {
if(round(pair.lightM)==1) {
if(pair.lightZ==1) lightLabel="<i>p</i>";
@@ -232,7 +247,7 @@
} else if(pair.heavyZ==2&&round(pair.heavyM)==4) heavyLabel="&
    ↪ alpha;";
else heavyLabel=QString("<sup>%1</sup>%2").arg(round(pair.heavyM
    ↪ )).arg(it->second);
} else heavyLabel="?";
- if(pair.pairType==20) return QString("<center>%1(%2) [%3 MeV
    ↪ ]</center>").arg(heavyLabel).arg(lightLabel).arg(pair.
    ↪ excitationEnergy,0,'f',3);
+ if(pair.pairType==20) return QString("<center>%1+%2 [%3 MeV]</
    ↪ center>").arg(heavyLabel).arg(lightLabel).arg(pair.
    ↪ excitationEnergy,0,'f',3);
else return QString("<center>%1+%2 [%3 MeV]</center>").arg(
    ↪ heavyLabel).arg(lightLabel).arg(pair.excitationEnergy,0,'
    ↪ f',3);
}
}
@@ -242,8 +257,13 @@
std::map<int, QString>::const_iterator it=elementMap.find(
    ↪ firstPair.lightZ);
if(firstPair.pairType==10) lightLabel[0]="&gamma;";
else if(firstPair.pairType==20) {
- if(firstPair.lightZ<0) lightLabel[0]="&beta;<sup>-</sup>";
- else lightLabel[0]="&beta;<sup>+</sup>";
+ if(it!=elementMap.end()) {
+ if(round(firstPair.lightM)==1) {
+ if(firstPair.lightZ==1) lightLabel[0]="<i>p<sub>T</sub></i>";
+ else lightLabel[0]=QString("<i>%1<sub>T</sub></i>").arg(it->
    ↪ second);
+ } else if(firstPair.lightZ==2&&round(firstPair.lightM)==4)
    ↪ lightLabel[0]="&alpha;<sub>T</sub>";
```

```
+ else lightLabel[0]=QString("<sup>%1</sup>%2<sub>T</sub>").arg(
    ↪ round(firstPair.lightM)).arg(it->second);
+ } else lightLabel[0]="?";
} else if(it!=elementMap.end()) {
if(round(firstPair.lightM)==1) {
if(firstPair.lightZ==1) lightLabel[0]="<i>p</i>";
@@ -254,8 +274,13 @@
it=elementMap.find(secondPair.lightZ);
if(secondPair.pairType==10) lightLabel[1]="&gamma;";
else if(secondPair.pairType==20) {
- if(secondPair.lightZ<0) lightLabel[1]="&beta;<sup>-</sup>";
- else lightLabel[1]="&beta;<sup>+</sup>";
+ if(it!=elementMap.end()) {
+ if(round(secondPair.lightM)==1) {
+ if(secondPair.lightZ==1) lightLabel[1]="<i>p<sub>T</sub></i>";
+ else lightLabel[1]=QString("<i>%1<sub>T</sub></i>").arg(it->
    ↪ second);
+ } else if(secondPair.lightZ==2&&round(secondPair.lightM)==4)
    ↪ lightLabel[1]="&alpha;<sub>T</sub>";
+ else lightLabel[1]=QString("<sup>%1</sup>%2<sub>T</sub>").arg(
    ↪ round(secondPair.lightM)).arg(it->second);
+ } else lightLabel[1]="?";
} else if(it!=elementMap.end()) {
if(round(secondPair.lightM)==1) {
if(secondPair.lightZ==1) lightLabel[1]="<i>p</i>";
@@ -280,7 +305,7 @@
} else if(secondPair.heavyZ==2&&round(secondPair.heavyM)==4)
    ↪ heavyLabel[1]="&alpha;";
else heavyLabel[1]=QString("<sup>%1</sup>%2").arg(round(
    ↪ secondPair.heavyM)).arg(it->second);
} else heavyLabel[1]="?";
- if(firstPair.pairType==20) return QString("%1(%2%3)%4 [%5 MeV
    ↪ ]").arg(heavyLabel[0]).arg(lightLabel[0]).arg(lightLabel
    ↪ [1]).arg(heavyLabel[1]).arg(secondPair.excitationEnergy
    ↪ ,0,'f',3);
+ if(firstPair.pairType==230) return QString("%1(%2%3)%4 [%5 MeV
    ↪ ]").arg(heavyLabel[0]).arg(lightLabel[0]).arg(lightLabel
    ↪ [1]).arg(heavyLabel[1]).arg(secondPair.excitationEnergy
    ↪ ,0,'f',3);
else return QString("%1(%2,%3)%4 [%5 MeV]").arg(heavyLabel[0]).
    ↪ arg(lightLabel[0]).arg(lightLabel[1]).arg(heavyLabel[1]).
    ↪ arg(secondPair.excitationEnergy,0,'f',3);
}
```

A.3 Modifications to the AZURE2 Fitting Code

src/AChannel.cpp

This file defines a single reaction channel, we replace code that marks β-decay channels as Fermi or Gamow-Teller with code that marks transfer channels as such.

```
@@ -18,8 +18,9 @@
if(nucLine.levelPi()*nucLine.pi2()==pow(-1,nucLine.l()))
    ↪ radtype_='E';
else radtype_='M';
} else if(nucLine.pType()==20) {
- if(nucLine.l()==0) radtype_='F';
- else radtype_='G';
+ //if(nucLine.l()==0) radtype_='F';
+ //else radtype_='G';
+ radtype_='T';
}
}
```

src/CNuc.cpp

This file is responsible for properties of the compound nucleus, we modify β-specific lines to handle the transfer type, and ensure it is treated with full angular momentum channels, but excluded from transforming input parameters as physical widths.

```
@@ -125,6 +125,7 @@
NucLine Line(stm);
if(stm.rdstate() & (std::stringstream::failbit | std::
    ↪ stringstream::badbit)) return -1;
if(Line.l()>maxLValue&&Line.pType()==0) maxLValue=Line.l();
+ if(Line.l()>maxLValue&&Line.pType()==20) maxLValue=Line.l();
if(Line.isActive()==1) {
PPair NewPair(Line);
PairNum=this->IsPair(NewPair);
@@ -471,7 +473,7 @@
if(tempPene<1e-16) tempPene=1e-16;
penes.push_back(tempPene);
}
- } else if(theChannel->GetRadType()=='F'||theChannel->
    ↪ GetRadType()=='G') {
+ } else if(theChannel->GetRadType()=='F'||theChannel->
    ↪ GetRadType()=='G'||theChannel->GetRadType()=='T') {
```

```
if(theLevel->GetGamma(ch)<0.0) isNegative.push_back(true);
else isNegative.push_back(false);
tempGammas.push_back(fabs(theLevel->GetGamma(ch)));
@@ -485,7 +487,7 @@
double nFSum=1.0;
for(int ch=1;ch<=theJGroup->NumChannels();ch++) {
AChannel *theChannel=theJGroup->GetChannel(ch);
- if(theChannel->GetRadType()!='F'&&theChannel->GetRadType()!='G
    ↪ ')
+ if(theChannel->GetRadType()!='F'&&theChannel->GetRadType()!='G
    ↪ '&&theChannel->GetRadType()!='T')
tempGammas[ch-1]=sqrt(fabs(tempGammas[ch-1]/penes[ch-1]/denom));
if(isNegative[ch-1]) tempGammas[ch-1]=-tempGammas[ch-1];
theLevel->SetGamma(ch,tempGammas[ch-1]);
@@ -621,8 +623,8 @@
for(int aa=1;aa<=this->NumPairs();aa++) {
if(!this->GetPair(aa)->IsEntrance()) continue;
for(int ir=1;ir<=this->NumPairs();ir++) {
- if(this->GetPair(ir)->GetPType()==20) continue;
- if(this->GetPair(aa)->GetPType()==20) {
+ //if(this->GetPair(ir)->GetPType()==20) continue;
+ if(this->GetPair(aa)->GetPType()==230) {
for(int l = 0; l < 2; l++) {
for(int j=1;j<=this->NumJGroups();j++) {
if(!this->GetJGroup(j)->IsInRMatrix()) continue;
@@ -653,7 +655,7 @@
}
}
}
- } else if(this->GetPair(ir)->GetPType()==0) {
+} else if(this->GetPair(ir)->GetPType()==0 || this->GetPair(ir)
    ↪ ->GetPType()==20) {
for(double s=fabs(this->GetPair(aa)->GetJ(1)-this->GetPair(aa)->
    ↪ GetJ(2));
s<=(this->GetPair(aa)->GetJ(1)+this->GetPair(aa)->GetJ(2));s
    ↪ +=1.) {
for(double sp=fabs(this->GetPair(ir)->GetJ(1)-this->GetPair(ir)
    ↪ ->GetJ(2));
@@ -734,7 +736,7 @@
}
for(int aa=1;aa<=this->NumPairs();aa++) { //loop over all pairs
PPair *entrancePair=this->GetPair(aa);
- if(entrancePair->GetPType()==20 || !entrancePair->IsEntrance()
    ↪ ) continue;
```

```
+ if(entrancePair->GetPType()==230 || !entrancePair->IsEntrance
    ↪ ()) continue;
for(int j=1;j<=this->NumJGroups();j++) {
JGroup *theFinalJGroup=this->GetJGroup(j);
for(int la=1;la<=theFinalJGroup->NumLevels();la++) {
@@ -746,7 +748,7 @@
KGroup *theKGroup=entrancePair->GetDecay(decayNum)->GetKGroup(k)
    ↪ ;
for(int chp=1;chp<=theFinalJGroup->NumChannels();chp++) { //loop
    ↪  over all final configurations in the capture state
AChannel *finalChannel=theFinalJGroup->GetChannel(chp);
- if(this->GetPair(finalChannel->GetPairNum())->GetPType()!=0)
    ↪ continue; //ensure the configuration is a particle pair
+ if(this->GetPair(finalChannel->GetPairNum())->GetPType()==10)
    ↪ continue; //ensure the configuration is a particle pair
int chDecayNum=entrancePair->IsDecay(finalChannel->GetPairNum())
    ↪ ;
if(!chDecayNum) continue; //if it is actually a resonance decay
    ↪ ...
for(int kp=1;kp<=entrancePair->GetDecay(chDecayNum)->NumKGroups
    ↪ ();kp++) {
@@ -922,7 +924,7 @@
for(int ch=1;ch<=theJGroup->NumChannels();ch++) {
AChannel *theChannel=theJGroup->GetChannel(ch);
PPair *thePair=this->GetPair(theChannel->GetPairNum());
- if(thePair->GetPType()==0) {
+ if(thePair->GetPType()==0 || thePair->GetPType()==20) {
int lValue=theChannel->GetL();
double levelEnergy=firstLevel->GetE();
double resonanceEnergy=levelEnergy-(thePair->GetSepE()+thePair->
    ↪ GetExE());
@@ -1390,7 +1392,7 @@
complex totalWidth=theLevel->GetTransformGamma(ch)+externalWidth
    ↪ ;
int tempSign = (real(totalWidth)<0.) ? (-1) : (1);
double bigGamma;
- if(theChannel->GetRadType()!='F'&&theChannel->GetRadType()!='G
    ↪ ')
+ if(theChannel->GetRadType()!='F'&&theChannel->GetRadType()!='G
    ↪ '&&theChannel->GetRadType()!='T')
bigGamma=tempSign*2.0*real(totalWidth*conj(totalWidth))*tempPene
    ↪ [ch-1]/
(1.0+normSum);
else bigGamma=real(totalWidth);
```

```
@@ -1454,7 +1456,7 @@
int tempSign = (theLevel->GetBigGamma(ch)<0) ? (-1) : (1);
out << " Q = " << std::setw(12) << tempSign*sqrt(fabs(theLevel->
    ↪ GetBigGamma(ch)))/100.0/sqrt(fstruc*hbarc)
<< " b ";
- } else if(theChannel->GetRadType()=='F'|| theChannel->
    ↪ GetRadType()=='G') {
+ } else if(theChannel->GetRadType()=='F'|| theChannel->
    ↪ GetRadType()=='G' || theChannel->GetRadType()=='T') {
out << " B = " << std::setw(12) << theLevel->GetBigGamma(ch)
<< " ";
} else {
```

src/EPoint.cpp

This file handles data for a single experimental data point. We modify the R-matrix points to interpret the centre of mass energy for transfer reactions, and we remove the Fermi phase factor from calculations.

```
@@ -483,7 +483,8 @@
cm_energy_=this->GetLabEnergy()/
(pPair->GetM(2))*
(pPair->GetM(1)+pPair->GetM(2));
- excitation_energy_=cm_energy_+pPair->GetSepE();
+ excitation_energy_= cm_energy_ + pPair->GetSepE();
+ cm_energy_ -= pPair->GetExE();
}

/*!
@@ -712,10 +713,10 @@
} else if(thePair->GetPType()==20){
complex loElement = complex(0.0,0.0);
this->AddLoElement(j,ch,loElement);
- IntegratedFermiFunc fermiFunc(thePair->GetZ(1));
- double endPointE = thePair->GetSepE()-inEnergy;
- double sqrtPene = (1.+endPointE/0.510998903<=1.) ? 0. : sqrt(
    ↪ fermiFunc(1.+endPointE/0.510998903,exitPair->GetZ(1)+
    ↪ exitPair->GetZ(2),thePair->GetChRad()));
- this->AddSqrtPenetrability(j,ch,sqrtPene);
+ //IntegratedFermiFunc fermiFunc(thePair->GetZ(1));
+ //double endPointE = thePair->GetSepE()-inEnergy;
+ //double sqrtPene = (1.+endPointE/0.510998903<=1.) ? 0. : sqrt
    ↪ (fermiFunc(1.+endPointE/0.510998903,exitPair->GetZ(1)+
    ↪ exitPair->GetZ(2),thePair->GetChRad()));
```

```
+ this->AddSqrtPenetrability(j,ch,1.0);
this->AddExpCoulombPhase(j,ch,1.0);
this->AddExpHardSpherePhase(j,ch,1.0);
}
```

References

Adsley, P. 2017, Private Communication

Adsley, P., Neveling, R., Donaldson, L. M., Pellegri, L., & Hubbard, N. J. 2014, k600analyser, GitHub. https://github.com/padsley/k600analyser/

Adsley, P., Neveling, R., Papka, P., et al. 2017, J. Instrum., 12, T02004. http://stacks.iop.org/1748-0221/12/i=02/a=T02004?key=crossref.3f0987ba3a82bcfdc472d771c364364a

Alburger, D. E., & Wilkinson, D. H. 1972, Phys. Rev. C, 5, 384. https://link.aps.org/doi/10.1103/PhysRevC.5.384

Almaraz-Calderon, S., Bertone, P. F., Alcorta, M., et al. 2014, Phys. Rev. Lett., 112, 152701. http://journals.aps.org/prl/abstract/10.1103/PhysRevLett.112.152701

—. 2015, Phys. Rev. Lett., 115, 179901. http://link.aps.org/doi/10.1103/PhysRevLett.115.179901

Angulo, C., Arnould, M., Rayet, M., et al. 1999, Nucl. Phys. A, 656, 3. https://www.sciencedirect.com/science/article/abs/pii/S0375947499000305

Azuma, R. E., Uberseder, E., Simpson, E. C., et al. 2010, Phys. Rev. C, 81, 045805. https://link.aps.org/doi/10.1103/PhysRevC.81.045805

Bair, J. K., Kington, J. D., & Willard, H. B. 1955, Phys. Rev., 100, 21. https://link.aps.org/doi/10.1103/PhysRev.100.21

Barker, F., & Warburton, E. 1988, Nucl. Phys. A, 487, 269. http://linkinghub.elsevier.com/retrieve/pii/0375947488906136

Barlow, R. 1989, Statistics: a guide to the use of statistical methods in the physical sciences (Wiley)

Barrett, B. R., Navrátil, P., & Vary, J. P. 2013, Prog. Part. Nucl. Phys., 69, 131. http://linkinghub.elsevier.com/retrieve/pii/S0146641012001184

Bohne, W., Homeyert, H., Morgenstern, H., & Scheer, J. 1968, Nucl. Phys. A, 115, 457. https://www.sciencedirect.com/science/article/pii/0375947468900183

Bravo, E., & Martínez-Pinedo, G. 2012, Phys. Rev. C, 85, 55805. http://link.aps.org/doi/10.1103/PhysRevC.85.055805

Brown, B. A., & Wildenthal, B. H. 1988, Annu. Rev. Nucl. Part. Sci., 38, 29. http://www.annualreviews.org/doi/10.1146/annurev.ns.38.120188.000333

Brune, C. R. 2002, Phys. Rev. C, 66, 044611. https://link.aps.org/doi/10.1103/PhysRevC.66.044611

Burbidge, E. M., Burbidge, G. R., Fowler, W. A., & Hoyle, F. 1957, Rev. Mod. Phys., 29, 547. https://link.aps.org/doi/10.1103/RevModPhys.29.547

Catford, W. 2004, CATKIN. http://personal.ph.surrey.ac.uk/~phs1wc/kinematics/

Chen, W., Gehrels, N., & Diehl, R. 1995, Astrophys. J., 440, L57. http://adsabs.harvard.edu/doi/10.1086/187760

Chiari, M., Giuntini, L., Mandò, P. A., & Taccetti, N. 2001, Nucl. Instruments Methods Phys. Res. Sect. B Beam Interact. with Mater. Atoms, 184, 309. http://www.sciencedirect.com/science/article/pii/S0168583X0100787X

Cybert, R. H., Amthor, A. M., Ferguson, R., et al. 2010, Astrophys. J. Suppl. Ser., 189, 240. http://stacks.iop.org/0067-0049/189/i=1/a=240

Daehnick, W. W., Childs, J. D., & Vrcelj, Z. 1980, Phys. Rev. C, 21, 2253. https://link.aps.org/doi/10.1103/PhysRevC.21.2253

Descouvemont, P., & Baye, D. 2010, Reports Prog. Phys., 73, 036301. https://arxiv.org/pdf/1001.0678.pdfhttp://stacks.iop.org/0034-4885/73/i=3/a=036301

Diehl, R., Alexander, F., Krause, M., et al. 2013, Proc. Sci., arXiv:1307.4190. http://arxiv.org/abs/1307.4190

Eggenberger, P., Meynet, G., Maeder, A., et al. 2008, Astrophys. Space Sci., 316, 43. http://link.springer.com/10.1007/s10509-007-9511-y

Ekström, A., Baardsen, G., Forssén, C., et al. 2013, Phys. Rev. Lett., 110, 192502. https://link.aps.org/doi/10.1103/PhysRevLett.110.192502

Enge, H. A. 1981, Nucl. Instruments Methods, 187, 1. http://www.sciencedirect.com/science/article/pii/0029554X81904651

Firestone, R. B. 1996, Table of Isotopes Eighth Edition (Wiley)

Forssén, C. 2017, Private Communication

Freer, M. 2007, Reports Prog. Phys., 70, 2149. http://stacks.iop.org/0034-4885/70/i=12/a=R03?key=crossref.542b2ddafb36be32cde46f85b5c26e7c

Fujita, H. 2004, Internal Memo, iThemba LABS

Hinds, S., & Middleton, R. 1961, Proc. Phys. Soc., 78, 81. http://stacks.iop.org/0370-1328/78/i=1/a=313?key=crossref.87b6f70a2c4dcb6409f9e1e7d5e6bcfc

Howard, A. M., Munch, M., Fynbo, H. O. U., et al. 2015, Phys. Rev. Lett., 115, 052701. http://journals.aps.org/prl/abstract/10.1103/PhysRevLett.115.052701

Hoyle, F. 1954, Astrophys. J. Suppl. S., 1, 121. http://adsabs.harvard.edu/doi/10.1086/190005

Iliadis, C. 2008, Nuclear Physics of Stars (Wiley-VCH)

Iliadis, C., Champagne, A., Chieffi, A., & Limongi, M. 2011, Astrophys. J. Suppl. Ser., 193, 16. http://iopscience.iop.org/0067-0049/193/1/16/article/

Iliadis, C., Longland, R., Champagne, A., Coc, A., & Fitzgerald, R. 2010, Nucl. Phys. A, 841, 31. https://www.sciencedirect.com/science/article/abs/pii/S0375947410004197

James, F., & Winkler, M. 2004, MINUIT User's Guide. http://seal.web.cern.ch/seal/documents/minuit/mnusersguide.pdf

Jeukenne, J. P., Lejeune, A., & Mahaux, C. 1977, Phys. Rev. C, 16, 80. https://link.aps.org/doi/10.1103/PhysRevC.16.80

Kelley, J., Purcell, J., & Sheu, C. 2017, Nucl. Phys. A, 968, 71. http://linkinghub.elsevier.com/retrieve/pii/S0375947417303330

Krane, K. S. 1987, Introductory Nuclear Physics (Wiley)

Kuperus, J. 1964, Physica, 30, 2253. http://www.sciencedirect.com/science/article/pii/0031891464900527

Lane, A. M., & Thomas, R. G. 1958, Rev. Mod. Phys., 30, 257. https://link.aps.org/doi/10.1103/RevModPhys.30.257

Li, K. C. W. 2015, Characterization of the pre-eminent 4-α cluster state candidate in 16O (MSc thesis), Stellenbosch University. http://hdl.handle.net/10019.1/97982

McFadden, L., & Satchler, G. R. 1966, Nucl. Phys., 84, 177. https://www.sciencedirect.com/science/article/pii/002955826690441X

Micron Semiconductor Ltd. 2018, 2018 Catalogue. http://www.micronsemiconductor.co.uk/silicon-detector-catalogue/

Miller, P. D., Duggan, J. L., Duncan, M. M., et al. 1969, Nucl. Physics, Sect. A, 136, 229

Mohr, P. 2015, Eur. Phys. J. A, 51, doi:10.1140/epja/i2015-15056-5. http://dx.doi.org/10.1140/epja/i2015-15056-5

Möller, P., Nix, J., & Kratz, K.-L. 1997, At. Data Nucl. Data Tables, 66, 131. https://www.sciencedirect.com/science/article/pii/S0092640X97907464

Möller, P., Nix, J., Myers, W., & Swiatecki, W. 1995, At. Data Nucl. Data Tables, 59, 185. https://www.sciencedirect.com/science/article/pii/S0092640X97907464https://www.sciencedirect.com/science/article/pii/S0092640X85710029

Naqib, I., & Green, L. 1968, Nucl. Phys. A, 112, 76. https://www.sciencedirect.com/science/article/abs/pii/0375947468902200

Neveling, R., Smit, F. D., Fujita, H., et al. 2016, Guide to the K600 magnetic spectrometer, Tech. rep., iThemba LABS

Neveling, R., Fujita, H., Smit, F. D., et al. 2011, Nucl. Instruments Methods Phys. Res. Sect. A Accel. Spectrometers, Detect. Assoc. Equip., 654, 29. http://www.sciencedirect.com/science/article/pii/S0168900211012460

Pagel, B. E. 1997, Nucleosynthesis and Chemical Evolution of Galaxies (Cambridge University Press)

Pang, D. Y., Roussel-Chomaz, P., Savajols, H., Varner, R. L., & Wolski, R. 2009, Phys. Rev. C, 79, 024615. https://link.aps.org/doi/10.1103/PhysRevC.79.024615

Parikh, A. 2016, Private Communication

Parikh, A., José, J., Seitenzahl, I. R., & Röpke, F. K. 2013, A&A, 557, A3. https://www.aanda.org/articles/aa/pdf/2013/09/aa21518-13.pdf

Pignatari, M., Herwig, F., Hirschi, R., et al. 2016, Astrophys. J. Suppl. Ser., 225, 24. http://iopscience.iop.org/article/10.3847/0067-0049/225/2/24/pdf

Plüschke, S., Diehl, R., Schönfelder, V., et al. 2001, in Eur. Sp. Agency, (Special Publ. ESA SP, Vol. 459, 55–58. http://arxiv.org/abs/astro-ph/0104047

Rauscher, T. 2003, exp2rate. http://download.nucastro.org/codes/exp2rate.f90

Rauscher, T., & Thielemann, F.-K. 2000, At. Data Nucl. Data Tables, 75, 1. http://www.sciencedirect.com/science/article/pii/S0092640X00908349http://linkinghub.elsevier.com/retrieve/pii/S0092640X00908349

Rauscher, T., Thielemann, F. K., & Kratz, K. L. 1997, Phys. Rev. C, 56, 1613. https://link.aps.org/doi/10.1103/PhysRevC.56.1613

Rolfs, C. E., & Rodney, W. S. 2005, Cauldrons in the Cosmos: Nuclear Astrophysics (University of Chicago Press)

Schiffer, J. P., Hoffman, C. R., Kay, B. P., et al. 2013, Phys. Rev. C, 87, 034306. https://link.aps.org/doi/10.1103/PhysRevC.87.034306

Segel, R. E., Hanna, S. S., & Allas, R. G. 1965, Phys. Rev., 139, B818. https://link.aps.org/doi/10.1103/PhysRev.139.B818

Smith, M., Lingerfelt, E., Nesaraja, C., & Smith, C. 2004, Computation Infrastructure for Nuclear Astrophysics, nucastrodata. http://www.nucastrodata.org/infrastructure.html

Spasskii, A. V., Teplov, I. B., & Fateeva, L. N. 1968, Sov. J. Nucl. Phys, 7, 175

Taylor, J. R. 1983, Scattering theory : the quantum theory of nonrelativistic collisions (Wiley), xvi, 477

Thomas, R. G. 1951, Phys. Rev., 81, 148. https://link.aps.org/doi/10.1103/PhysRev.81.148

Timmes, F. X., Woosley, S. E., & Weaver, T. A. 1995, Astrophys. J. Suppl. Ser., 98, 617. http://adsabs.harvard.edu/doi/10.1086/192172

Tomlinson, J. R. 2015, PhD thesis, University of York. http://etheses.whiterose.ac.uk/12576/

Tomlinson, J. R., Fallis, J., Laird, A. M., et al. 2015, Phys. Rev. Lett., 115, 052702. http://journals.aps.org/prl/abstract/10.1103/PhysRevLett.115.052702

Tostevin, J. A. 2017, University of Surrey version of the code TWOFNR (of M. Toyama, M. Igarashi and N. Kishida) and code FRONT (private communication). http://www.nucleartheory.net/NPG/code.htm

Vogt, E. 2005, R-Matrix Theory, JINA. http://www.jinaweb.org/events/matrix/05-R-matrix.pdf

Warburton, E. K., & Brown, B. A. 1992, Phys. Rev. C, 46, 923. https://link.aps.org/doi/10.1103/PhysRevC.46.923

Whitmire, D. P., & Davids, C. N. 1974, Phys. Rev. C, 9, 996. http://link.aps.org/doi/10.1103/PhysRevC.9.996

Woosley, S. E., & Weaver, T. A. 1995, Astrophys. J. Suppl. Ser., 101, 181. http://adsabs.harvard.edu/doi/10.1086/192237